THE MEASUREMENT OF NEUTRON ACTIVATION

CROSS SECTIONS IN THE ENERGY RANGE

3.5 Mev TO 6.0 Mev

by

NABIL ABDUL JALIL

A thesis submitted for the degree
of
Doctor of Philosophy
at
The University of Aston in Birmingham

Department of Physics
University of Aston

THE UNIVERSITY OF ASTON IN BIRMINGHAM

THE MEASUREMENT OF NEUTRON ACTIVATION

CROSS SECTIONS IN THE ENERGY RANGE

3.5 Mev TO 6.0 Mev

By

NABIL ABDUL JALIL

Ph.D NOV. 1980

SUMMARY

A measurement of the ^{46,47,48}Ti(n,p)^{46,47,48}Sc reaction cross-sections has been performed relative to the U-235 fission cross-sections over the neutron energy range of 3.5 Mev to 6.0 Mev.

The uranium-235 content, required for flux analysis, was determined from both 2π and low geometry alpha-particle assay. Fissions from the U-235 standard were detected in a low mass parallel-plate ionisation chamber. To provide a satisfactory neutron flux, a deuterium gas taget was designed to withstand up to three times the maximum beam power densities permissible in conventional gas targets.

The gamma-ray activities induced in the irradiated samples were determined using a 7.62 cm x 7.62 cm NaI(TI) detector. The gamma-ray detection efficiencies were corrected for sample self-scattering and self-absorption using the Monte Carlo method. A second Monte Carlo program was developed to correct for irradiation geometry. Corrections were applied for neutron scattering within the sample and fission chamber, and the thermal and background neutrons.

The present measurements are in agreement with other measurements, whilst providing greater accuracies.

(n,p) Cross-sections :

Neutron Activations :

Gamma-ray Activity :

Ti(n, p)Sc cross-sections

ACKNOWLEDGEMENTS

I am grateful to :

Professor S.E. Hunt , for the provision of facilities
used for the completion of this work ,

Dr. A.Bore , who made himself available countless
times for discussion and supervision throughout this
project work ,

Frank and Howard of the work-shop staff , for
building the components used , and for many ingenious
suggestions ,

the operators of the Dynamitron accelerator and the
Radiation Centre staff for the co-operation given ,

the Tun Ismail Atomic Research Centre and the
Government of Malaysia for their financial support ,

and my wife , for her help , patience and understanding
throughout the course of this work .

CONTENTS

LIST OF TABLES

CHAPTER 1

INTRODUCTION

CHAPTER 1

NUCLEAR DATA

The work undertaken aims to provide a contribution to the world nuclear data requirements over the fast neutron energy range, for the fission and fusion reactor programmes. Data is required on neutron interactions with a variety of reactor materials such as fuel, cladding, biological shields and dosimetry.

To this end, there has been extensive international co-operation between member countries of the International Atomic Energy Agency, particularly between the United States and Europe /1/. A compilation of World request lists is documented in WRENDA /2/ (World Request List for Nuclear Data) and published biennially by IAEA. Over 600 items are listed in the requests, covering data mainly for reactor design, operation and safety performance predictions. It may also be noted that requests originating in different countries for the same reactor sometimes differ /3/. The request lists in WRENDA serve as a guide for experimentalists and evaluators in the planning of nuclear data measurements and evaluations. Information regarding such measurements may be forwarded to the Nuclear Data section of the IAEA or the regional nuclear data centre, the centre serving Europe being situated in Saclay, France

1.1 Applications and requirements of Nuclear Data in Reactor Design

The design of a reactor proceeds through three stages. In the initial stage, the designer is required to perform calculations to optimise the behaviour of the projected design and the economic feasibility of the design. In the second stage, the safety aspects of the design are investigated, involving a complete safety assessment requiring a knowledge of the underlying physics relevant to an accident situation. The final stage follows the construction of the reactor, where measurements on the kinetic behaviour of the reactor are performed. Although direct measurements of the kinetic behaviour provide more accurate information than calculations, accurate nuclear data is required for the analysis of observed anomalies in reactor behaviour.

The construction of prototype fast power reactors have been invariably preceeded by a mock-up zero power reactor having a critical assembly of the same dimensions and fuel, but operating at a power of less than 100 watts. Measurements on the zero power reactor can be extrapolated to predict the performance of the power reactor. Such experiments are currently required due to the lack of reliability of theoretical calculations stemming from uncertainties

in nuclear data. Considerable improvements in nuclear data would inevitably reduce the need for extensive preliminary experiments. This is already the case in the thermal reactor field where accurate predictions can be made on the basis of existing knowledge.

The implications of uncertainties in nuclear data have been considered in many papers, with a recent review of nuclear data being presented by Rowlands /3/.

Uncertainties in the prediction of reactor properties would result in the provision of extra design margins for a guaranteed maximum power output and adequate control of the reactor.

Assessment of data requirements begin with the establishment of target accuracies for the prediction of reactor properties. Judgements are made on the tolerable uncertainty levels which would avoid the need for significant additional margins and contingencies in the design. The sensitivity of these uncertainties on the value of the calculated reactor properties are then evaluated over the energy range of interest. It is then possible to specify those cross-sections which require further calculation and the accuracies required. Energy resolution requirements are determined by the reactor spectrum and structure in the cross-sections.

1.2 Neutron Dosimetry

Neutron dosimetry concerns the measurement of the neutron flux spectrum at specific positions in an assembly and is applied, for example, to correlating material properties (such as radiation damage) to the radiation and temperature environments.

Accurate prediction of radiation damage is of great importance and is applicable to:

(1) The prediction of safe lifetimes for reactor pressure vessels from accelerated tests.

(2) Estimates of rupture in fuel cladding.

(3) Estimates of dimensional changes in graphite moderators.

(4) The design of fast reactor components from data generated in thermal reactors.

Whilst the most urgent need for fluence measurements (i.e. time-integrated dose over long periods) is in the study of radiation damage to materials, such measurements are also relevant to reactor parameters such as the speed of control, reactivity and fuel utilisation.

The impetus for the determination of more accurate activation cross-sections has come from the need for a precise knowledge of the flux profile and spectrum. One handicap has been the lack

of standardisation in the measurement and reporting
of fluence. Two commonly used conventions are the
fluence above 1 Mev and the equivalent fission
fluence.

The first convention is adequate for
correlating damage to fluence, provided the neutron
spectrum is well known and the activation cross -
sections sufficiently accurate. The fission fluence
is the fission neutron flux corresponding to an
observed detector activity. This convention gives
reproducibility in measurements within a facility
and provides a damage index for general comparisons
between facilities having different spectral
distributions. Proper normalisation of results calls
for the publication of the cross - sections used,
for the reconstruction of fluence and the damage
indices. The disadvantage, however, is that a fission
spectrum has to be assumed.

In material damage studies, the variations
introduced by different reactor spectra contribute
to the spread in experimental data. Thus, accurate
neutron spectra are required.

1.3 Activation Detectors

Although a number of methods exist for
the measurement of neutron flux, the limitations of

space, insensitivity to large gamma - radiation intensities and high temperature has led to the wide - spread use of activation detectors.

Three main types of activation detectors exist. The first group is applicable to the detection of thermal and epithermal neutrons, and utilises the (n, γ) reaction.

Fissionable materials provide the second group of activants. The fission products are chemically separated and the radioactivity of a high yield product determined. ^{235}U and ^{239}Pu are used in the detection of thermal neutrons, whilst ^{238}U, ^{237}Np, ^{236}U and ^{232}Th are used to measure the fast neutron flux in the 0.5 Mev to 3.0 Mev energy range. However, high cost and complexity of analysis are disadvantages of these detectors.

The third and perhaps most important group of monitors are those exhibiting (n, p) and (n, α) reactions. The response of these detectors is proportional to the product of the differential activation cross - sections, $\sigma(E)$, and the neutron flux spectrum, $\phi(E)$, such that:

$$R = K \int_0^\infty \sigma(E) \, \phi(E) \, dE \qquad (1)$$

where K is a constant and R the number of reactions induced. The energy limits of response of activation detectors are characterised by the neutron energy

range from which the bulk of the activity is caused.
Table 1 presents the limits of response of some
commonly used fast neutron activation detectors
exhibiting thresholds.

Table 1: Response limits of some threshold detectors

Reaction	90% Energy Limits of Response[*]	
	Lower Limit (Mev)	Upper Limit (Mev)
^{27}Al (n,α)	6.8	11.1
^{54}Fe (n, p)	2.4	6.7
^{58}Ni (n, p)	2.5	6.6
^{238}U (n, f)	1.7	5.5
^{237}Np (n, f)	0.86	4.4

Ref : Dahl et al. /6/

Differences in the response limits
provide the basis for the experimental determinations
of reactor spectra. Nevertheless, in order to deter-
mine the energy response of a detector, a fission
neutron spectrum is assumed. Although rarely
encountered, it provides a convenient convention
for reporting data.

[*] The 90% limit of response represents the fission
specrum energy range from which 90% of the monitor
activity is observed .

Ideal characteristics of a detector require :

(1) An energy response covering the neutron energy range of interest.

(2) A suitable half - life.

(3) Chemical and physical stability , compatible with the irradiation environment.

(4) Insignificant competing reactions.

(5) A daughter product having an activity which is easily isolated and monitored, and having a low burn - up to thermal neutrons.

In the high temperature embrittlement of metals by hydrogen and helium gas produced by the (n, p) and (n,α) reactions, energy thresholds are generally in the 3 Mev to 7 Mev range.* Monitors used in material studies should therefore have a similar response.

* High temperature embrittlement can also be caused by thermal neutrons through ^{10}B (n,α) reactions, where trace quantities of boron are present in structural materials.

Monitors exhibiting short-lived activities are normally used for flux mapping . Reactions of interest for fast flux measurements over long irradiations , on the other hand , have long lived activities . Examples are ^{58}Ni (n, p)^{58}Co , ^{54}Fe (n, p)^{54}Mn, ^{46}Ti (n, p)^{46}Sc and ^{63}Cu (n, α)^{60}Co .

A further important consideration in the selection of a detector is the thermal neutron cross - section of the reaction product . A large cross - section to thermal neutrons would result in burn-up of the reaction product. Apart from the uncertainties induced by inaccuracies in the measurement or estimate of the burn - up effect , the presence of large thermal fluxes (10^{13} n cm^{-2}) would rapidly diminish the effective half - life of the detector . This is particularly important in nickel, ^{58}Co having a large cross - section to thermal neutrons (1650 barns)/8/ .

It has been suggested by Hogg et al /8/ that the ^{46}Ti (n, p)^{46}Sc reaction may provide a promising substitute to the ^{58}Ni(n, p)^{58}Co reaction due to its low burn - up to thermal neutrons (0.25 barns) and the ease of measurement of the burn - up of scandium - 46 in comparison to ^{58}Co and ^{54}Mn . The use of ^{46}Ti as a monitor , however, has been limited by the lack of accurate cross-section data .

Preferred reactions for use in dosimetry are subject to change as more accurate data become available . Further, much emphasis is now placed on reactions exhibiting cross - sections resembling damage processes in structural materials .

One such reaction is the ^{93}Nb(n, n')^{93}Nb reaction for which there are priority 1 requests in WRENDA . However , it is unlikely that the $\pm$ 10 % accuracy requested can be met at the present time . A feasibility measurement carried out by Randl et al / 9 / provided an accuracy of only $\pm$ 25 % , but this is expected to improve .

1.4 The Ti (n, p) Sc reactions

Following a study of (n, p) cross-section measurement requests in WRENDA, the Ti (n, p) Sc reactions were selected for measurement . Standing priority I and priority II requests in WRENDA require accuracies ranging from 5% to 10% (1 standard deviation), mainly for dosimetry applications .

To date, only a limited number of measurements exist . With the exception of the work performed by Smith et al /10/, these measurements do not meet the 5% to 10% accuracy requirements quoted in WRENDA. Furthermore, there has been little agreement between measurements . A review of these measurements follows.

Gonzalez 1961 /11/

The ^{47}Ti(n, p)^{47}Sc cross - section was measured relative to the ^{31}P (n, p)^{31}Si reaction covering the neutron energy range from 2.0 Mev to 3.6 Mev . Typical accuracies of about 13 % are quoted .

Armitage 1967 /12/

^{47}Ti (n, p)^{47}Sc cross - section was measured from 3.5 to 6.0 Mev relative to the ^{58}Ni(n, p)^{58}Co data of Barry /16/, with an absolute measurement at one energy .

Luckic and Carrol 1970 /13/

^{46}Ti (n, p)^{46}Sc cross - section was measured from 4.91 to 7.04 Mev, and the ^{48}Ti(n, p)^{48}Sc reaction from 6.24 to 7.04 Mev at 500 Kev intervals . Cross - sections were computed relative to the ^{56}Fe(n, p)^{56}Mn, ^{27}Al(n, α)^{24}Na and ^{58}Ni(n, p)^{58}Co cross - sections . Accuracies quoted are 15 % .

Ghorai et al 1971 /14/

These measurements were performed using a dynamitron accelerator similar to that used for this work . ^{46,47,48}Ti(n, p)^{46,47,48}Sc measurements

were made relative to the evaluated $^{27}Al(n, p)^{27}Mg$ cross - section data of Grundl /15/ and cover the neutron energy range from 4.1 Mev to 6.1 Mev . Typical accuracies are 17 % to 18 % .

Smith and Meadows 1976 /10/

These measurements are the most comprehensive to date , covering the energy range from threshold to 10 Mev . $^{46,47,48}Ti$ (n, p) $^{46,47,48}Sc$ measurements were made relative to the ^{235}U (n, fission) cross - section for neutron energies up to 4 Mev and relative to the ^{238}U (n, fission) cross - section above 4.0 Mev . Typical accuracies range from 5 % to 8 % for the $^{46,47}Ti(n,p)$ reaction in the 4.0 Mev to 6.0 Mev range , with an accuracy of 12 % at the $^{48}Ti(n, p)^{48}Sc$ reaction threshold .

The data of Luckic et al exhibit marked fluctuations when made relative to different standards at a given energy . Measurements at 6.24 Mev made relative to the $^{56}Fe(n, p)^{56}Mn$ and $^{58}Ni(n, p)^{58}Co$ reactions dirrefed by 67% . The data of Ghorai measured relative to the $^{27}Al(n, p)^{27}Mg$ data of Grundl differed considerably from the data of Smith et al., even though the corresponding $^{27}Al(n, p)$ data of Smith agreed with that of Grundl . The measurements

of Gonzalez also showed considerable differences
from the other measurements .

This work aims to resolve some of these
discrepancies whilst providing a stronger data base
for evaluators . Greater accuracies can be achieved
through improvement in counting statistics (Smith
et al quote 1.0 % to 10 %) with a greater number of
measurements over an energy range, thereby averaging
experimental fluctuations . Further, a more rigorous
approach to corrections is sought . For example, a
better representation of mean neutron energy can be
obtained through a consideration of neutron path
length within a sample rather than merely the energy
profile . Most Ti(n, p) cross - section measurements
to date have been made relative to secondary
standards which in turn have been measured relative
to either the ^{1}H(n, p) or the ^{235}U(n, fission) cross
- sections . Hence, measurements relative to either
of these standards should provide greater accuracy.

1.5 Experimental method

The (n, p) reactions can be monitored
through either direct on-line measurements of the
emitted charged particles, or through activation
methods whereby the decay of a radioactive reaction

product is monitored . The direct on-line method
has been demonstrated by Kojnin and Lauber / 4 /
and is particularly suited to measurements where
the reaction product is either stable or exhibits
a very long or very short half life . Nevertheless,
the activation method was opted for in preference
to the direct measurement in view of the greater
experimental difficulties anticipated in on-line
techniques .

Irradiations

Irradiations were performed using the
Birmingham Radiation Centre 3 MV Dynamitron
accelerator /60/. Titanium discs (99.99 % pure) ,
20 mm in diameter and 2 mm thick were placed at
distances of 2.0 cm and 2.5 cm from a $D(d, n)^3He$
neutron target . The experimental arrangement used
is similar to that used by Smith et al and is
depicted in fig. 1.1 .

NEUTRON
SOURCE

TITANIUM
SAMPLE

^{235}U DEPOSIT
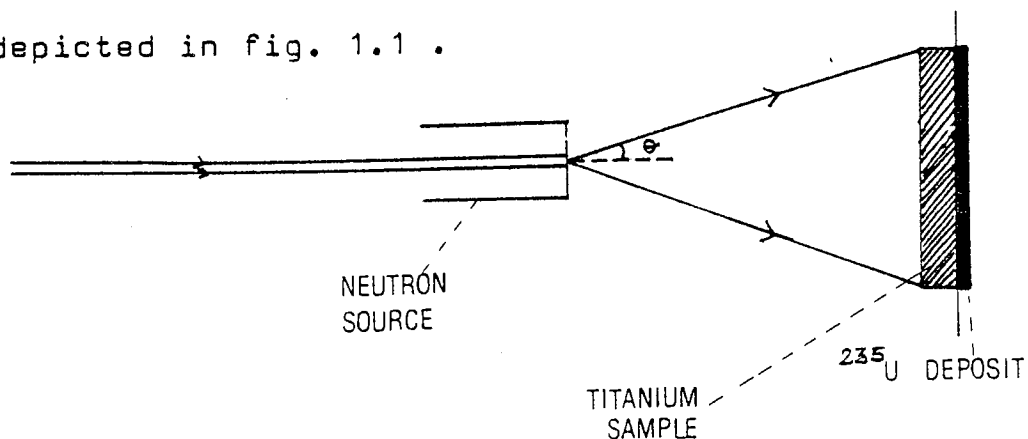
FIG. 1.1: EXPERIMENTAL ARRANGEMENT FOR SAMPLE IRRADIATIONS

The selection of ^{235}U as a standard in
the measurement of neutron flux was made following
a survey of methods suitable for accurate flux
determination . Methods of flux measurement are
discussed in the following chapter .

CHAPTER 2
THE MEASUREMENT OF
FAST NEUTRON FLUX

CHAPTER 2

The Measurement of Fast Neutron Flux

In neutron cross - section measurements, a major contribution to the accuracy of the measurement relates to the determination of neutron flux .

Methods of neutron flux measurement may be classified into two groups, namely, absolute and relative methods . Absolute methods are not dependent upon the knowledge of any particular reaction cross-section . Relative methods, on the other hand, are made relative to standards of which the cross - section is accurately known . These methods will be discussed further .

2.1 Absolute Methods of Measurement

Absolute methods are generally made through three techniques : (1) associated particle, (2) associated activity and (3) total absorption .

Associated particle measurements

Neutron production from the frequently used reactions $D(d, n)^3He$, $T(p, n)^3He$ and $T(d,n)^4He$, is accompanied by the simultaneous production of charged particles . The detection of these particles forms the basis for neutron flux measurements .

The associated particle method has been
widely used in the measurement of 14 Mev neutron
fluxes from the $T(d, n)^4He$ reaction . The success
of this technique for 14 Mev neutrons (E_d=150 Kev)
is related to the isotropic distribution of the
associated alpha particles . These alpha particles
may be detected using thin-window proportional
counters or solid state detectors . The latter are
preferred from the point of view of small size and
superior energy resolution, but suffer from radiation
damage . A knowledge of the solid angle subtended
by the charged-particle detector, the number of
alpha particle counts and the anisotropy factor for
their distribution provides the neutron flux .

When the $D(d, n)^3He$ reaction is used to
generate neutrons in the 3 Mev range ($E_d < 200$ Kev),
the associated particle method can also be applied
for accurate flux measurements, due to the isotropic
distribution of the ^3He particles and neutrons . At
higher energies, the distribution is increasingly
anisotropic and thus the angular distribution has
to be taken into consideration, and provides an
extra source of uncertainty .

A competing reaction to the $D(d, n)^3He$
reaction is the $D(d, p)^3H$ reaction, having a
similar cross - section at low energies . Detection

of the protons provides an alternative to the detection of the ^{3}He particles, made possible by the higher energy of the protons . A thin aluminium absorber interposed between the neutron source and the charged-particle detector, the thickness of which is selected to absorb the ^{3}He particles but not the protons, can be used to improve discrimination between the two particles . Alternatively, the two particles may be magnetically separated .

Similar methods can be applied to the measurement of neutron fluxes from the T(p, n)^{3}He reaction, developed initially by Liskien /17/ .

Limitations of the associated particle methods relate to scattering of the primary bombarding particles and the associated particles in the target backing and chamber . The scattered particles have intense fluxes, creating radiation damage in solid state detectors and also pulse pile-up .

The use of analysers combining electric and magnetic fields can be used to eliminate these effects, but are complicated by charge exchange . For the D(d, n)^{3}He reaction, unbacked self-supporting deuterium targets in the form of deuterated polyethelyne targets have been developed /18/ to reduce scattering effects . However, one

difficulty with these targets is the limitation of accelerator beam currents to a few nanoamps, hence limiting the neutron flux . A further method of background discrimination is coincidence counting, where the neutron and associated particle are detected in coincidence .

Associated Activity

Certain reactions, such as the $^7Li(p,n)^7Be$, $^{51}V(p, n)^{51}Cr$, $^{57}Fe(p, n)^{57}Co$ and $^{65}Cu(p, n)^{65}Zn$, result in reaction products which are gamma active. Measurement of the induced activity allows for the determination of neutron flux . A $MnSO_4$ bath, for example, can be used to determine the total neutron yield related to target activity . Subsequent measurements of target activity provide a measure of neutron flux . Variations of accelerator beam intensity and reaction yield are averaged out .

Total Absorption methods

Total absorption methods rely upon absorption of essentially all neutrons incident upon the detector, whatever the neutron energy . Although long counters can provide these characteristics, they are normally limited to relative flux measurements . This is due to uncertainties in the

evaluation of the response of the long counter/7/, due to the heterogeneity and quality of the moderator employed in the counter .

Some of the total absorption detectors in current use are the manganese and vanadium baths, and the black and gray detectors . The earliest is the manganese bath used to calibrate standard neutron sources . The neutron source is placed at the centre of a large vessel containing an aqueous solution of $MnSO_4$. Neutrons are moderated and subsequently captured by the manganese, leading to the 2.58 hour activity of ^{56}Mn . Following irradiation, the ^{56}Mn activity from a uniformly distributed solution is absolutely counted . Accuracies of about 2 % are reported, associated mainly with the activity measurement, hence greater accuracies are achieved when this method is used for comparison of source strengths .

The gray and black detectors are designed to provide prompt neutron detection whilst maintaining a fast response for timing purposes .

A gray neutron detector comprises a moderator-manganese or vanadium mixture with an entrance channel terminating at the centre of the detector . Neutrons are moderated and captured . The capture gamma rays are detected at the surface by

a sodium iodide detector . A disadvantage is the slow time response to neutrons at higher energies .

The black neutron detector of Poenitz /19/ serves to overcome the slow response of the gray detector and consists of a plastic or liquid scintillator with an entrance channel terminating at the centre . Neutrons from a collimated beam lose essentially all their energy in successive scattering collisions before falling below an energy threshold or escaping from the system . The scintillation light output from hydrogen and carbon recoils is detected by several photomultipliers . The probability for total energy loss is 99-95 % in the 1 to 10 Mev range . Thus, extrapolation to zero pulse height is made more accurate due to the relatively small number of small pulses in comparison with conventional recoil scintillation detectors .

2.2 Relative Methods of Measurement

Neutron fluxes may be measured from a knowledge of the neutron cross-section of a suitable standard . The pre-requisites for a standard are an accurately known, slowly varying cross-section and a reaction product providing high yield and suitability for counting .

In the neutron energy range 100 Kev to 20 Mev, the ^{1}H(n, p) reaction provides a convenient standard . The neutron-proton scattering cross-section is known from transmission experiments to an accuracy of better than 1% and is the only standard of which the cross-section is known to such an accuracy over this energy range .

The scattering of neutrons by protons is isotropic in the centre of mass systems for neutron energies up to 10 Mev and approximately so in the laboratory system . Further, the energy of the recoiling protons, E_p, is related to neutron energy, E_n, by the equation :

$$E_p = E_n \cos^2 \theta \qquad \text{---------}(2.1)$$

Given an isotropic angular distribution of the protons, the energy distribution of recoil protons from a monoenergetic neutron source will be rectangular from zero proton energy up to $E_p = E_n$ ($\theta = 0$) . An ideal proton recoil spectrum is shown in fig. 2.1 . Unfortunately, the ideal rectangular distribution is not observed in practice . Experimental spectra exhibit a low energy tail due to gamma ray and noise pulses, and rounding off at the upper limit due to the spread in neutron energy and the detector resolution . This is illustrated

in fig . 2.1 :
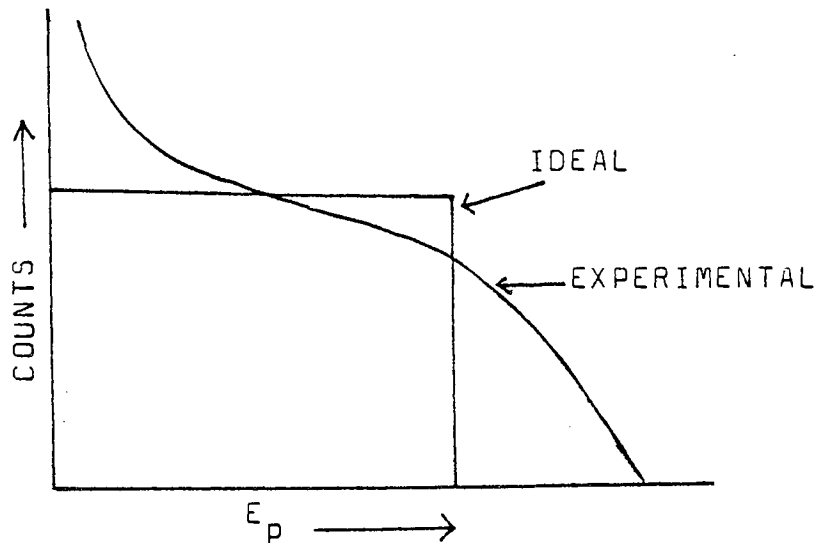
Fig. 2.1 : An idealised proton recoil spectrum and
an experimental spectrum .

Two main types of detectors in common
use for the detection of recoil protons are propor-
tional counters and scintillation counters .
Proportional counters will be discussed first .

Proportional Counters

In a proportional counter, the detection
medium is a hydrogeneous gas such as methane (CH_4),
at several atmospheres of pressure . Gas amplifi-
cation factors of 20 or 30 are commonly used to
overcome interference from noise pulses . An
auxilliary electrode accurately defines the sensitive
volume . The sensitive volume is important from the
point of view of flux measurements . Further, some

protons will cross the boundary of the sensitive
volume before expending their full energy in the
sensitive volume, whilst recoils produced outside
the sensitive volume will expend part of their
energy in the sensitive volume . The sum effect is
an increase in the number of small pulses and a
rounding off at the upper end of the energy
distribution . An extensive review of response
functions for recoil proportional counters of
different designs may be found in ref. /20/ .

The total proton counts are obtained
through a procedure involving the fitting of a
threoretically calculated spectrum, taking into
account the detector response . The fitting allows
extrapolation of the proton counts into the region
where gamma rays and noise pulses are observed .

The upper energy limit (approximately
3 Mev) of usefulness of gas-filled proportional
counters is set by the proton range in the gas .
For a cylindrical counter,
when the proton range exceeds the counter diameter,
considerable wall and edge effects are observed .
Although it is possible to increase the counter
diameter and gas pressure above ten atmospheres ,
the practical limit is set by increased sensitivity
to gamma rays and the high voltage requirements .

Scintillation Counters

Scintillation counters provide the
advantages of reduced wall effects, greater detection
efficiency to neutrons and fast response for time
of flight experiments .

A disadvantage of organic scintillation
detectors is the non-linearity in light output with
energy which has to be corrected for . Further, the
detection efficiency decreases with increasing
neutron energy . Although the detection efficiency
can be improved through increasing the detector size,
an important factor which limits the size is the
pulse rate due to gamma rays interacting within the
detector . Hence, the scintillator must be kept
small in order to avoid pile-up of gamma pulses .
The light output of organic scintillators is always
higher per unit energy for electrons than for heavy
charged particles . Hence, the problem of gamma
discrimination is made more severe .

Where gamma ray pulse pile-up is not
severe, pulse shape discrimination may be employed .
In the majority of organic scintillators , prompt
flourescence provides most of the observed
scintillation light . A longer lived component
corresponding to delayed flourescence is also

observed in some cases . The fraction of light which appears in the slow component often depends on the nature of the exciting particle . Certain organic scintillators, including stilbene crystals and a number of commercial liquids and plastics, are particularly suitable for pulse shape discrimination due to the large differences in the slow component for fast neutrons (recoil protons) and gamma rays (fast electrons) . Reviews of pulse shape discrimination properties may be found in ref. /21 - 25/ .

Proton Recoil Telescopes

At the upper limit of the energy range of conventional recoil proportional counters, problems relating to spectrum unfolding and extra - polation of the spectrum to zero pulse height can be overcome through the use of recoil telescopes .

In the telescope, recoils limited to the forward cone only are recorded ($\theta \simeq 0$) . This provides a response exhibiting a simple narrow peak. A telescope may comprise two or three detectors in which coincident pulses only are recorded . Alternatively, a solid state detector subtending a small solid angle in the forward direction provides a simpler experimental arrangement (see fig. 2.2).

The superior resolution of solid state

detectors is an advantage when this technique is
used for neutron spectroscopy .

(a)

(b)
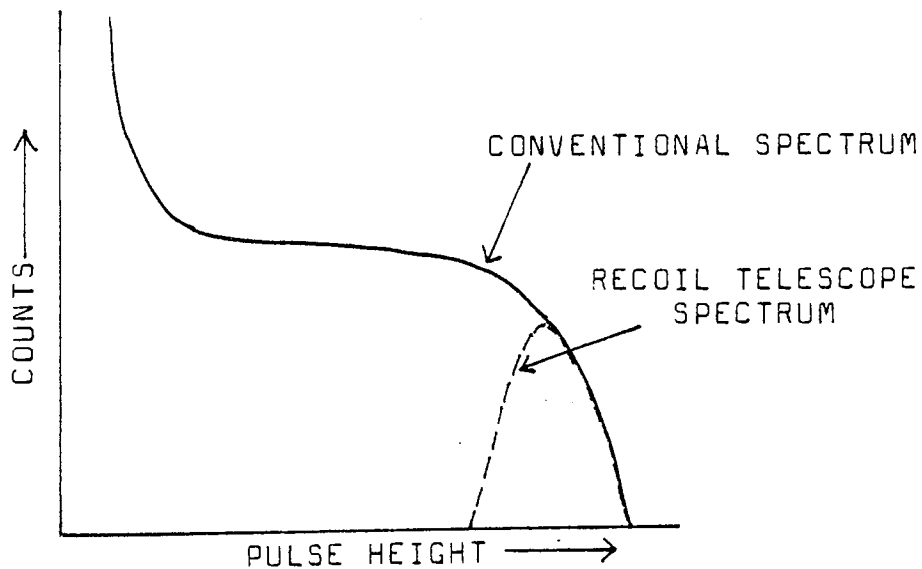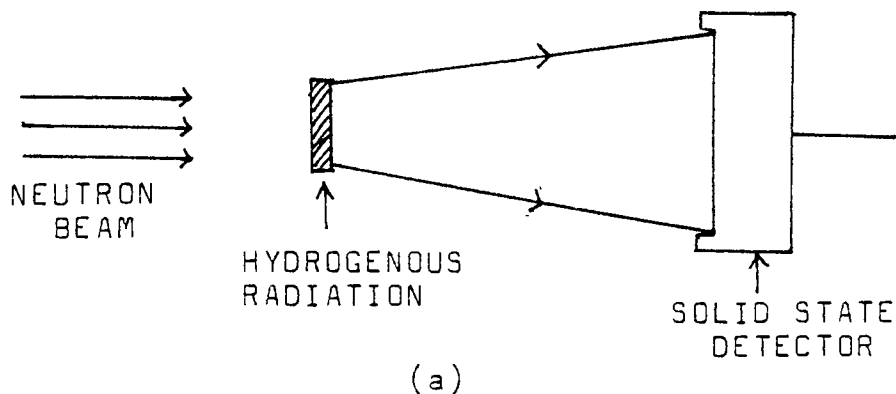
Fig . 2.2 (a) Recoil telescope (schematic) using solid
state detector .

(b) Comparison of pulse height distributions
between conventional recoil spectra and
recoil telescope spectra .

The main disadvantage of recoil telescopes is the necessarily low detection efficiencies due to the small solid angles subtended and the limitation on radiator thickness .

2.2.1 Other Standards

Although the ^{1}H(n, p) scattering cross - section is well known below 100 Kev, difficulties relating to the measurement of low energy protons requires other standards . In the 10 Kev to 100 Kev region, standards based on the ^{6}Li(n, α)^{3}H , ^{10}B(n, α) and ^{3}He(n, p)^{3}H reactions are available . However, the cross - sections for these reactions are not as accurately known as the ^{1}H (n, p) cross - section . Nevertheless, the ^{6}Li(n, α)^{3}H reaction is a commonly used standard between 100 Kev and thermal energies . Lithium glass scintillators provide a convenient detection mode ; the lithium content is commonly determined through low energy neutron transmission experiments . Typical accuracies of 2% in flux measurements can be achieved, excluding· the uncertainty in the ^{6}Li(n, α)^{3}H cross-section .

Uranium - 235

Thus far only primary standards have been discussed . In many cross - section experiments ,

secondary standards have been used as alternatives .
The term secondary refers to the fact that the
cross - sections of these standards have been
measured relative to the primary standards . Of
these secondary standards, the ^{235}U(n, fission)
cross - section is the most widely used .

Fission counting is generally simpler
and can be performed to greater accuracies in
comparison with recoil proton counting . The
advantages of fission counting relate to the large
amount of energy carried by the fission fragments
(totalling 160 Mev) . It is therefore possible to
discriminate against other competing reaction or
events due to background or counter contamination .
A further advantage is the flat response of the
fission cross - section over the fast neutron
energy range .

In the measurement of neutron flux using
^{235}U as a standard, the major sources of systematic
error lie in the assay of the fissile deposit and
the uncertainty in the fission cross - section data
used . A recent review of the status of the ^{235}U
fission cross - section has been presented by
Patrick /26/ . Whilst measurements in the 0.1 to 3.0
Mev range are in good agreement to within 2%
accuracy, a spread in the experimentally measured

values above this energy range provide an accuracy

of only 3% . Nevertheless, the importance of the

fission cross - sections to the nuclear power

programmes has led to repeated measurement and

revaluation, particularly the $^{235}U(n, f)$ cross -

section, since most other fission cross-sections

are measured relative to this standard . Thus ,

measurements made relative to a fission cross-section

can be renormalised as data accuracy improves .

Fission counting and fission counter

design will be discussed in the following chapter .

CHAPTER 3

FISSION COUNTER DESIGN

CHAPTER 3

3.1 A Review of Recent Trends in Fission Counter Design.

Trends in fission counter design have developed over the past decade with a view to increasing time resolution in Time of Flight Techniques to provide alpha - background suppression. The impetus has been the requirement for fission cross - section data of highly active isotopes. These nuclear data requirements have been motivated by the following :

(1) Improved safety requirements for fast reactors, calling upon reliable calculations of the inventory of hazardous isotopes as a function of fuel burn - up.

(2) Waste Management considerations, where problems arise with the long term hazards of highly active waste .

(3) The need for quantitative calculations for neutron economy under high burn - up conditions.

It should be noted that fission cross - section measurements of isotopes exhibiting spontaneous fission can only be carried out using

the Time of Flight Technique, where the time
resolution requirements are for resolutions equal
to, or better than, the neutron pulse widths used .

3.1.1 Gas Scintillation Counters

A revival in the use of gas filled
scintillation fission counters could be observed
from the early seventies, initiated by rapid
developments in heavy ion physics . For such
experiments, detectors are required which combine
good energy and time resolutions, insensitivity to
radiation damage and high detection efficiencies .
While only poor energy resolution is achieved with
plastic scintillators, gas scintillators exhibit
time and energy resolutions sufficient for
discrimination between alpha - particles and fiss-
ion fragments for isotopes such as U - 235 with
decay rates of approximately 100 $s^{-1}mg$.

At higher alpha activities, when isotopes
like Pu - 239 are investigated, pulse pile - up
results in the merging of the pulse height differ-
ence . Additional alpha suppression is then
obtainable by observing both fragments in
co - incidence, requiring thin samples (500 ug cm^{-2})
and thin backing foils (100 ug cm^{-2}) . A difficulty
arising from the co - incidence counting technique,

observed by Kappeler / 27 /, is radiation damage in
the backing foils, reducing the life time of the
foils to two or three months . Thus, restrictions
are imposed on the use of co - incidence counting .
However, recent developments of gas scintillation
detectors for heavy ion experiments by Mutterer et
al / 28 / showed promising results, with energy
resolutions of 2.2 % for Xenon-136 per 1.4 Mev amu
and time resolutions of 210 parsec . These results
are comparable to the performance of solid state
detectors, whilst not having the limitation of
radiation damage .

3.1.2 Gas Ionisation Counters

Whilst the differences in kinetic energy
between alpha - particles and fission fragments are
about 12 times, for specific energy loss this ratio
is sixty times . This is illustrated by the well -
known energy loss curves of fig. 3.4 . This effect
can only be utilised in parallel plate ionisation
counters .

These detectors are sometimes used in
fission cross - section measurements incorporating
the use of multiparallel fission-plates so that
considerable amounts of fissile material can be
used to improve fission counting statistics/29, 30/.

In the past decade considerable improvements in the time resolution of parallel plate ionisation chambers have been achieved, with 1 nanosec. being reported /31/. Behrens and Brown /32/ have shown that alpha suppression in these detectors is sufficient for measurements on Am-241, but for significantly higher rates, the alpha discrimination properties are lost due to those alphas which are emitted under small angles to the surface of the plates and, therefore, have a long geometric path length in the chamber . Budtz - Jorgensen and Knitter /33/ avoided this effect by introducing a collimator grid in front of the sample as illustrated by fig. 3.1 . Only fragments which are emitted with angles larger than approximately 35 degrees to the surface are able to penetrate the collimator . The collector electrode is an 8 micron aluminium foil, sufficient to allow the passage of alpha particles but not fission fragments . The electrode spacings are so arranged as to allow alpha particles to deposit their energy on either side of the electrode . Thus only a small nett charge is collected by the electrode, reducing the effective pulse height for alpha particles . This detector operates with alpha particle rates of up to 5×10^{8} s^{-1} .
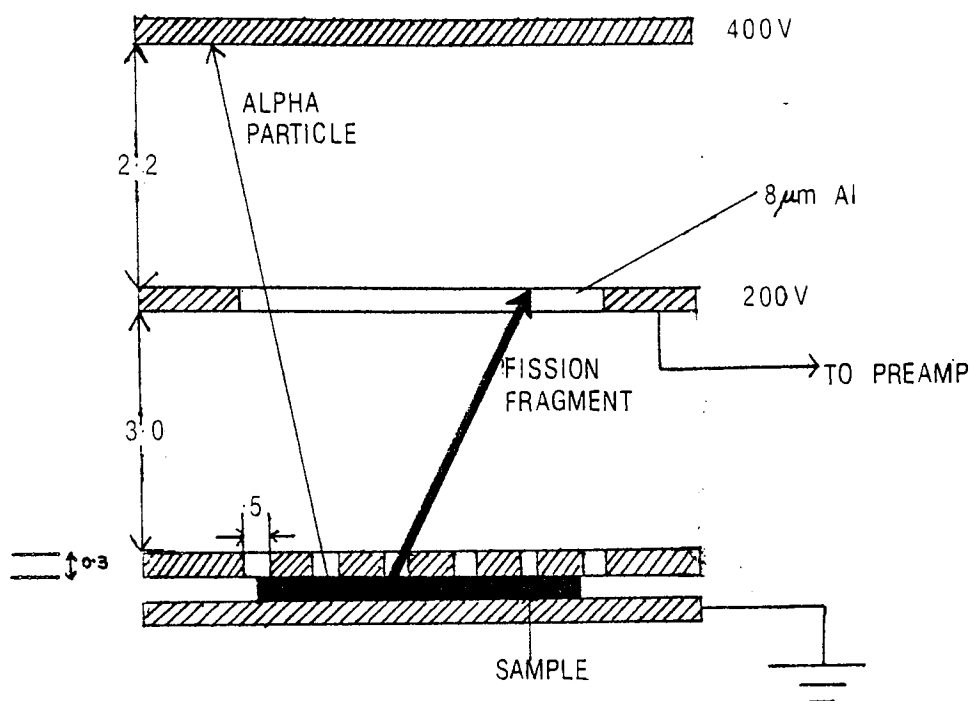
Fig. 3.1 : The ionisation chamber of Budtz-Jorgensen
and Knitter . (Schematic sketch)

Dabbs et al /34/ have developed another
solution to the alpha background problem . A
chamber was designed with hemispherical plates as
shown in Fig. 3.2 . The two arrows indicate the
maximum / minimum track length ratio limitation
imposed by this geometry . Setting this ratio equal
to 3, a pulse height difference factor of 15 is
obtained between fragments and alphas . Alpha-particle
activities of up to $10^8 s^{-1}$ can be tolerated, but
the time resolution is comparable to conventional
ionisation chambers .
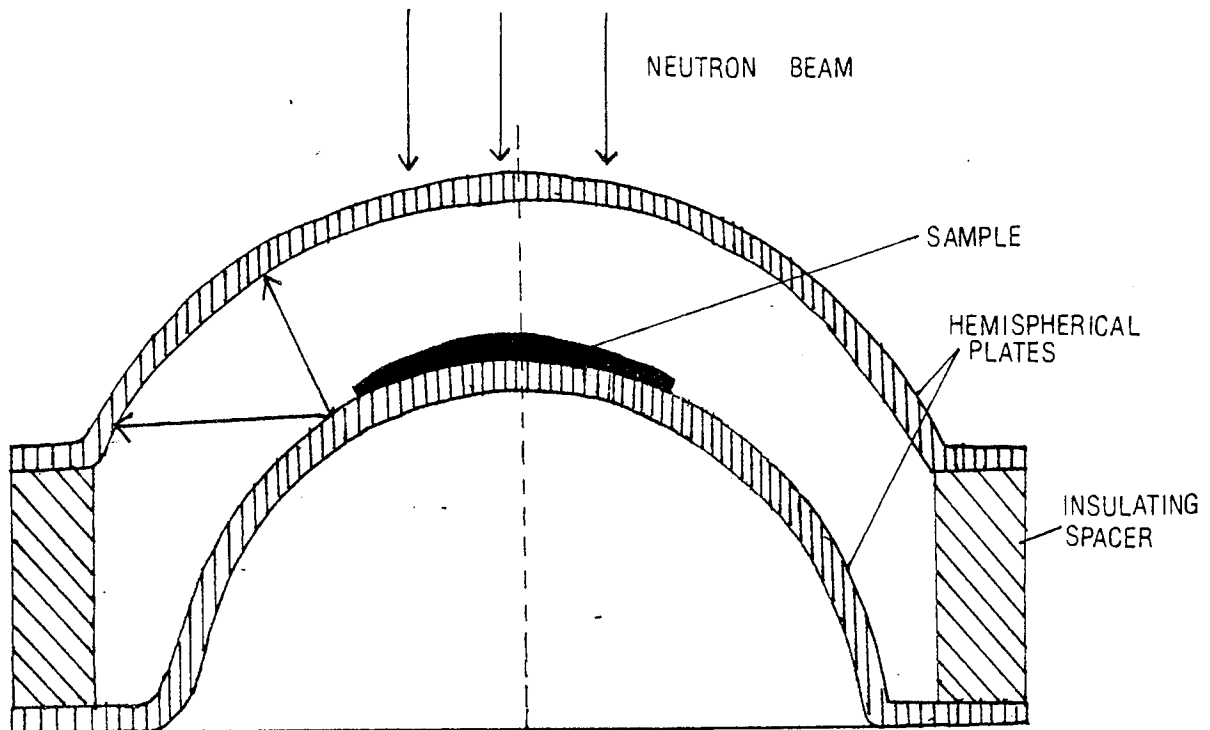
Fig. 3.2 : The ionisation chamber of Dabbs et al .
(Schematic).

3.1.3 Parallel Plate Avalanche Detectors

The requirement for subnanosecond
timing in heavy ion physics has led to the develop-
ment of these counters with time resolutions of
better than 0.3 nsec .

Kazerouni /35/ developed a counter of
similar construction to that of Dabbs, but using
10 mbars of butene . By decreasing the bias voltage,
the ratio between fragment and alpha-particles was found
to increase rapidly to values above 50 until the
alphas disappeared in the preamplifier noise . This

behaviour is explained by competing columnar

recombination in the weak ionisation tracks of

alpha particles which prevent an avalanche below

a critical voltage . A time resolution of less

than 350 psec. was observed with an alpha suppres-

sion factor of 10 observed over two days .

A further illustration of the versatility

of avalanche detectors is in the measurement of

fragment angular distribution . Just et al /48/

developed a position sensitive parallel plate

avalanche detector which allows the recording of

fission events and their angular distribution

simultaneously . The time resolution was 250 psec.

and. the position sensitivity, better than 0.4 mm.

Aston University

Content has been removed for copyright reasons

Fig. 3.3 : Anode strip pattern in the position

sensitive avalanche counter of

Just et al .

The position sensitivity is obtained by dividing the anode plate into a strip pattern corresponding to angle intervals of 10 degrees .

3.1.4 Nuclear Track Polymers

This method is restricted to isotopes which do not decay by spontaneous fission, as the Time Of Flight Technique is not applicable .

Polymers have good alpha discrimination . The threshold for track formation differs for various plastic films corresponding to a critical value of Z/β where Z is the particle charge and β the ratio of particle to light velocity . Thresholds of common detector materials are Z/β =20 for CR39*, 30 for cellulose nitrate, 40 for cellulose acetate and 65 for Lexan /36/ . Alpha particles of energy 5.5 Mev have a ratio Z/β =37, so the latter two materials may be used.

* CR39 is the commercial name for the polymer whose monomer is the oxydi-2, 1 ethanediyl di-2 propenly diester of carbonic acid .

3.2 Design Considerations For The 2π Gas Flow Fission Counter Used In This Work

The use of U-235 in this work as the neutron flux monitor or standard does not pose the problems associated with high alpha activities discussed in the previous section . Furthermore, the requirements for a thin uranium-235 deposit, to obtain reduction of fragment self - absorption, has meant that only alpha activities of 500 s^{-1} need be dealt with in 2π geometry .

The ungridded parallel plate ionisation counter is the simplest and cheapest type of fission counter to construct . It can be made both rugged and reliable and aluminium and magnesium are often employed since their neutron activation products decay quickly . The simple geometry permits an accurate calculation of counting efficiencies . Energy resolutions, on the other hand, for reasons to be discussed in Chapter 4, are modest, but this is not an essential requirement . The accuracy with which neutron fluxes can be measured is limited primarily by the uncertainty in the U-235 fission cross - section, currently at approximately 3% over the energy range relevant to this work, 4 Mev to 5Mev.

Other alternative modes to fission fragment detection are through the use of solid

state detectors and proportional counters .

In gas - filled proportional counters,
the fissile material is a solid deposit coated on
the inner walls . The electrode is charged with
sufficiently high positive potential to bring the
tube into the proportional region of operation .
Typical gas pressures in such chambers are much
below atmospheric to reduce the requirements for
high field intensities whilst effecting discrimin-
ation between alpha - particles and fragments .

The advantage of such a counter arises
from the multiplication factors of the order of a
hundred or more obtained . Electronic and background
noise is not a problem and less amplifier gains are
required . The disadvantage, however, is the lack
of stability to anode voltage variation . Whereas
it is common practice to make boron (n, α) counters
of the proportional type, fission counters are used
in the form of ionisation chambers due to the large
fragment energies .

Solid state detectors have the advantages
of good energy and time resolution but suffer
radiation damage from fission fragments . Further-
more, 2π geometry is not easily obtained and
therefore, such solid state detectors are more
commonly used in low geometry counting . Low geometry

fission counting, however, was not considered
feasible due to the low counting statistics expected
and anisotropy in the fission fragment angular
distribution above neutron energies of 5 Mev .

3.2.1 Range_and_Ionising_Properties_of_Fission_Fragments

In fission counter design, the relation-
ships between range and ionisation density are of
interest . Bruntton and Hanna /37/ having studied
fission fragment distributions from U-235, report
most probable light and heavy fragment energies of
94.5 Mev and 60.2 Mev respectively . Both fragments
carry a total most probable kinetic energy of 156
Mev, with practically all fragments carrying
energies of greater than 40 Mev .

At the moment of creation, fragments
carry a nett positive charge through the loss of
several electrons . Although the most probable
charges at the moment of creation are not known,
the charges carried by fragments at the start of
their range are found to be dependent upon the
electron capture and loss mechanisms and therefore
the medium traversed . Lassen /52/ reports most
probable charges of 16 and 15 for light and
heavy fragments in argon, whilst larger charges

were observed in solids, beryllium yielding 22 and 23 respectively . Whilst small differences were observed between gases, marked differences were observed in solids . The measurements of Fulmer and Cohen /38/ on equilibrium charges in gases show a general agreement with those of Lassen . Fragment charge was a linear function of velocity in all gases investigated . A theoretical study of electron capture and loss mechanisms was made by Bell /39/ and equilibrium between the rates of capture and loss found to be attained at fragment velocities approaching that of the most loosely bound orbital electron in the fragment . As fragments lose energy through ionising collisions, with a consequent reduction in velocity, the rates of electron capture increase over that of electron loss . Hence the nett charge decreases with velocity until an equilibrium charge is reached .

From the work of Bohr, Bethe and others, documented by Wilkinson /40/ the rate of energy loss with distance of a particle of charge Ze traversing matter containing n atoms/cm^{-3} is :

$$-\frac{dE}{dx} = \frac{4\pi Z^2 e^4}{mv^2} \, n \, Z \, \log \left\{ \frac{2mv^2}{I} - \log(1-\beta^2) - \beta^2 \right\} \quad --(3.1)$$

where E is the particle energy, v its velocity,

m the electron mass, and $\beta = v/c$. Z is the atomic
number of the element traversed and I, considered
to be the average excitation energy of the atom, is
best determined empirically . As the fragments lose
velocity and gain electrons, the fall in nett
charge z more than compensates for the fall in v
in equation (3.1), and hence the largest rate of
energy loss is at the beginning of the track . Only
towards the end of the track does the ionisation
density rise again due to the decreasing v term .
This is illustrated in Fig. 3.4 .
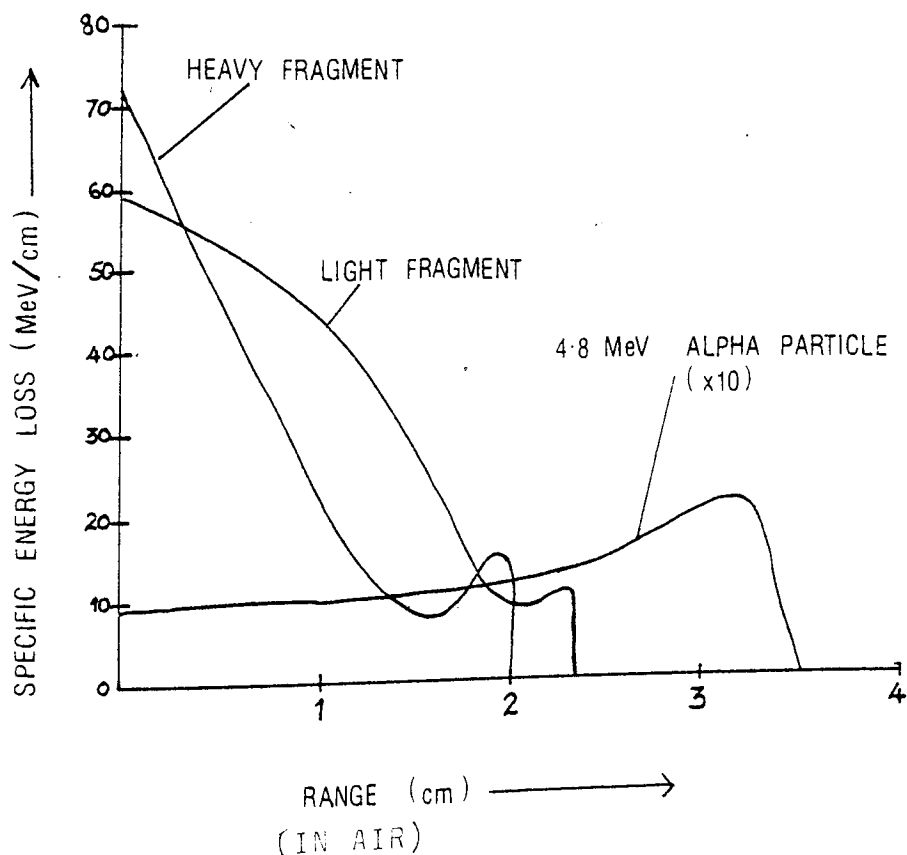
Fig. 3.4 : A plot of ionisation density versus range
for alpha particles and fission fragments.

Alpha partcles, on the other hand, exhibit a large
ionisation density towards the end of their tracks .

An appropriate choice of source -
detector spacing (typically 0.5 cm to 2 cm in argon)
for U-235 and U-238 chambers would therefore effect
discrimination between alpha - particles and fission
fragments .

A further consideration of ionisation
by fission fragments was observed in an analysis by
Ling and Knipp /41/ . The distribution in the ratio
of the ionisations produced by two associated
fragments is broader than the distribution in the
ratio of energies obtained from their masses . This
observation is supported by evidence that the mean
kinetic energy of fission fragments determined
calorimetrically is appreciably higher than the
value deduced from ionisation yields . Schimitt and
Leachmann /42/ suggest an expression representing
fission fragment energy as :

$$E = W_\alpha \, J_0 + E_0 \qquad \text{------------(3.2)}$$

where W_α is the mean energy deposited per ion -
pair formed for alpha particles in the gas, J_0 the
total observed ionisation (total number of ion -
pairs) and E_0 is approximately 5.7 Mev and 6.7 Mev
for light and heavy fragments respectively, and

represents the energy losses to nuclear collisions as fragments approach the end of their range .

3.2.2 The Mean Energy Per Ion Pair Formed, "W"

The requirements for maximum pulse output per unit energy deposition calls for a consideration of the filling gas properties . The output pulse per unit energy in an impurity-free gas is primarily dependent on two factors, the detector capacitance and the mean energy required for the formation of an ion - pair W . Numerous measurements for W have been performed and reported. Table 3.1 presents the W value for common gases used in ionisation chambers .

Xenon, krypton and argon present the lowest W values and as such would provide corres - pondingly large ionisation yields per unit energy deposited . Xenon and krypton however, are expensive .

For optimum operation of ionisation chambers, it is often desirable to employ a mix - ture of gases, as will be apparent from the proceeding sections. Detailed investigations of various gas mixtures with argon as the main constituent have been carried out by Melton, Hurst and Bortner /45/ . They observed that a particular

concentration for each gas introduced gave minimum
values of W for the mixture .

Table 3.1 : <u>W VALUES IN ELECTRON VOLTS PER ION</u>

   <u>PAIR FOR ALPHA PARTICLES IN GASES</u>

Hydrogen	37.0
Helium	42.7
Nitrogen	36.6
Oxygen	32.5
Neon	36.8
Argon	26.4
Krypton	24.1
Xenon	21.9
Methane	29.0
Boron triflouride	36.0*
Air	35.5

Ref. Jesse and Sadausskis /43/

    * Bortner and Hurst /44/

Following this investigation, Bortner and Hurst
provide an effective value W_{ij} represented by the
empirical equation :

$$1/W_{ij} = (1/W_i - 1/W_j)Z_{ij} + 1/W_j \qquad \text{--------(3.3)}$$

where $Z_{ij} = P_i/(P_i + a_{ij}P_i)$, P_i is the partial
pressure of the gas having a value W_i and P_j is

the partial pressure of the gas having the value W_j . The constant, a_{ij}, is equal to the ratio of the stopping powers S_j/S_i for the component gases in some instances but is normally considered as an empirical constant .

3.2.3 Electron Attachment

Modern ionisation chambers are invariably operated in the electron collection mode, in preference to the positive ion mode . The disadvantages of the latter are pulse pile - up and microphonics (mechanical oscillations at acoustic frequencies) in the necessarily slow amplifiers used . Correspondingly, the use of fast amplifiers with a frequency response sensitive only to the high frequency portion of the pulse, facilitates the electron collection mode . The contribution to detector performance from the ancillary electronics will be further discussed in Chapter 4 .

In the electron collection mode, a consideration of effects due to the presence of electronegative impurities is of importance, since electrons captured by electronegative impurities have reduced mobility and would therefore be lost to the signal .

The most common electronegative
impurity encountered in a laboratory environment
is oxygen . In the use of solder fluxes, hydrogen
chloride may be introduced as a constituent of
certain fluxes . Silicon tetraflouride is also a
common impurity in the presence of boron
triflouride .

McCutchen /46/ observed appreciable
attachment losses in pure argon upon addition of
0.1% oxygen . Further addition of 2% carbon dioxide
however, diminished these losses . This is
attributed to a reduction in electron agitation
energy following inelastic collision with polyatomic
molecules to a value close to the minimum for
attachment cross - section h, in fig. 3.5 .
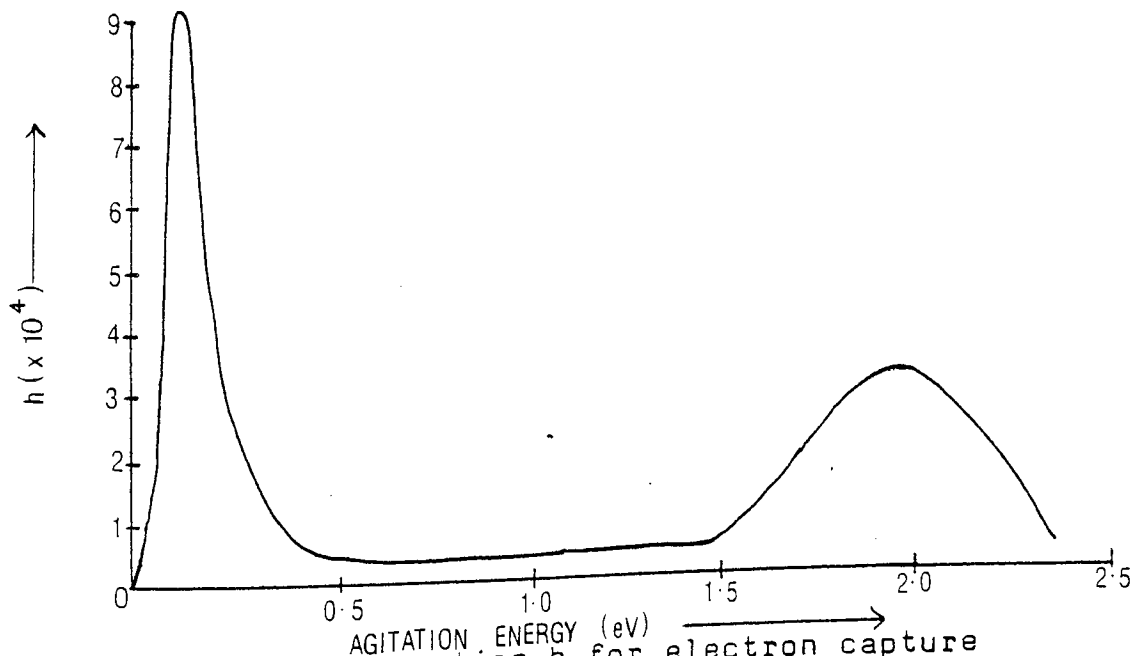
Fig. 3.5 : Cross - section h for electron capture
in oxygen .   Ref. Wilkinson /40 / .

In collisions between electrons and neutral atoms, the probability of electron attachment h varies as a function of the agitation velocity (physical velocity of the electrons) .

Whilst different results are observed by experimenters in pure argon, reproduceable results were attained in mixtures incorporating a polyatomic gas . However, great care should be exercised in the use of carbon dioxide in closed environments due to the dissociation of carbon dioxide molecules .

From a treatment by Bistline /47/, the loss of signal due to electron attachment may be quantitatively expressed as :

$$S_o - S \approx 1/2(Sx/\lambda_c) \qquad\qquad \text{------------}(3.4)$$

where S_o is the voltage pulse in the absence of electron capture and is given by :

$$S_o = (N_o e/Cd)x \qquad\qquad \text{-----------}(3.5)$$

N_o is the total number of electrons released in ionisation, e, the electronic charge, C, the detector capacitance, d, the source - electrode spacing and λ_c , the electron attachment mean free path , x is the distance from the point of origin of the electron to the collector .

Application of equation 3.4 to a typical
parallel plate configuration, with appropriate
values for electric field E, to the presence of
1 part in 10^5 of oxygen impurity, would indicate
a loss of approximately 1% in signal . However,
at high pressures the purity requirements are
more stringent .

3.2.4 Ion Pair Recombination

A further contribution to signal loss,
commonly attributable to the presence of electro-
negative impurities, is recombination . The three
main processes, volume, preferential and columnar
recombination, are discussed by Wilkinson /40/.

Volume recombination relates to
recombination between ions from different tracks
simultaneously produced in the gas . The rate of
recombination is shown to be proportional to the
product of the negative and positive ion densities.
Contributions from volume recombination, however,
are negligible in pulse chambers as pulse pile -
up would predominate resulting in signal loss
prior to this limit .

Preferential recombination relates to
recombination between the original ion pair .
This occurs when an ejected electron is captured

close to its point of liberation by a neutral

atom, forming a negative ion, with subsequent

recombination with the parent positive ion .

Wilkinson reports that, with the exception of

high pressures and the presence of electro -

negative impurities, such events are improbable.

Columnar recombination between heavy

ions along the track of an ionising particle,

however, is a common process requiring consider-

ation in the presence of electronegative

impurities . A correction for the resulting

charge loss can be made by the Jaffe theory of

columnar recombination /50/ with various

simplifying assumptions . These assumptions are

inadequate, however, in accounting for recombi-

nation between free electrons and positive ions.

In general, for gases with no electron

attachment, and at low pressure, recombination

processes are not important .

3.2.5 Electron Drift Velocity and its relation to Pulse Rise Time

For electrons, the presence of an

electric field results in an increase in electron

temperature or agitation energy . This is

described by a commonly used expression, η , which

is simply the ratio of electron temperatures
(3/2)KT with and without the presence of an
electric field . In general η is a function of
E/p and is much larger for inert gases than for
·molecular gases . This may be explained by the
onset of inelastic collisions in molecular
gases at low agitation energies, preventing a
further increase in electron temperature .

Further to the increase in electron
temperature, the application of an electric
field results in the superposition of a drift
velocity, y, over the agitation velocity U
corresponding to the energy $1/2mU^2 = \eta (3/2)KT$.

A simple relationship between y and
U may be derived through a consideration of the
relationship : Velocity = Acceleration x Time,
for a particle with initial velocity zero, and
the assumption that an electron loses "memory"
following a collision with an atom . The acceler-
ation on an electron due to the presence of an
electron field E, is Ee/m . The average time
lapse between collisions is given by λ/Up ,
where λ is the electron mean free path per unit
gas pressure . Thus the average drift velocity
may be expressed as 1/2(Ee/m)(λ/Up) along the

line of force, or :

$$y = Ee^{\lambda}/2Ump \qquad \text{--------(3.6)}$$

It is apparent from equation 3.6 that for a given λ and E/p, the electron drift velocity is inversely proportional to the agitation velocity U .
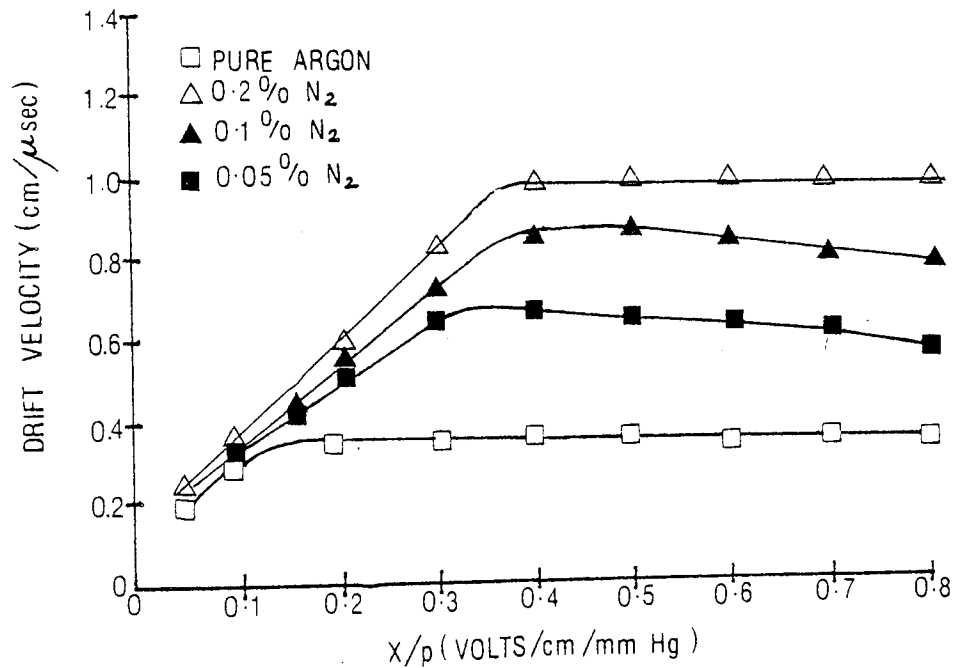

Fig. 3.6 : Electron Drift velocity in argon - nitrogen mixtures . From Bortner, Hurst and Stone /51/ .

Fig. 3.6 indicates the effect of the presence of increasing concentrations of nitrogen on electron drift velocity in argon . This is in agreement with the mechanism of reduction in

agitation energy due to inelastic collisions with nitrogen molecules .
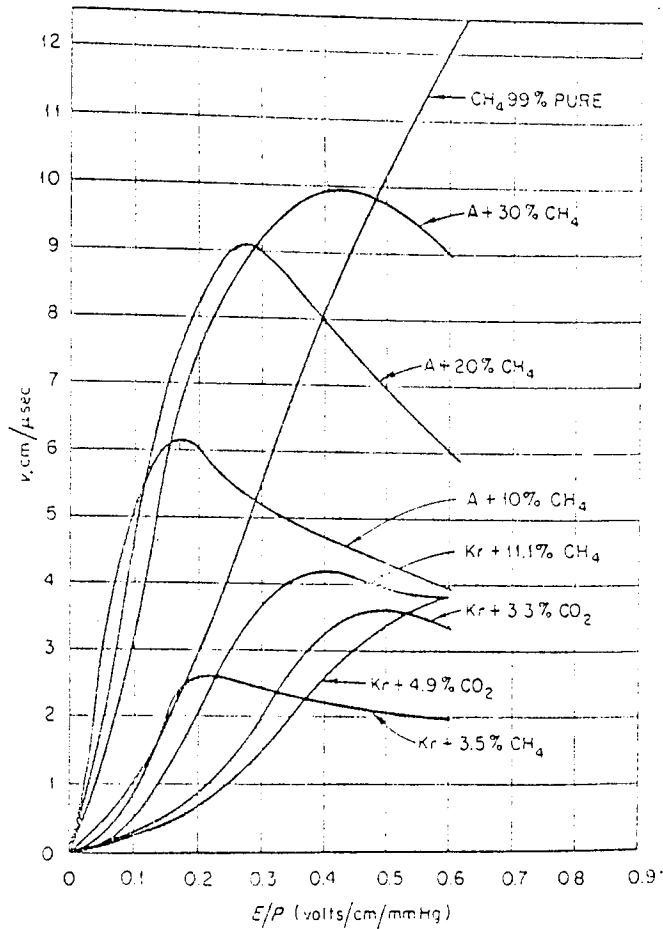

Fig. 3.7 : Electron drift velocity in various gases . From English and Hanna /58/ .

Extensive data on mixtures of argon - carbon dioxide, argon-methane and krypton-methane are presented by English and Hanna / 58 / .
Fig. 3.7 presents some of these results, of which methane provides the highest drift velocity and a correspondingly fast electron pulse rise time .

A general equation relating electron drift velocity to pulse rise time is easily derived on the assumption that an electron drifts along a line of electric force . Further, it should be noted that electron drift velocity is a function of E/p alone,

Expressing the drift velocity y as a function of E/p, where the field E is a function of position, the pulse rise time is obtained by direct integration of $y = -dr/dt=f(E/p)$ with respect to r, such that :

$$T = - \int_{a}^{r_0} 1/f(E/p)\,dr \qquad \text{----------(3.7)}$$

where r_0 is the initial position co-ordinate of the electron as measured along a line of force, and a, the co-ordinate of the intercept between the line of force and the collector electrode . From an analysis of the various geometrical configurations (parallel, cylindrical and spherical), a general equation expressing drift velocity as a function of r may be written as :

$$y = f(E/p) = \mu (E/p)^n = (E/p)^n \, r^{-m} \qquad \text{---------(3.8)}$$

The power n, is am empirical fit to

describe y as a function of E/p, and μ is defined to express y in cm/sec^{-1} . In the parallel plate configuration, m=0 and E=V/d, where d is the plate spacing . For the cylindrical case, m=1 and E=V/log(b/a), and m=2, E=Vab/(b-a) for the spherical case . Performing the integration in equation 3.7 provides a general equation for pulse rise time .

For the parallel plate configuration, with negligible edge effects, the electric field is a constant and it is simpler to express pulse rise time as d/y, where y is read off from the experimental points in fig. 3.7 . In reality, there will be a variation of electron pulse rise time in accordance with the variation in position of ionisation tracks . This effect will be discussed further in Chapter 4, when the contribution to detector performance by the ancillary electronics is discussed .

3.2.6 Summary

In this chapter, design considerations pertinent to the intrinsic performance of the detector have been discussed . Argon is shown to be ideal from the point of view of low W value . The possible introduction of electronegative

impurities however, requires the use of a mixture
incorporating argon and a polyatomic gas for the
reduction of sensitivity in detector response to
the presence of electronegative impurities . The
further requirement for fast pulse rise time
necessitates the use of mixtures providing high
drift velocities, of which methane best meets
this requirement . The use of methane in the mix-
ture, however, entails a choice of mixture
concentrations . Although increasing concentrations
of methane provide increasingly fast pulses, there
is a corresponding increase in the effective W
value, W_{ij} . Further, in a fast neutron field,
carbon and proton recoils are possible sources
of interference . With these considerations in
mind, an optimum mixture of 90% argon and 10%
methane was selected . Given a maximum neutron
energy of 6 Mev, corresponding carbon and proton
recoil energies were calculated to be 1.7 and
6.0 Mev . An analysis of the range and ionisa-
tion relationships for these particles indicated
negligible interference with fission counts .

The importance of appropriate choice
of chamber dimensions for improved discrimination
between alpha - particles and fission fragments
has been stressed . A further consideration for

the electrode area arises from the requirement for low detector capacitance C . The maximum output pulse V is given by V=Q/C, where Q is the total charge collected . The capacitance is given by $C=A\varepsilon_r\varepsilon_o/d$, where A is the electrode area and d the electrode spacing . Thus A/d should be minimised in order to maximise output pulse height per unit charge collected . The limits on A and d however are set by the alpha discrimination requirements . Bearing in mind the need for optimisation in design, a facility for varying the electrode spacing was incorporated .

In the following chapter, factors contributing to the performance of gas- filled fission detectors and the performance of the detector built are discussed .

CHAPTER 4
DETECTOR   PERFORMANCE

CHAPTER 4

4.1 Factors Contributing to Detector Performance

Prior to entering upon a discussion of the fission chamber performance, the factors contributing to overall performance will be discussed .

Resolution is a composite of two components, the extrinsic resolution σ_{ex} and the intrinsic resolution σ_{in} , such that :

$$FWHM/2.35 = (\sigma_{in}^2 + \sigma_{ex}^2)^{\frac{1}{2}} \quad \text{----------(4.1)}$$

σ_{ex} relates to the inherent noise contribution from the preamplifier-amplifier-P.H.A. combination . This contribution was measured through the experimental arrangement of fig.4.16 .

σ_{in} relates to the broadening of the pulse distribution within the detector and is unique to the detecting medium and the construction of the detector itself . Thus, a general form for detector resolution may be written as follows/53/:

$$FWHM = 2.35\sigma_{tot} = \frac{2.35}{\lambda}(\sigma_i^2 + \sigma_{tr}^2 + \sigma_t^2 + \sigma_p^2 + \sigma_A^2 + \sigma_{PHA}^2)^{\frac{1}{2}} \quad \text{--(4.2)}$$

where σ_i , σ_{tr} , σ_p and σ_t are components of σ_{in} , and σ_A and σ_{PHA} are components of σ_{ex} .

σ_i is the standard deviation in the number of ion-pairs formed for a given ionising particle .

σ_{tr} is the standard deviation due to rise time variations in the detector .

σ_t is the standard deviation due to self absorption in the source thickness .

σ_p is the standard deviation due to positive ion residual effect .

σ_A is the standard deviation due to the noise level in the detector and ancillary electronics.

σ_{PHA} is the standard deviation due to the pulse height analyser channel width and stability .

The factor σ_i is derived from a knowledge of the W value of the detecting medium i.e. the energy required to produce an ion-pair . For the argon-methane mixture used, the W value may be derived from equation 3.3 and is approximately 26 ev per ion-pair . The number of ion-pairs formed, J, is thus proportional to the ionising particle energy and subject to random fluctuations . For a truly Poisson distribution, the mean square deviation would be given by :

$$\overline{(J - J_o)}^2 = J_o \qquad \text{-------}(4.3)$$

where J_0 is the mean number of ion-pairs formed .
This relation is not vindicated experimentally .
Fano /53/ provides the relation :

$$\overline{(J - J_0)^2} = \overline{(n - \mathcal{E}/W)^2} \; J_0/\bar{n} = FJ_0 \quad \text{-------}(4.4)$$

to account for the standard deviation in the rate
of ion-pair formation being less than would be
expected from a purely Poisson distribution .
The term $\mathcal{E}$ refers to the energy loss in a primary
collision within the gas and n, the number of ion-
pairs produced in a primary collision . The Fano
factor, F, for a gas is reported to be between
0.3 to 0.5 /53/ . However, a much lower value of
0.09 was reported by Alkhazof et al /54/ using a
mixture of argon and acetylene .

In ungridded ionisation chambers, the
most significant contribution to detector
resolution is that due to σ_{tr} and σ_p. As mentioned
in chapter 3, electrons traverse the detecting
medium at much greater speeds than positive ions.
As electrons travel towards the anode, positive
ions drifting slowly towards the cathode create
a space charge and effectively reduce the electric
field . Consequently, E/P is reduced with a
corresponding change in electron rise time .

Further, the varying distances traversed by
electrons to the collector contributes to rise
time variation . The time for space charge
formation is also dependent upon track position.
The overall effect is a range of pulse rise
times for monoenergetic electrons .

In addition to pulse rise time
variation, pulse amplitude variations are observed.
This is illustrated in fig. 4.13, where f is the
distance of the point at which the ion-pair is
formed to the cathode, expressed as a fraction
of the electrode spacing .
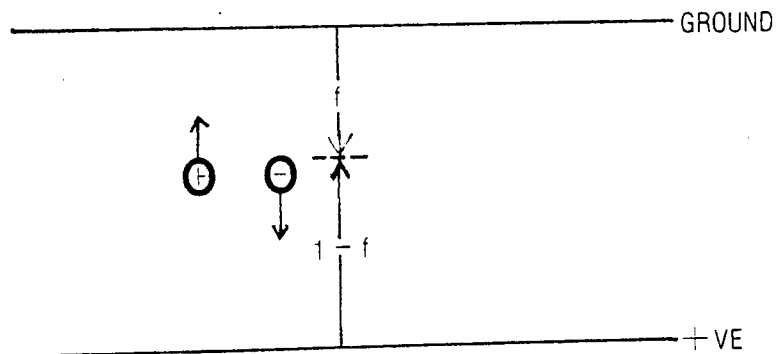
FIG. 4.13: Schematic representation of pulse amplitude
formation .

It may be shown through energy conservation that
the voltage induced at the anode by the electron
is $(1 - f)e/C$, whilst that of the ion is fe/C .
The voltage induced through total charge
collection is given by e/C . However, total

charge collection is not practical, as mentioned

in subsection 3.2.3 . The pulse shapes shown in

fig. 4.14 are for single ions .

$V_{max} = fe/c$

$V_{dec} = (1-f)e/c$

←—ion collection time - - - - - →

DECAY

VOLTAGE

TIME ————→

electron collection time

(a)

$V_{max} = ec/f$

VOLTAGE

TIME ————→

(b)
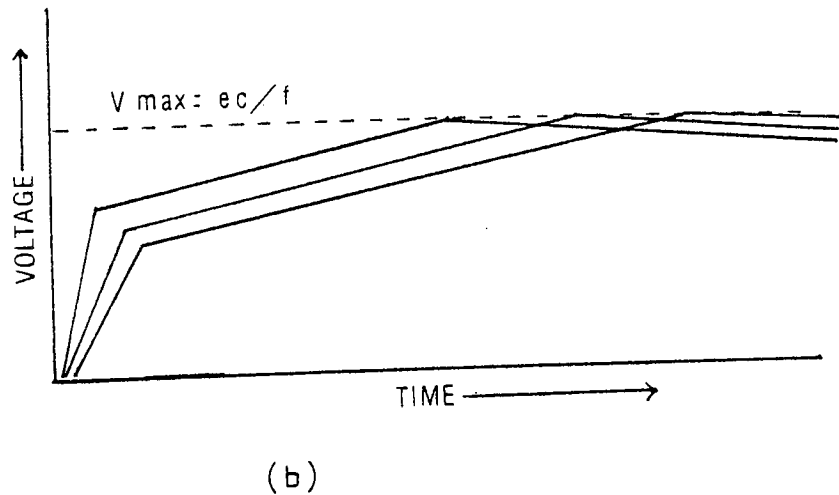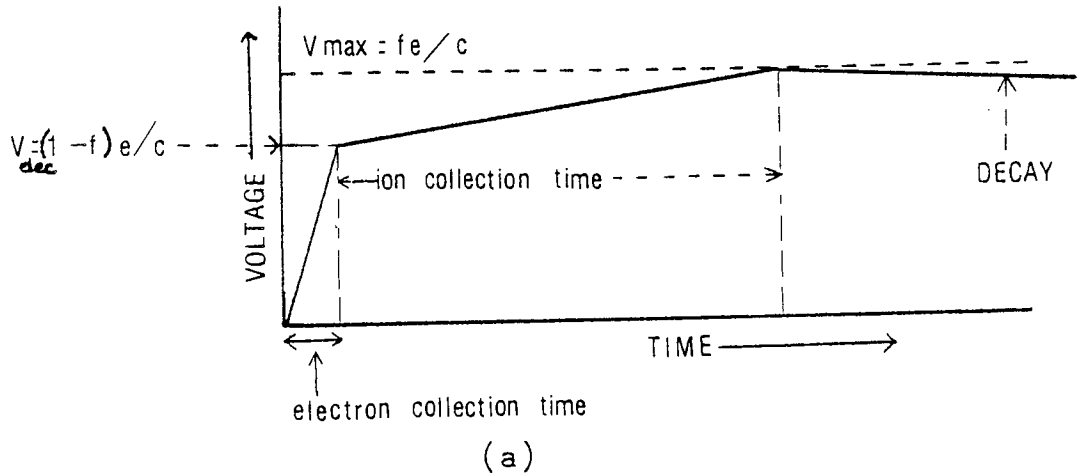
Fig. 4.14(a) Induced voltage from a single ion-pair.

(b) Induced voltages from single ion-pairs

having different initial locations

(rise time variations shown) .

For a nuclear particle creating a large number
of ions, the shape is more rounded (fig. 4.15).
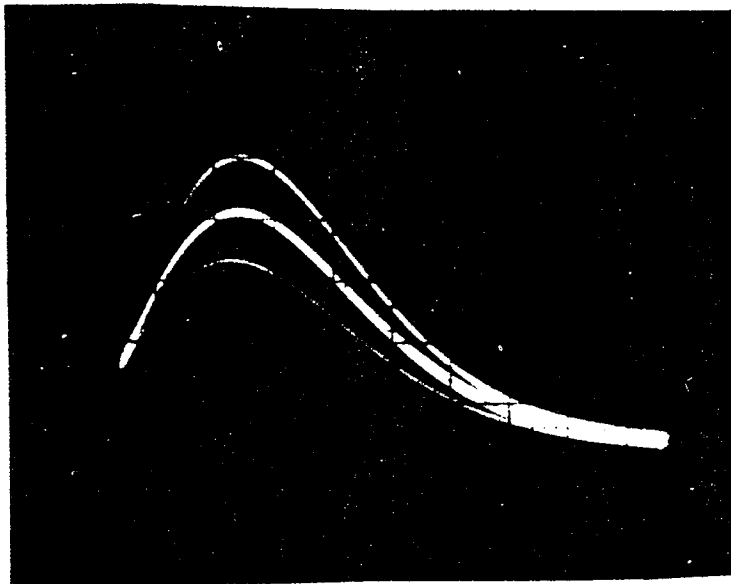
Fig. 4.15: Pulse shapes from the fission chamber.

The overall effect of an amplifier differentiation
time constant corresponding to electron collection
on pulse amplitude and rise time is a variation
in pulse amplitude. A solution to this problem
was put forward by Frisch /55/ through the use
of a grid, to provide screening against the space
charge .

The grid voltage is selected to
confine a major fraction of the electric field,

in the region between the grid and collector .
Thus, the induced signal on the anode is due to
electrons falling through the grid anode potential
difference alone, hence negating the broadening
effects mentioned above . A further advantage
of the gridded ionisation chamber is the shorter
collection time due to the grid-collector
proximity . Alkhazof reported a resolution of
0.5% using a gridded ionisation chamber with an
argon-acetylene mixture, whilst Mushtaq /56/
observed a resolution of 3.0% with a 90% argon
10% methane mixture . This is attributeable to
differences in the Fano factors; 0.09 and 0.3 to
0.5 respectively, and the grid dimensions used.

σ_t

The broadening introduced due to
particle energy losses in the uranium sample
thickness is characterised by a low energy tail,
and directly related to sample thickness .

σ_{ex}

The contribution of σ_{ex} (noise,
variation in amplification factor and pulse
height analyser channel width) to detector
resolution is, in general, small in comparison

to the contribution from $\sigma_{intrinsic}$, the exception being in the case of high resolution detectors .

During the course of this work, the contribution of σ_{ex} to the FWHM resolution was measured using the experimental arrangement shown in fig. 4.16 .
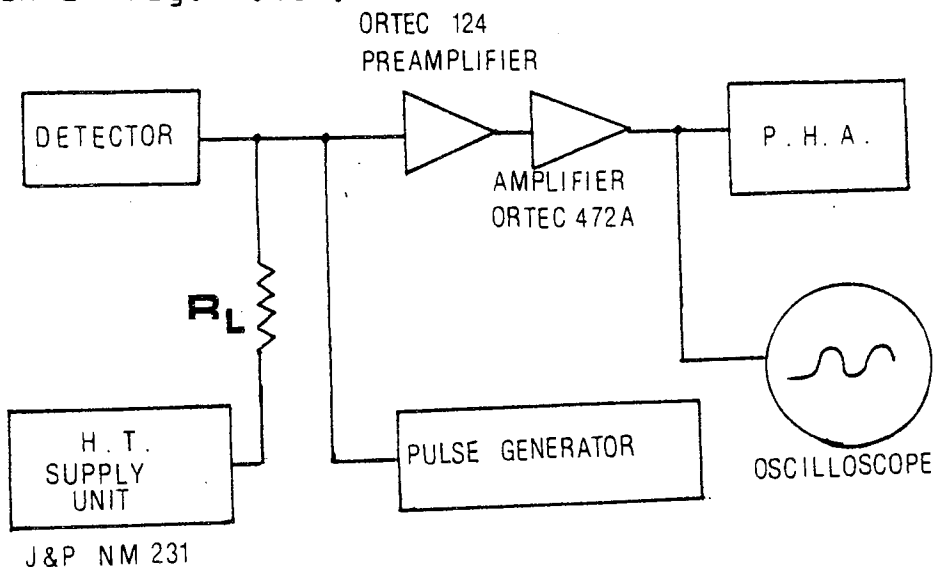

Fig. 4.16 : Experimental arrangement for the measurement of extrinsic resolution.

The pulser was set to generate approximately 500 pulses per second and the pulse rise and fall times set to 1 microsecond and 50 microseconds respectively . The fission chamber was connected to the preamplifier without the uranium foil in place and the bias switched on . This was done in order to stimulate the effect

of detector capacitance on the overall noise level . The FWHM resolution was found to be better than 0.2% .

4.2 Measured Detector Performance

Fig. 4.17 illustrates the fission counter designed for this work . The detector aluminium casing was made as thin as possible (0.125 mm thick) to minimise neutron scattering by the chamber, the limiting thickness being determined by rigidity requirements .

Characteristic ionisation curves for the detector were obtained using both an argon and a methane-argon mixture (gas composition 10% CH_4 , 90% Ar), at various source-electrode spacings and employing an alpha source . The argon-methane mixture generally gave more consistent results in addition to the larger pulse amplitude, as illustrated in figs. 4.18 and 4.19 . This is due to the reduced sensitivity to the presence of electronegative impurities in the methane-argon mixture .

Amplifier shaping constants $T_1 = T_2$ * were optimised experimentally at each electrode setting, the results of which are illustrated in fig. 4.20 .

*T_1 and T_2 are the amplifier differentiation and integration constants , respectively .
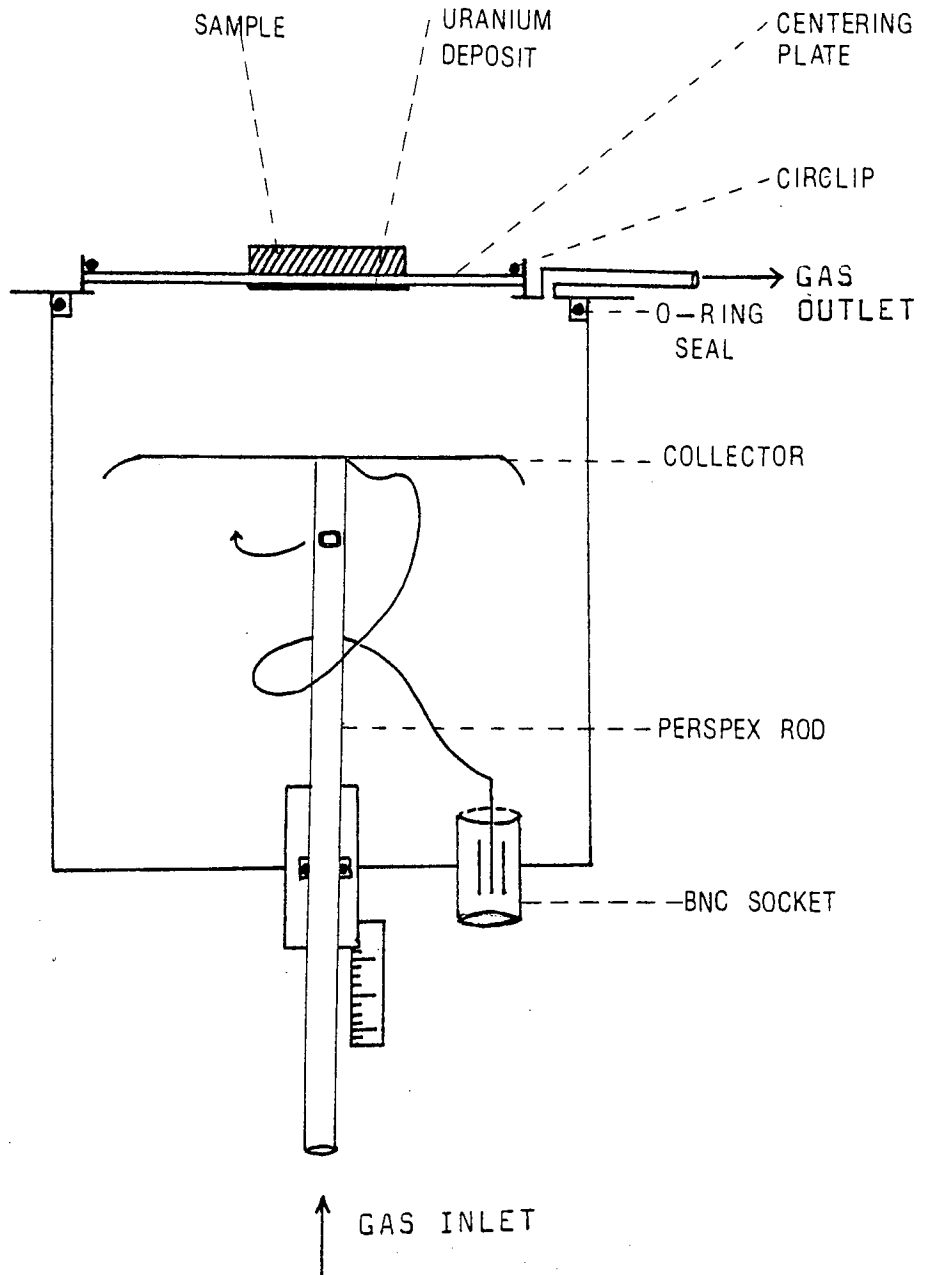
FIG.4.17a: SCHEMATIC DIAGRAM OF THE
FISSION COUNTER
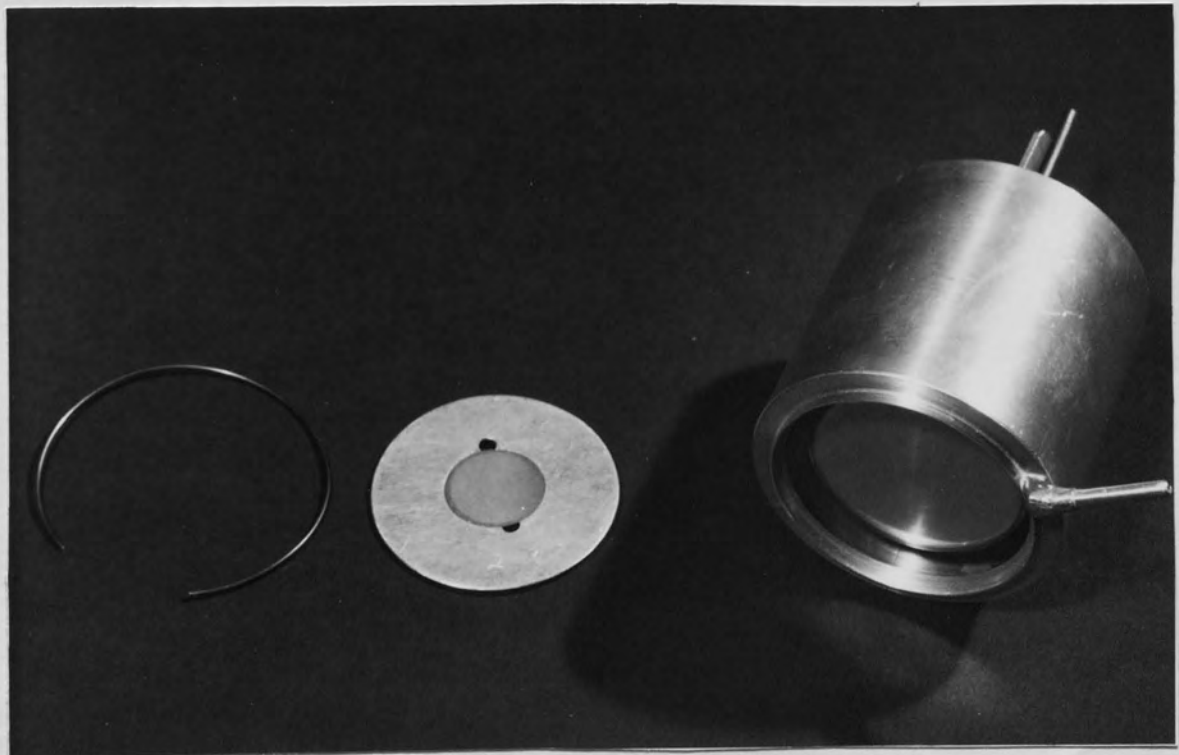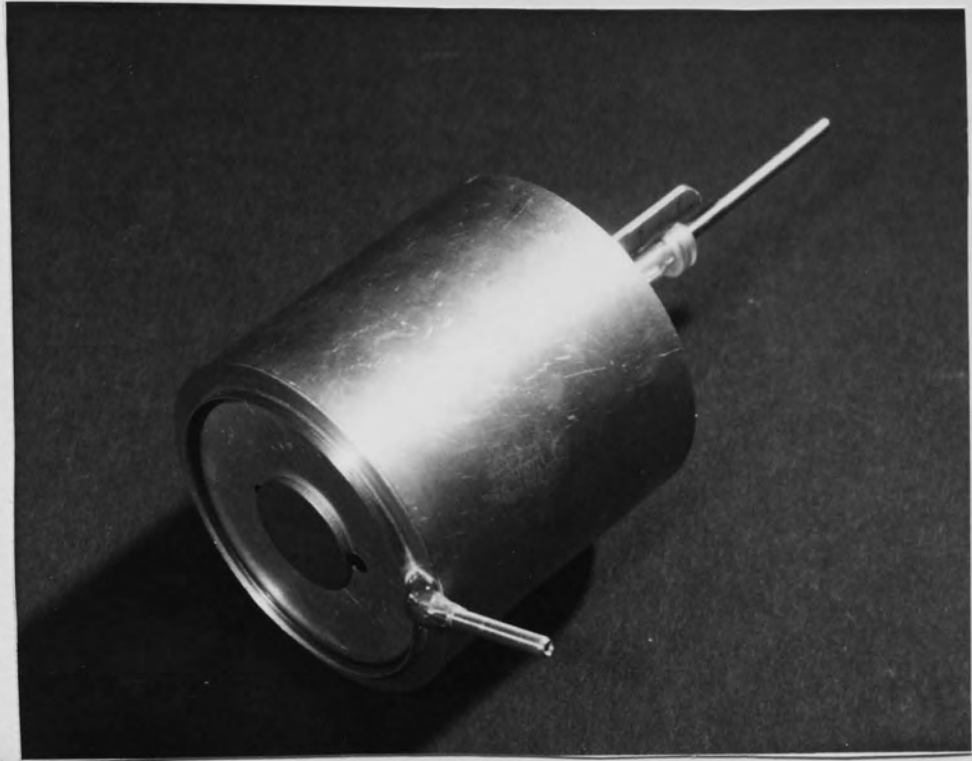
FIG . 4.17b: PHOTOGRAPH OF FISSION CHAMBER .
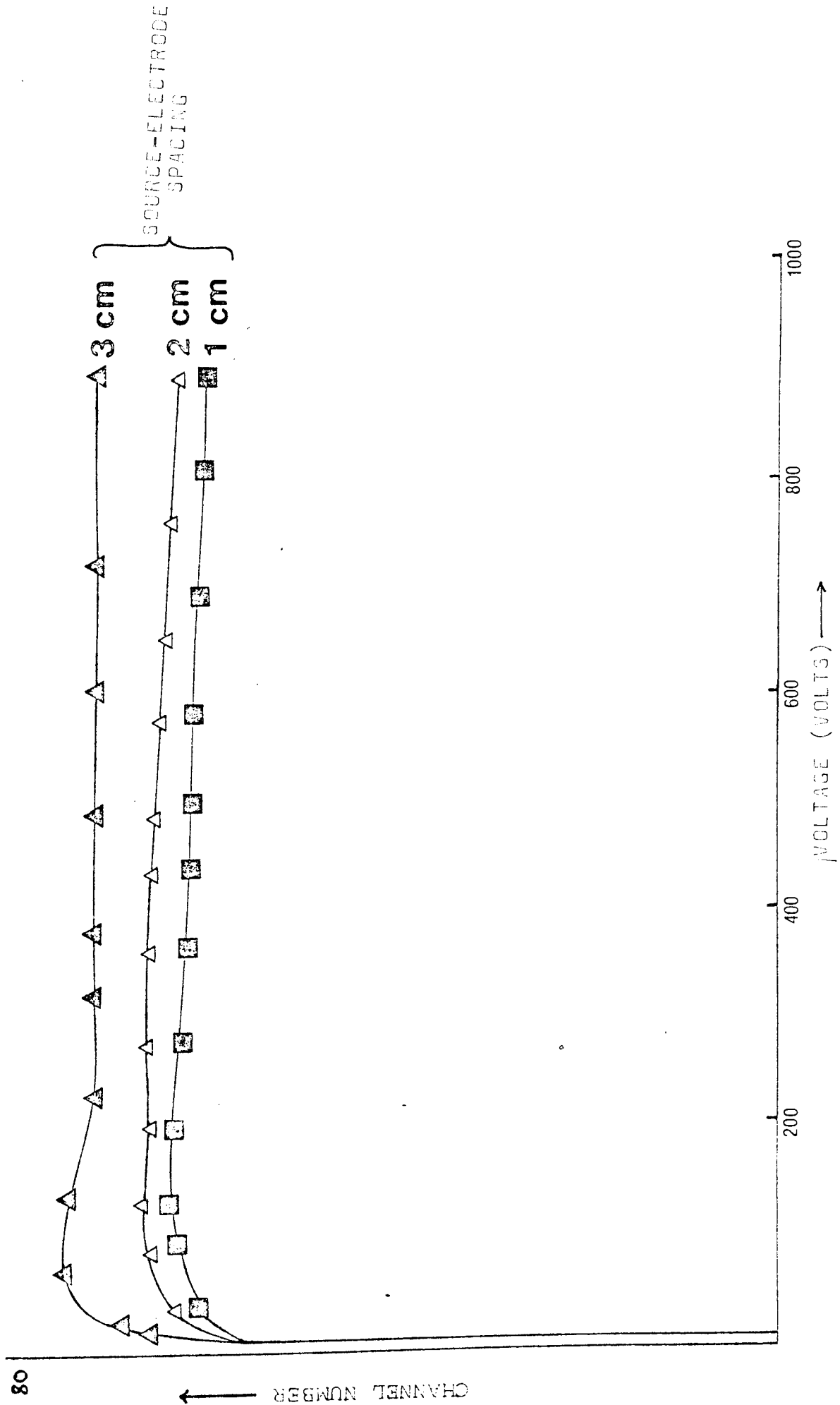
FIG. 4.18: CHARACTERISTIC IONISATION CURVES FOR THE FISSION CHAMBER USING PURE ARGON AS FILLING GAS
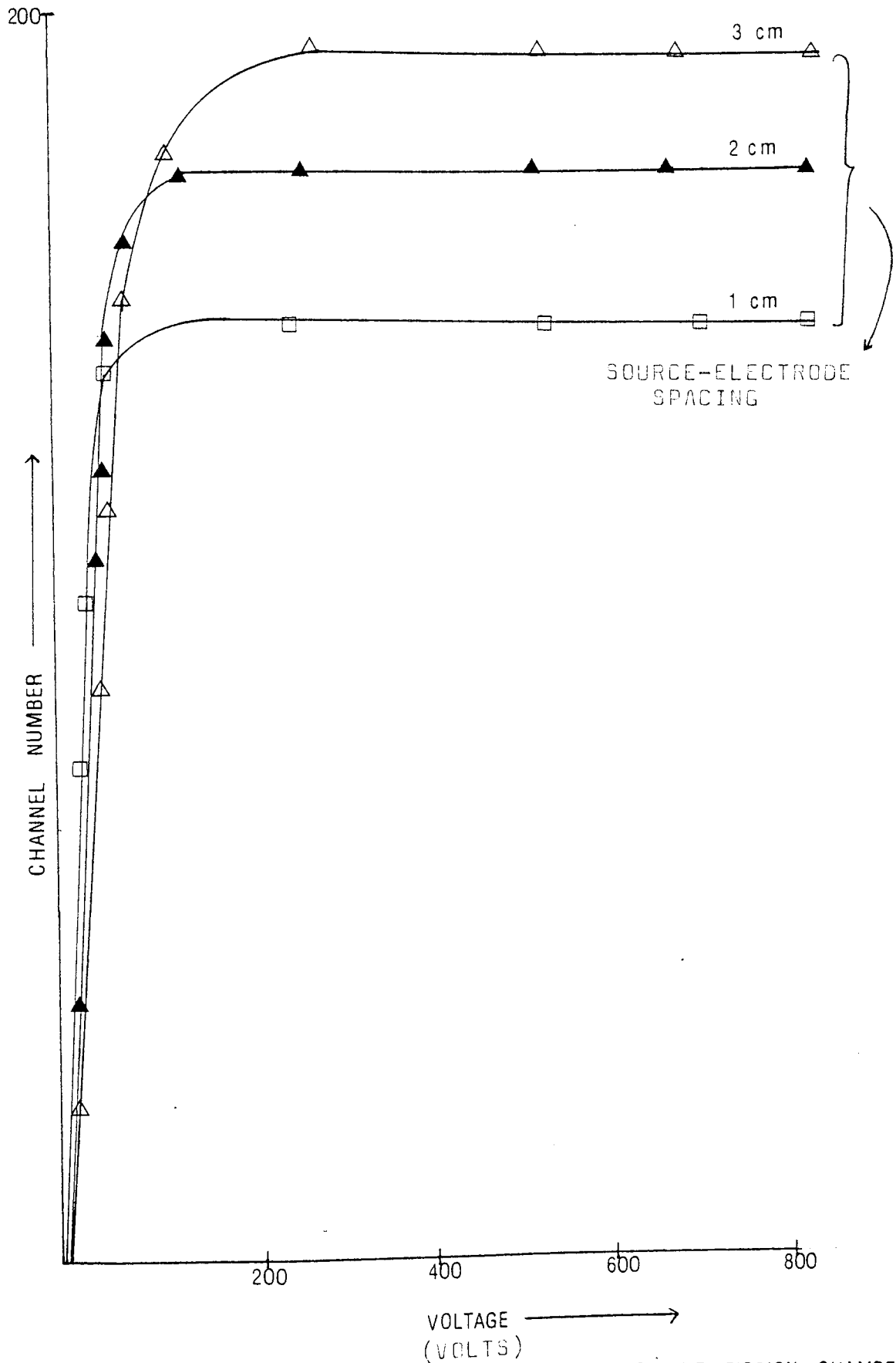
Fig. 4·19 CHARACTERISTIC IONISATION CURVES FOR THE FISSION CHAMBER
USING   90% argon — 10% methane
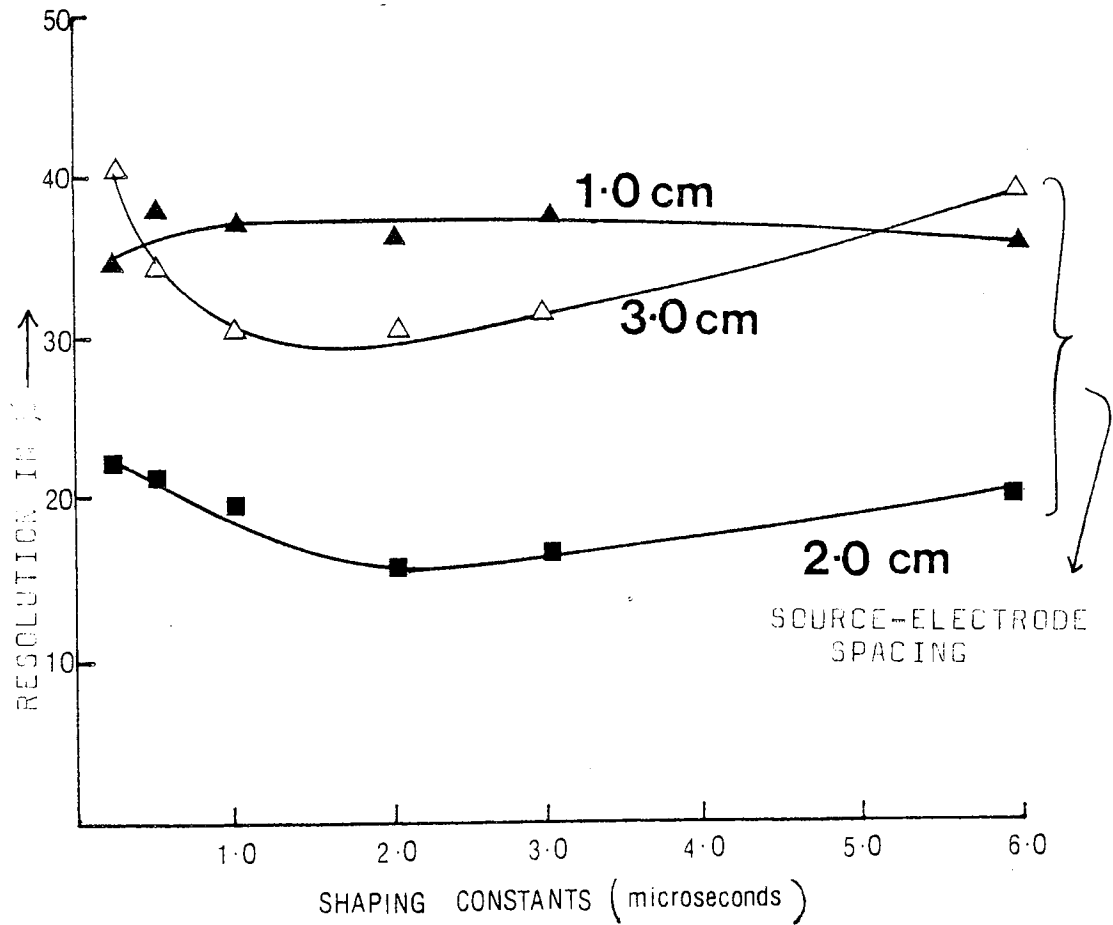
FIG. 4. 20 : VARIATION OF RESOLUTION WITH AMPLIFIER
SHAPING CONSTANTS . E.H.T. SETTINGS
WERE OPTIMISED FOR EACH ELECTRODE
SPACING USING INFORMATION FROM
FIGS. 4.19 AND 3.7

The effect of using amplifier constants less than the detector pulse rise time, T, due to electron collection, is to clip the pulse produced and, as discussed earlier, the overall effect is a worsening of the resolution . The use of longer shaping constants, on the other hand, results in increased probability for pulse pile-up . The detector pulse rise time as measured on an oscilloscope at the preamplifier output was found to be approximately 0.6 microseconds, confirming the results of fig. 4.20 .

4.2.1 Alpha Particle Spectra

Figs. 4.21 to 4.24 illustrate the spectra obtained for the monoenergetic alpha particles using electrode spacings of 1 cm, 2.0 cm, 3.0 cm and 3.5 cm . The spectral shapes were not the single peak expected from the alpha particle source . A study of the electrode geometries and alpha-particle ranges indicated that these effects were due to the source - electrode configuration (Fig. 4.25) .
The larger amplitude peak is that due to alpha-particles traversing past the collector electrode.
The smaller amplitude peak is attributed to alpha-particles with ionisation tracks
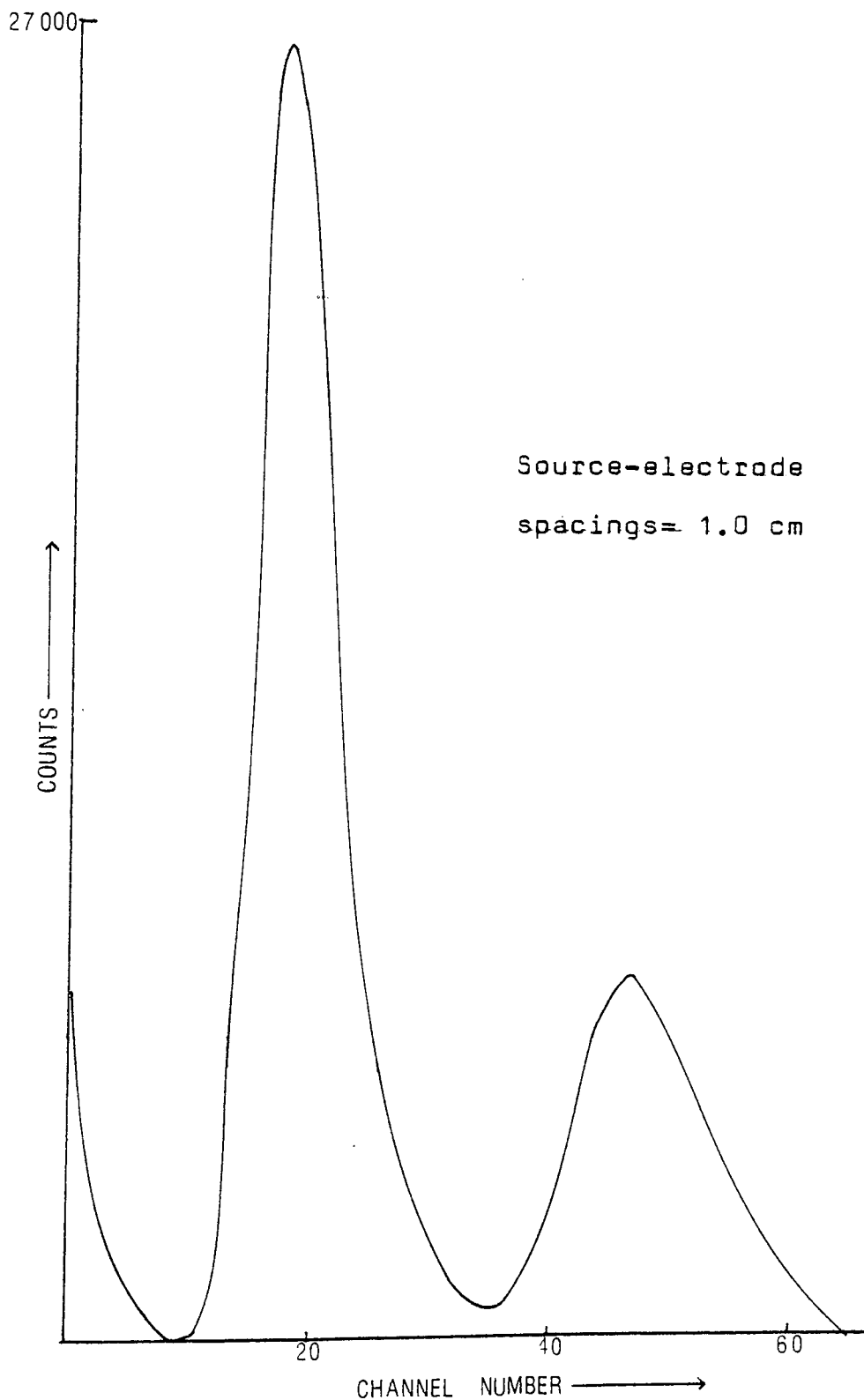
FIG. 4.21: ALPHA SPECTRUM FROM ^{241}Am (AMR 52).

DETECTOR FILLED WITH PURE ARGON

SOURCE-ELECTRODE SPACING = 2.0 cm
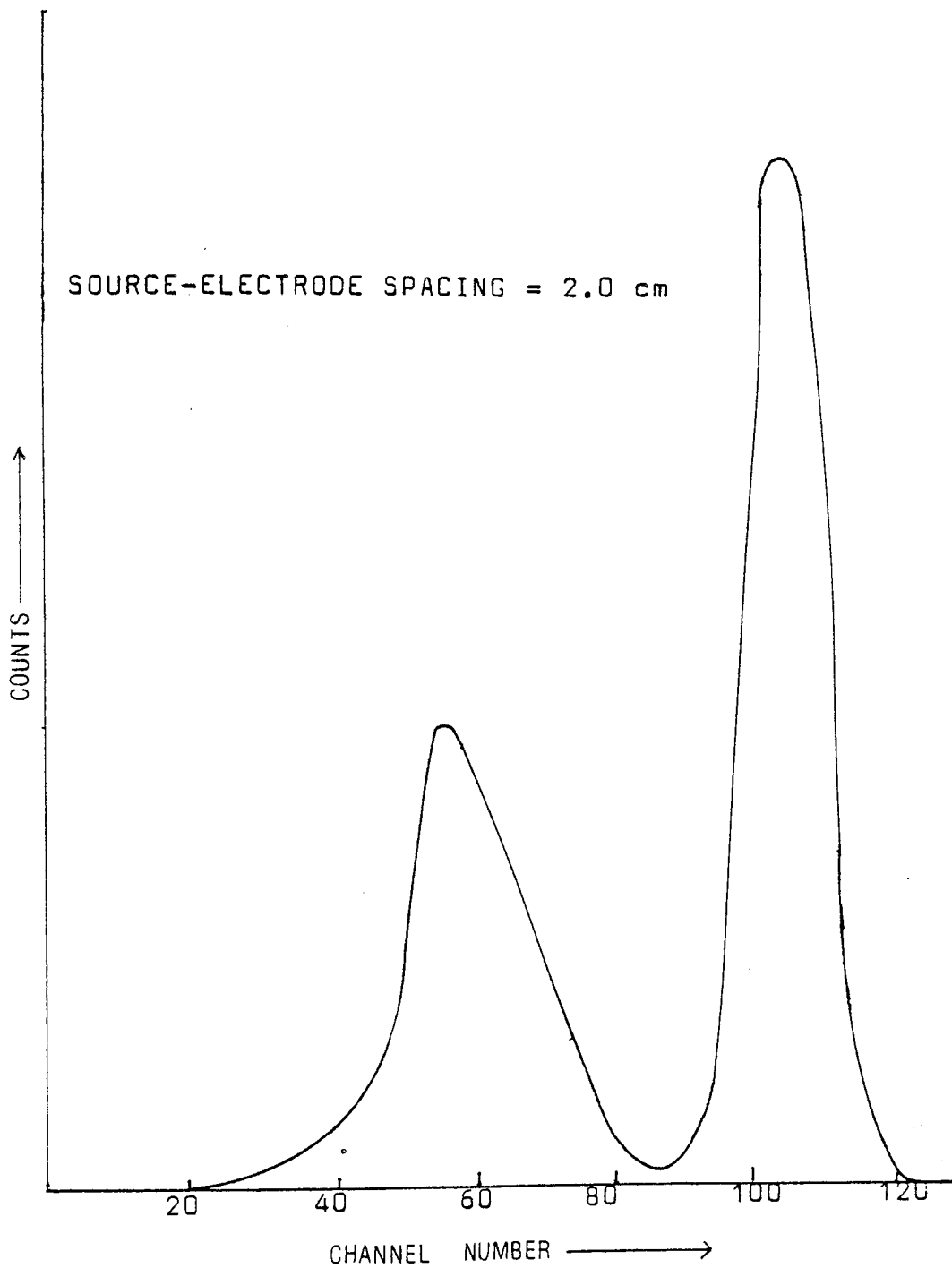
FIG. 4.22: ALPHA SPECTRA FROM ^{241}Am (AMR 52).
DETECTOR FILLED WITH PURE ARGON
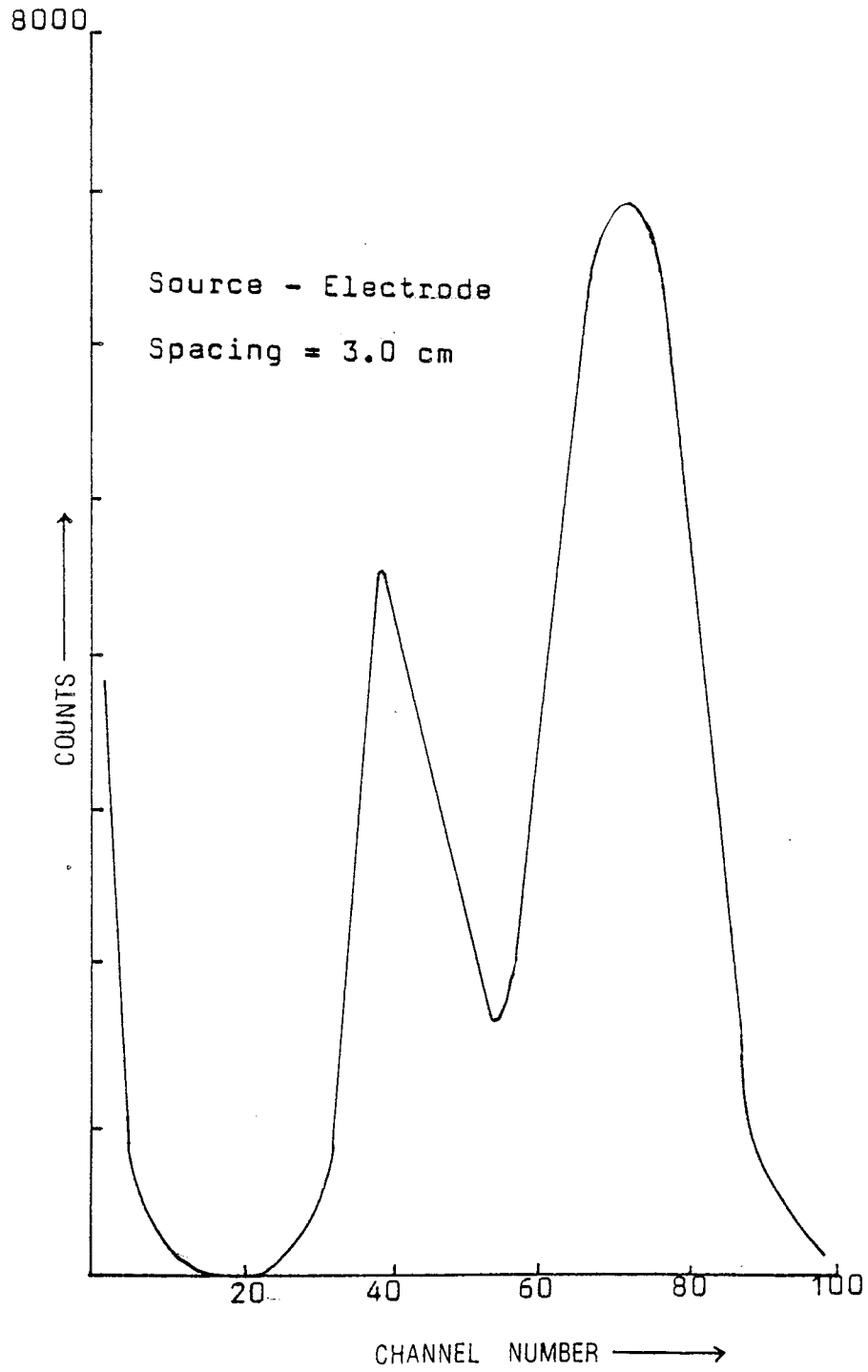
FIG. 4.23 : ALPHA SPECTRUM FROM ^{241}Am (AMR 52)
DETECTOR FILLED WITH ARGON
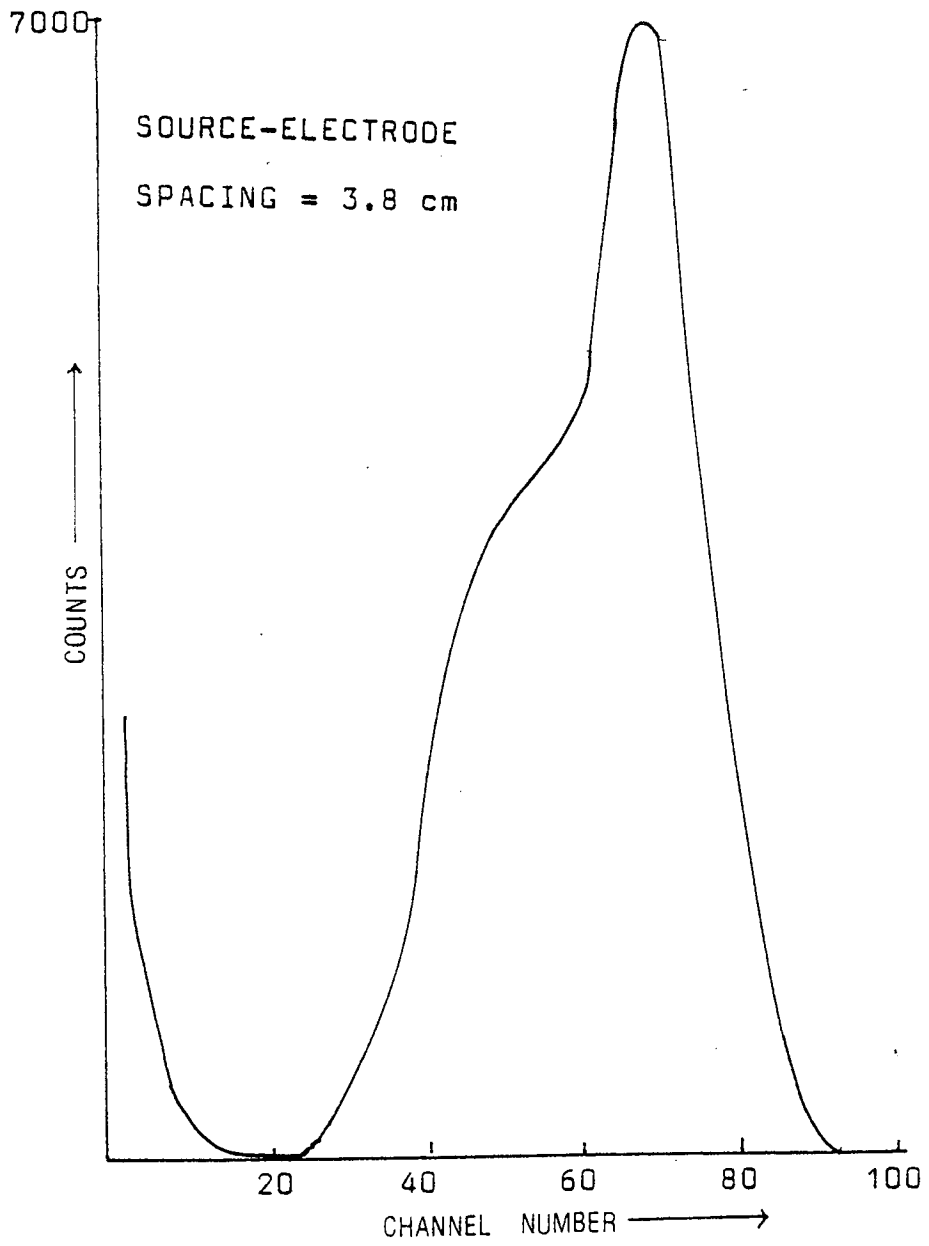
FIG. 4.24: ALPHA SPECTRUM FROM ^{241}Am (AMR 52)

intercepting the electrode and thus not depositing their full energy within the gas .
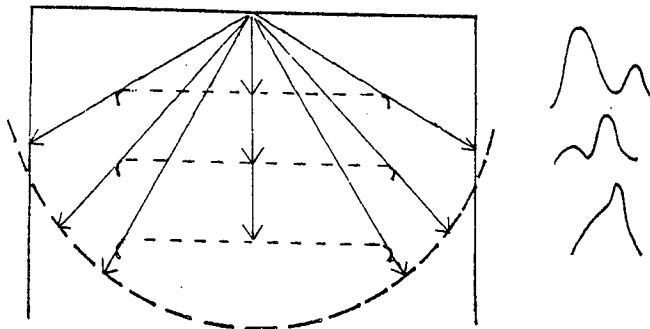
FIG. 4.25: EFFECT OF ELECTRODE GEOMETRY

ON ALPHA PARTICLE RANGES

IN THE CHAMBER .

The change in peak area ratios with electrode spacings in figs. 4.21 to 4.24 are in accordance with this explanation .

The spectrum illustrated in fig. 4.24 was obtained at a source electrode spacing of 3.8 cm, which is greater than the 3.2 cm range of the 4.8 Mev alpha particle from uranium-234 . Although the alpha particle tracks no longer intercept the electrode, a fraction of the alpha particles deposit part of their energy in the chamber walls . In order to overcome these detector geometry effects, it is necessary either to increase the fission chamber dimensions or to increase the gas pressure .

Mushtaq /56/, using a chamber of similar electrode configuration, observed similar effects . By increasing the gas pressure in the chamber the spectral distortion was eliminated .

At an electrode spacing of 2 cm and a pressure of one atmosphere, these spectral effects are not observed with fission fragments due to the mean range of the fission fragments being 2.0 and 2.5 cm respectively, and the specific ionisation being greatest at the start of the ionisation track . With smaller electrode spacings, distortion of the fission spectra is apparent . Nevertheless, in fission counting, the primary consideration is discrimination against alpha particles and the accurate measurement of fission counts . Although the spectral distortion may not affect the number of fission counts observed, it is an integral part of the considerations required to optimise alpha discrimination . This is particularly true in relation to the choice of chamber and electrode dimensions .

4.2.2 Alpha particle-fission fragment discrimination

The relationship between range and ionisation density and its relevance to

discrimination has been discussed in 3.2.1 . In
parallel plate geometry, decreasing the electrode
spacing reduces the ratio of the maximum energy
deposited by the alpha particle to that of maximum
energy deposited by the fission fragments . Alpha
particles emitted from the foil surface (assuming
no energy loss through absorption in the deposit)
at small grazing angles to the surface, deposit
an amount of energy independent of the electrode
spacing . Further, pulses due to ions emitted
close to the source, generate pulses which are
larger than those emitted close to the collector.
Thus, the ratio of minimum fragment energy to
maximum alpha particle energy decreases with
distance, hence reducing alpha discrimination .
Therefore, optimum source-detector distance is
required .

Fission spectra were obtained using
a moderated americium-beryllium neutron source
at various electrode spacings . A source-electrode
spacing of 2.0 cm was subsequently found to
provide the best discrimination .-This is not
unexpected since this configuration provides
the most symmetric sensitive volume dimensions
for the detector . A further decrease in chamber
dimensions, whilst maintaining symmetry, would

improve alpha discrimination . However , the chamber
dimensions are limited by the uranium deposit and
backing foil diameters of 2.0 cm and 5.0 cm respec-
tively .

4.2.3 Alpha Particle Pulse Pile-up Prevention

The presence of several alpha particles
within the resolving time of the detector system
can result in the superposition of pulses, generating
a single pulse of amplitude comparable to the
smaller fission fragment pulses .

Given the detector pulse rise time T of
0.6 microseconds , and an amplifier shaping constant
of one microsecond , the resolving time of the
system may be determined from the graph provided by
Gillespie / 57 / (Fig . 4.26) . This provides a
resolving time , τ , of approximately 2.0 micro-
seconds .

Following Gillespie , the pile-up count
rate C_α can be determined by the relationship :

$$C_\alpha = \frac{N_0 \exp(-N_0 \tau)}{(1+(\frac{1}{3})N_0 \tau)} \sum_{n=r}^{\infty} \left[\frac{(N_0 \tau)^{n+N_0 R - 1}}{(n + N_0 \tau - 1)!} \right] \qquad (4.5)$$

Where :

N_0 = Alpha counts per second

   = Resolving time in seconds

R = Ratio of the minimum fission to the average
   alpha particle energy

n = Integer from R to infinity
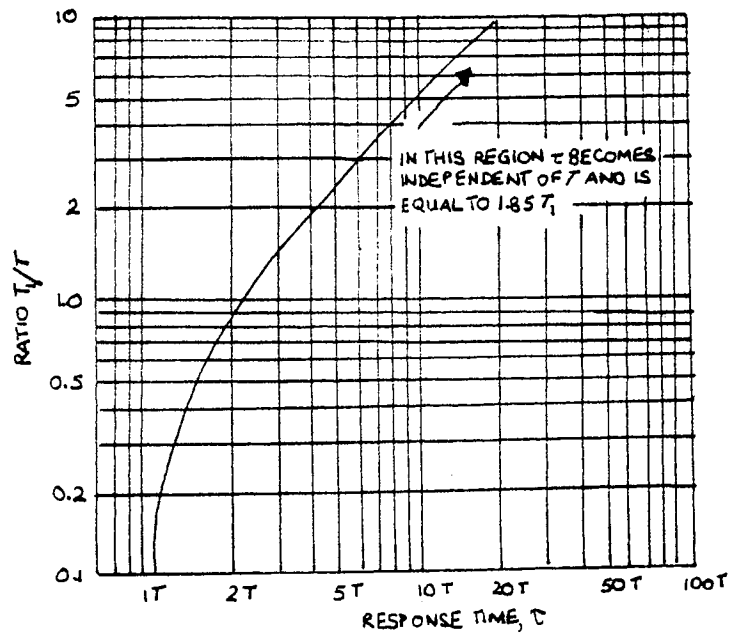
FIG. 4.26: Resolving time , τ , as a function of
          detector pulse rise time , T, and equal
          amplifier time constants , $T_1 = T_2$ (Gi53).

Setting N_o = 500 cs^{-1} , τ = 2.0 microseconds and
R = 15 Mev/3 Mev = 5 , a value of approximately
1 x 10^{-13} counts s^{-1} is obtained for C_α . This
is negligible . Equation 4.5 represents the number
of coincident alpha pulses occuring within the
resolving time τ , giving a pulse approximately
R times that of a single alpha particle pulse .
In the measurement of fission activity , fission
counts corresponding to fragment energies greater
than 15 Mev only were counted (see fig . 4.27) .
If fission counts corresponding to energies
greater than 6.0 Mev only were counted (R = 2) ,
then C_α would be approximately 0.5 counts s^{-1} ,
which compares unfavourably with the fission count
rate . The fission spectrum shown (fig . 4.27)
illustrates that fission counts of energy less than
15 Mev are significantly less than 1% of the total
counts , for which a correction factor can be
applied as described in section 4.3.1 .

4.3 Corrections applied to the Fission Counts

4.3.1 Absorption Corrections

Measurements on fission fragment ranges
are discussed by Hyde /61/ and Frank /62/ and
referenced by White /63/ , where the mean fragment
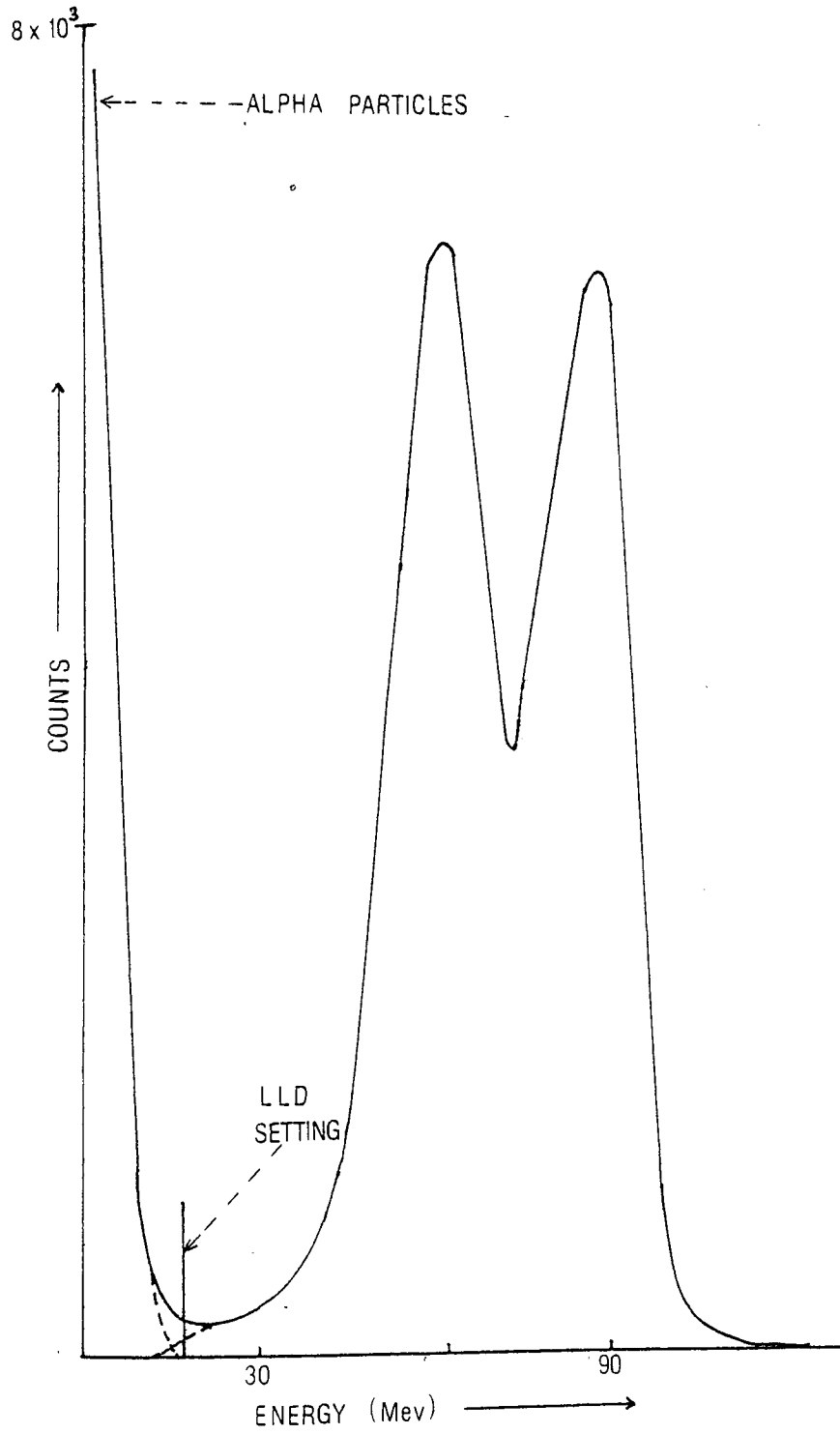
FIG. 4.27: FISSION SPECTRUM

range is quoted as 7.5 ± 0.5 mg cm^{-2} . The ranges
of the heavy and light fragments are 0.9 and 1.1
times the mean range , respectively . For a deposit
of finite thickness , t , fragments arising from
the deposit lose energy in the deposit . Further ,
fragments emitted at grazing angles to the surface
are totally absorbed . Except for very thick deposits,
absorption corrections run from 0.1% to 10% . The
fraction absorbed , F , is represented by the
relation $F = t/2R$, where t is the deposit thickness,
and R the mean fragment range (see white / 63 /).
This relation does not account for fission fragments
emerging from the deposit with insufficient energies
to appear above the amplifier or P.H.A. lower level
discriminator setting . Thus the relation proposed
by Rossi et al /64/ may be used , where :

$$F = t/2 \ (R - R_o) \hspace{3cm} (4.5)$$

and R_o is the range of fission fragments in the deposit
having an energy equal to the energy equivalent of
the discriminator setting .

The existence of foil non-uniformity is,
to an extent , unavoidable . The effect is to
increase the absorption losses . Corrections for

non-uniformity may be incorporated into the absorp-
tion correction through the relation :

$$F = (t^2 + \sigma^2) / 2tR \qquad\qquad (4.6)$$

where σ is the standard deviation on the variation
of the thickness . R may be replaced by R - R_o to
account for losses to the lower level discriminator
setting . For this work , measurement of the foil
non-uniformity σ/t was made by Akhtar /64/ and
found to be 0.32 . The method of measurement is
described in 5.12 . White has demonstrated that ,
for uniform foils , an additional non-uniformity
correction factor dependent upon the method of
uranium deposition has to be applied . These correc-
tions have been determined experimentally by White,
through the irradiation of foils carrying deposits
of varying thicknesses , relative to a thin foil
back to back in a double ionisation chamber . For
deposits formed through vacuum evaporation or
electrospraying , the correction corresponds to a
non-uniformity of σ/t = 0.4 . The overall non -
uniformity may be determined by summing the two
contributions quadratically to give a value of
σ/t = 0.5 .

4.3.2 Backscattering Correction

Measurements on backscattering of fission fragments have been performed by Englkemier and Walton /58/ , who provide values of 4.6% and 2.8% average backscattering from platinum at fragment biases of 15 Mev and 8 Mev respectively . However, for thin foils , the emission of two fragments,with the backscattering of one from the deposit backing into the counting volume , results in the super-position of the two pulses . Hence , only a single count is registered and , in contrast to the backscattering of alpha particles , there is no correction for backscattering of fission fragments .

4.3.3 Momentum Correction

The effect of a neutron of energy E_n imparting its momentum to the compound nucleus , hence driving the fission fragments further into , or out of the deposit , has been calculated by Lamphere /65/ . Given that the range of the fragment is much larger than the deposit thickness , the momentum correction is given by :

$$F_m = \pm\ 0.0026\sqrt{E_n} \qquad\qquad (4.7)$$

F_m is positive for a deposit facing away from the neutron source , and negative for deposits facing the neutron source . Thus the correction factor may be expressed as $(1 + F_m)$.

This correction does not take into account the effect of anisotropy of the fission fragment angular distribution . Where anisotropy is not insignificant , F_m is given by /66/ :

$$F_m = \frac{t}{2R} (1 - 2QR/t)^2 (\frac{3}{2 + A}) \qquad (4.8)$$

where Q is the ratio of the neutron momentum to the mean fragment momentum , and A is the ratio of the fragment flux at 0° to the neutron direction , to that at 90° . This expression does not apply when at least one fragment always escapes from the foil, i.e. when $2QR/t = 1$, in which case $F_m = 0$.

CHAPTER 5
ALPHA ASSAY

CHAPTER 5

Alpha Assay of the Uranium Deposit

Accurate measurements of the masses of thin uranium deposits (< 1.0 mg cm^{-2}) on thick backings may be made through both destructive and non-destructive methods . Destructive methods may be made using techniques such as spectrophotometry or coulometry , and provide accuracies of better than 0.1% /67,68/ . Destructive methods , however, would not serve the requirements of this work .

Foils carrying fissile deposits of thicknesses 0.1 mg cm^{-2} to 1.0 mg cm^{-2} can be assayed non-destructively by alpha or fission counting in 2π-geometry to an accuracy of 0.2% to 1.0% , depending on deposit thickness /63/ . In low geometry, accuracies of 0.1% are reported , but similar accuracies are possible in 2π-geometry through relative measurements with a reproducibility of 0.01% /72/ .

In the purchase of foils , the choice of ^{235}U enrichment is of importance . It is suggested that high enrichments may not always be desirable , particularly in low geometry assay .

Should the ^{234}U content be reduced significantly as a result of high ^{235}U enrichments , the alpha counting accuracies would be considerably reduced due to the lower specific activities

encountered . For this work , a 5.0 cm diameter by
0.15 mm thick platinum foil , carrying a 2.0 cm
diameter by 0.1 mg cm^{-2} thick ^{235}U deposit (in the
form of U_3O_8) was purchased from A.E.R.E., Harwell.
The ^{234}U content of the deposit is 1.179% , providing
97.1% of the alpha-particle activity .

A similar ^{238}U foil , having a deposit
of thickness 0.2 mg cm^{-2} was later purchased and
used in a calibration experiment to determine the
thermal neutron contribution to the flux measurement.

The isotopic compositions of the two foils
are tabulated in table 5.1 .

Table 5.1 : Isotopic compositions of the ^{235}U
and ^{238}U foils .

^{235}U foil content	^{238}U foil content
^{235}U ———— 93.137%	^{238}U ———— 99.995%
^{234}U ———— 1.179%	^{235}U ———— 0.005%
^{236}U ———— 0.25%	
^{238}U ———— 5.435%	

The non-destructive assay of these foils
by fission counting was discounted , owing to the
non-availability of a calibrated neutron flux .
Further , even if a calibrated neutron source had
been available , the accuracy of the flux calibration

is probably no better than 1% . Fission counting
is thus limited to relative measurements where an
accurately assayed foil is available . Hence , the
foil was assayed using both 2π and low-geometry
alpha counting .

5.1 Alpha Assay in 2π-Geometry

The main advantage of 2π counting in
relation to low-geometry counting is the much larger
detection efficiency , allowing measurements on thin
layers of low activities . The 2π -assays in this
experiment were carried out using the parallel plate
ionisation chamber described earlier (see fig.4.17).
As will be apparent from the proceeding discussion ,
under certain circumstances , measurements made in
low-geometry provide greater precision . Nevertheless,
2π -measurements provide a check on the low-geometry
measurements . Further , a knowledge of the 2π
alpha particle activity corresponding to an accurately
known mass of uranium (from low-geometry measurements)
provides a means for a quick check on the possible
loss of fissile material .

Uncertainties in the 2π -geometry counting
stem from both backscattering in the deposit backing
and absorption of the alpha particles in the deposit.
The effect of self-absorption is to decrease the

observed counts , whilst backscattering increases
the counts observed . The principal contribution to
lost counts from absorption relates to the total
energy loss for alpha particles emitted at small
grazing angles to the foil surface . Alpha particles
emitted at less acute angles to the surface lose
only part of their energy and contribute to the low
energy tail observed in alpha particle spectra .
Fig. 5.1 illustrates this effect , as observed by
White /63/ using a gridded ionisation chamber .

The thinnest foil shows a low energy tail
of approximately 1% of the total counts and is
mainly due to backscattering . The spectrum from
the thickest foil is virtually all tail .

5.1.1. Experimental Method

The 2π alpha assay in this work was
initiated in May 1978 . Some non-uniformity in the
uranium deposit was evident from the colour fringes
of the deposit . In addition , there were signs of
surface contamination . Hence , the deposit activity
was accurately monitored and then cleaned in "decon
90" (decontamination fluid) solution . A second
assay produced no significant change in the alpha
count rate .

FIG 5.1 ALPHA SPECTRA FROM URANIUM DEPOSITS OF
DIFFERENT THICKNESSES (WHITE op. cit.)

The experimental set-up for these activity measurements is illustrated in fig. 5.2 . The scalars and pulse height analysers were connected in parallel and the dead time corrected results were analysed and checked for consistency . The lower-level discriminator of the single channel analysers were selected to discard noise and low energy alpha particle pulses . Selection of discriminator setting were made using a pulse generator .
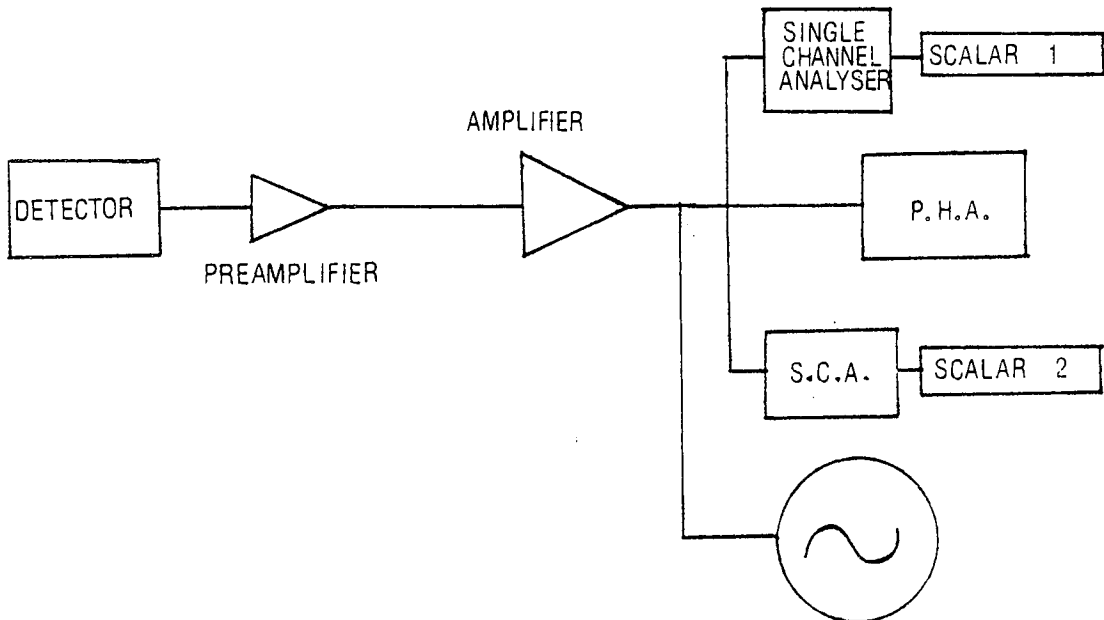

FIG. 5.2 SCHEMATIC DIAGRAM OF THE EXPERIMENTAL SET-UP USED IN THE ALPHA ASSAY

The rise and fall times of pulses from the pulse generator were set to simulate the pulse shapes from the detector and the pulse amplitudes then varied so as to correspond to the lowest channel of interest in the spectrum (see fig. 5.3) .
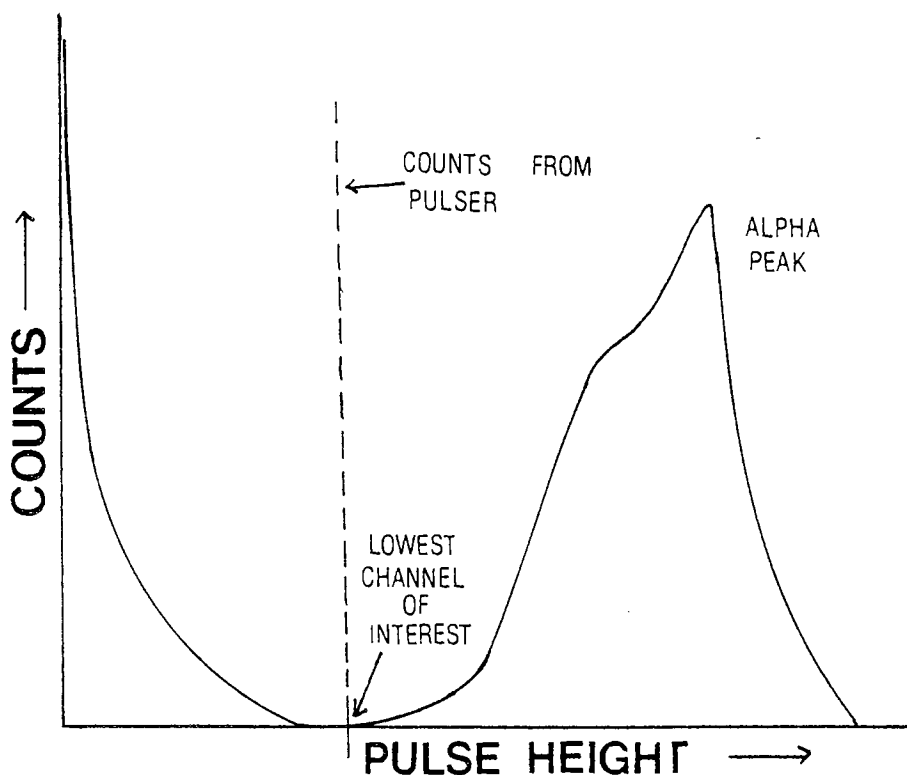
FIG. 5.3 : Setting the Single Channel Analyser
LLD to correspond to the lowest
channel of interest .

The lower-level discriminators were set at this

level . For this work , a lower-level discriminator

setting corresponding to 0.8 Mev alpha particle was

selected .

Alpha particle counts were recorded only

after optimum settings in the equipment had been

attained and the electronics checked for drift .

Optimum E.H.T. settings at any given electrode

spacing can be obtained from the data in figs . 4.19

and 4.26 , the latter providing data for minimum rise

time . Although no observable differences in count

rates with electrode spacing were apparent , an electrode spacing of 3.5 cm was used . This provides a single alpha particle peak and , hence , facilitates the energy calibrations required for absorption corrections .

In the assay , several sets of data involving 30 successive measurements were obtained , whilst keeping experimental conditions constant . An accumulation period of 100 seconds for a single measurement was found convenient , given an alpha particle activity of approximately 500 cs^{-1} . Data from a typical set of measurements for the ^{235}U foil is presented in Table 5.2 , and for the ^{238}U foil in Table 5.3 .

During these measurements , the background count was , on occasion , observed to vary by as much as 300% during the course of a day , but remaining constant for sufficiently long periods . This was due to noise pick-up from machines operating in the vicinity of the laboratory . Hence , several background readings were interspersed between activity measurements in the same set , to provide a check on possible drastic changes in the mean background level . In the ^{235}U assay , the mean background level is only 0.004% of the total counts and the statistical uncertainty in the activity

Table 5.2 : Alpha particle counts for the ^{235}U

foil in counts per second (2π-geometry)

507 $\pm$ 2	506 $\pm$ 2
504	506
504	504
501	504
508	510
504	506
504	505
502	504
507	499
506	502
505	506
501	503
501	503
503	505
504	504

Mean = 504 $\pm$ 0.4 cs^{-1}

Mean background = 0.02 cs^{-1} $\pm$ 0.002

Table 5.3 : Alpha particle counts for the ^{238}U

foil in counts per second (2π -geometry)

4.2 $\pm$ 0.2	4.1 $\pm$ 0.2
4.2	4.0
4.6	4.2
4.2	4.8
4.5	4.3
4.3	4.2
4.4	4.3
4.5	4.3
4.1	3.9
3.9	4.4
4.5	4.4
4.2	4.2
4.4	4.8
4.1	4.2
4.4	4.2

Mean = 4.3 $\pm$ 0.01 cs^{-1}

Mean background = 0.02 cs^{-1} $\pm$ 0.002

measurements is 0.1% . Hence, the effect of a 300%

change in the mean background level is negligible .

In the ^{238}U assay , however, greater care is required

in performing the measurements .

Each data set was tested for conformity

with the Poisson distribution . This provides an

indication of whether the observed fluctuations in

a set of measurements is solely due to statistics .

Appreciable deviations from the Poisson distribution

would suggest some equipment malfunction resulting

in the injection of spurious counts . Three such

sets were discarded as a result - a fault was later

traced to a NIM BIN . Through the course of the

faulty measurements, intermittent noise pick-up was

simultaneously observed on the oscilloscope .

The method used for determining the good-

ness of fit between the observed frequency distribution

of the measured data and the Poisson distribution

is the Chi-square test , where :

$$\chi^2 = \frac{\sum \left[(\text{observed value}) - (\text{mean value})\right]}{\text{Mean value}} \qquad (5.1)$$

Fig. 5.4 provides the probability , P , of

conformity to the Poisson distribution from a given

value of χ^2 .

FIGURE 5.4. A plot of the Chi-square distribution. For each curve, p gives the probability that a random sample of N numbers from a true Poisson distribution would have a larger value of χ^2/ν than that of the ordinate. For data for which the experimental mean is used to calculate χ^2, the number of degrees of freedom $\nu = N - 1$.   REF. /69/

A probability of less than 0.02 would indicate abnormally large fluctuations , whilst a probability of greater than 0.98 reflects a non-random distribution. A probability of 0.5 indicates a perfect fit . The data of Table 4.1 and ·Table 4.2 closely approximated a perfect fit ..A typical frequency distribution from a set of ^{235}U measurements is presented in fig . 5.5 .
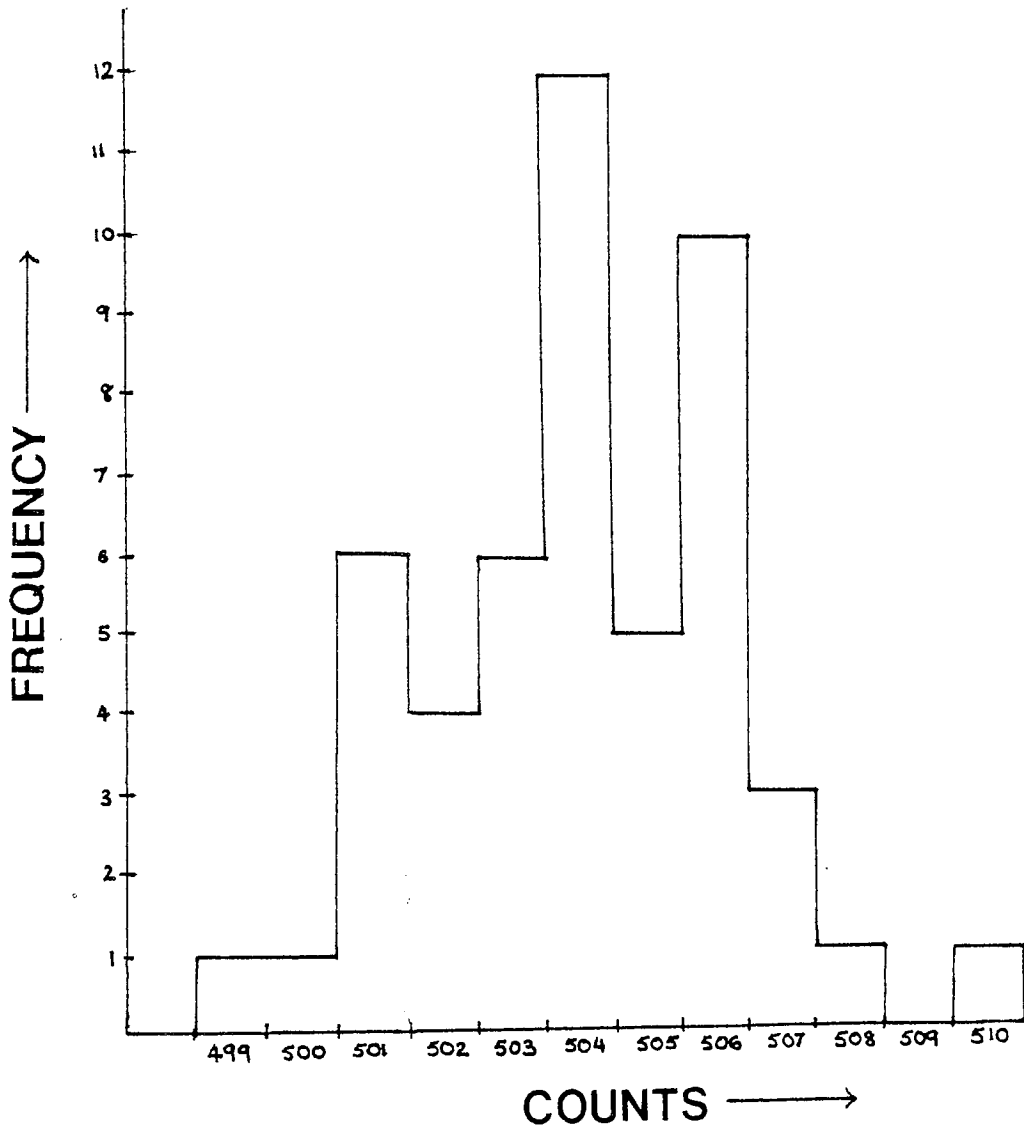
Fig. 5.5 : Frequency distribution from a set of
50 measurements from the ^{235}U assay .

5.1.2 Corrections applied to the 2π-activity

measurements

Dead Time

All pulse counting systems require a

minimum interval of time separating two events in

order to record such events as separate . This time
interval is referred to as the dead time , T_d , of
the system . Counting losses can be corrected for
through consideration of either of two models of
dead time behaviour , viz. the paralyseable model
and the non-paralyseable model . These models are
discussed by Knoll /69/ . At low count rates (less
than 1/10 T_d) the two models merge , hence either
is applicable . Using the non-paralyseable model , the
relationship between the measured counts , m , and
the actual counts , n , is given by :

$$n = \frac{m}{1 - mT_d} \qquad (5.2)$$

Although most analogue to digital
convertors (ADCs) possess a facility for dead time
correction , i.e. through counting in live time ,
this facility may not fully correct for dead time .
Proper dead time correction requires a knowledge of
the pulse processing system of the particular ADC
used .

Fig . 5.6 illustrates the pulse processing
system in an ADC with reference to dead time .
During the time to peak period , an input pulse with
sufficient amplitude to exceed the lower level
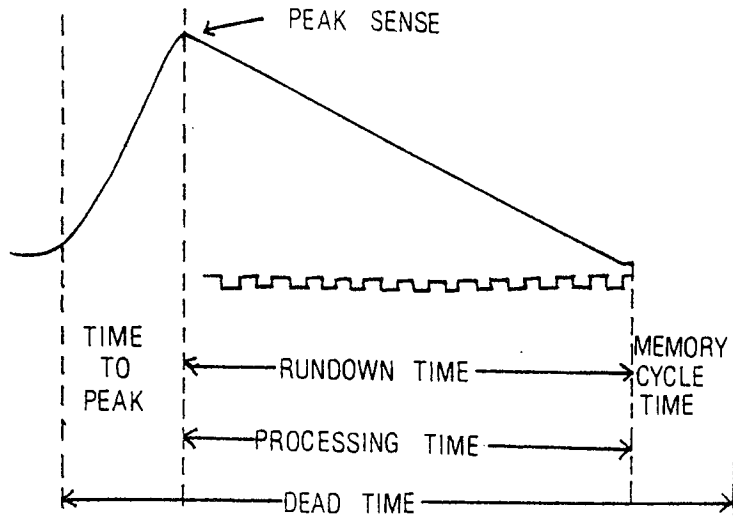
Fig . 5.6 : Dead time in an ADC .

discriminator threshold charges a capacitor . When
the peak of the pulse is sensed , the voltage on the
capacitor is discharged . The time required to
discharge the capacitor to baseline is directly
proportional to pulse height . At the start of
discharge , a gate is opened to allow the binary
address scalar to count clock pulses from the
oscillator in the ADC . At the end of discharge ,
the information in the scalar - the clock pulses
counted - is passed into the memory address register.
An input gate prevents the acceptance of additional
input pulses from the time the peak is detected
until address transfer is complete .

When counting is performed with the ADC
in the live time mode , the elapsed time is gated
off so as not to include the processing time . This
processing time , however , may not include the time
to peak and memory address times .

Methods of dead time measurement are
discussed in refs. /70 , 71/ . The total dead time
for the system used in this work was accurately
measured using a pulse generator operating in the
double pulse mode and a calibrated oscilloscope .
Double 10KHz pulses with variable delays were
introduced into the ADC input (Fig. 5.7) .
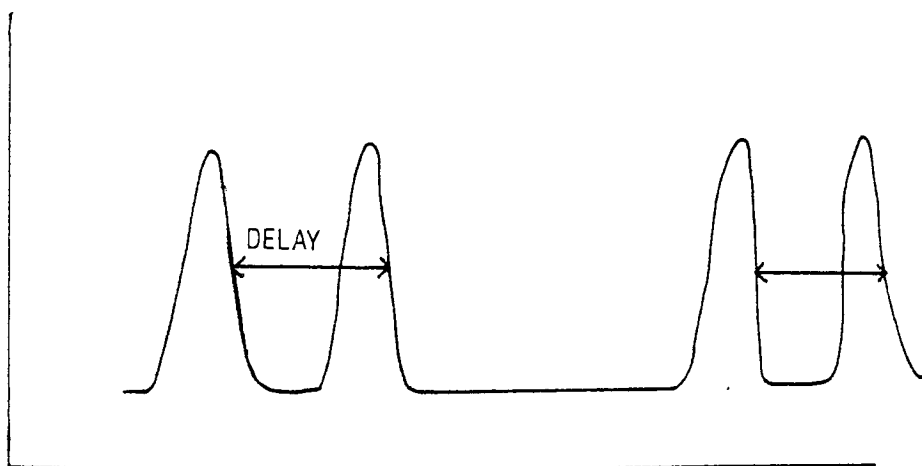
Fig. 5.7 : Double pulses with delay .

When the delay between the double pulses equals the
total dead time , the count rate was halved .

It is clear from the preceeding discussion
that the processing time is pulse amplitude dependent

when in the variable dead-time mode . Correction
for variable dead time , however , is cumbersome .
Hence , all measurements were performed in the
fixed dead-time mode . In this mode the dead time
was found to be 12.6 microseconds for the ADC , and
0.265 microseconds for the single channel analyser-
scalar combination .

5.1.2 Absorption Corrections

Absorption corrections for the 2π assay
are similar to those applied to the fission counts
discussed in the previous chapter . A range of
11.2 $\pm$ 1.5 mg cm^{-2} for 4.8 Mev alpha particles
was used in the calculation .

The deposit uniformity has been mapped
by Akhtar /64/ . The counting was performed using a
silicon surface barrier detector . A collimator
arrangement ensured that activity from a selected
region only would reach the detector . Thirty four
regions , each of 3 mm diameter , were mapped , the
results of which are depicted in fig . 5.8 . The
σ/t value , i.e. the ratio of the root mean square
deviation of the thickness to that of the mean
thickness , obtained from these measurements, is
0.32 . As discussed earlier in subsection 4.3.2 , an
additional σ/t value corresponding to the method

of uranium deposition is required .
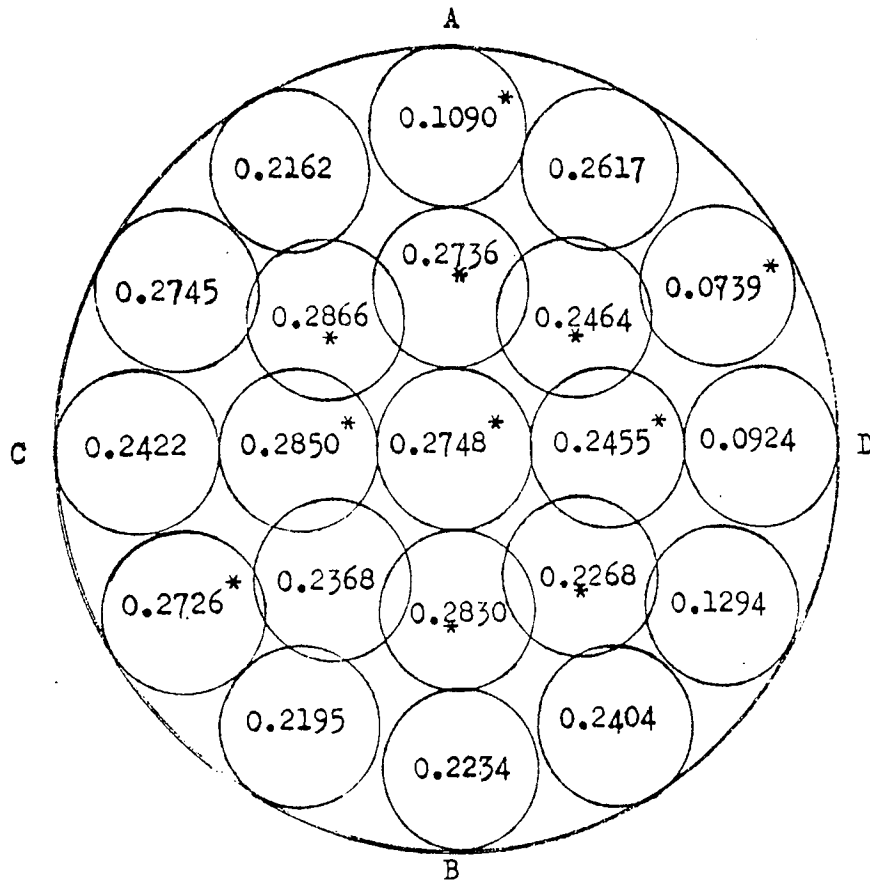
Fig. 5.8 : Non-uniformity in the ^{235}U foil , as

mapped by Akhtar .

White op. cit. suggests a value of $\sigma/t = 0.4$ (for

electrodeposition) which , when summed quadratically

with the value of 0.32 (for deposit non-uniformity) ,

provides an overall σ/t value of 0.5 . This σ/t

value , when used in conjuction with relation (4.6) ,

provides the fraction of counts F lost in absorption.

The correction factor for absorption C_{ab} , which
is multiplied to the observed alpha-particle counts,
is thus given by the relation :

$$C_{ab} = \frac{1}{(1 - F)} \qquad (5.3)$$

5.1.3 Scattering Corrections

Alpha particles emitted in the direction
of the platinum backing of the deposit can be
scattered back through small angle collisions into
the counting volume . This results in an increase
in the counts observed . Similarly , alpha-particles
emitted towards the counting volume can be scattered
back into the deposit , resulting in lost counts .
Crawford /73/ has calculated the "scatter in"
correction whilst White , op. cit. , has calculated
the "scatter out" correction . Fig . 5.9 , provided
by White , illustrates the calculated scattering
corrections with foil thickness .

The overall scattering corresponding to
a residual range of 5 mm (0.8 Mev alpha particles
residual range) and a deposit thickness of 0.1 mg cm^{-2}
as determined from fig . 5.9 , is 2.45% of "scatter
in" . Since the effect of "scatter in" is to increase
the observed counts , the correction factor C_{scatt}

applied for scattering is given by :

$$C_{scatt} = \frac{1}{1 + F_{scatt}} \qquad (5.4)$$
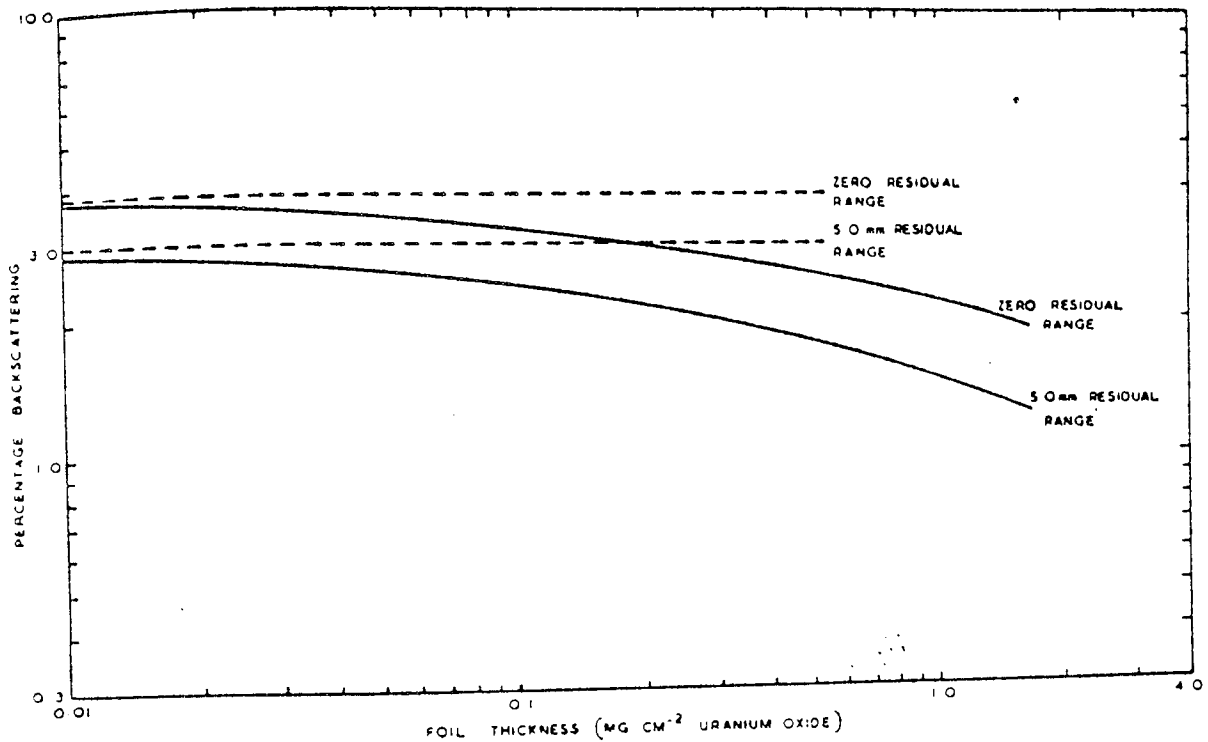

FIG. 5.9 : Calculated variation of scattering with foil thickness.

    - - - - Backscattering (B) calculated by Crawford
    ——— Net scattering (B−C)
    C   Scatter out correction

5.1.4 The Corrected Alpha Particle Activities in 2π Geometry

A tabulation of the correction factors applied to the 2π measurements , together with associated uncertainties are presented in Table 5.4:

Table 5.4 : Correction Factors Applied to the 2π Measurements

Corrections	^{235}U (2π geometry)	^{238}U (2π geometry)
Absorption	1.00596	1.01124
Scattering	0.97609	0.9775
Dead time	1.00013	Negligible
Uncertainties		
Statistics	$\pm$ 0.04%	$\pm$ 0.23%
Absorption	$\pm$ 0.1%	$\pm$ 0.17%
Scattering	$\pm$ 0.05%	$\pm$ 0.05%
Total	$\pm$ 0.1%	$\pm$ 0.30%

The sample activities are determined by multiplying the experimentally observed 4π activity by the correction factors in Table 5.4 . Following from the data in Tables 5.2 and 5.3 , the alpha-particle activities for the ^{235}U foil and the ^{238}U foil are 990 $\pm$ 1 ds^{-1} and 8.5 $\pm$ 0.02 ds^{-1} respectively .

5.2 The Low Geometry Assay

Low geometry measurements were made in order to improve the accuracy of the alpha assay . In low geometry counting , no corrections for absorption or small angle scattering of alpha

particles need be applied since both these effects
are limited to alpha particles emitted at small
grazing angles to the deposit surface . Nevertheless,
large angle Rutherford Scattering is possible and ,
although small , has to be corrected for . White ,
op. cit ., calculates a "scatter in" correction of
0.15% and a "scatter out" correction of 0.10% ,
providing an overall "scatter in" correction of
0.05% .

Fig. 5.10 illustrates the vacuum system
and the vacuum chamber used , into which the silicon
surface barrier detector and the uranium foil were
placed . The solid state detector was mounted so
as to facilitate the variation of source to detector
distance . All measurements were made with the
vacuum chamber pressure maintained to below 10^{-6} mbar.

The solid state detector used was a
totally depleted Ortec model no . 8-019-150-300 .
A maximum H.T. voltage supply of 120 volts provided
a maximum sensitive depth of 300 microns , sufficient
for the detection of 6.0 Mev protons and 20 Mev
alpha-particles . Typical resolutions of 1.9% for
4.8 Mev alpha-particles from ^{234}U were observed
(see fig . 5.11) .
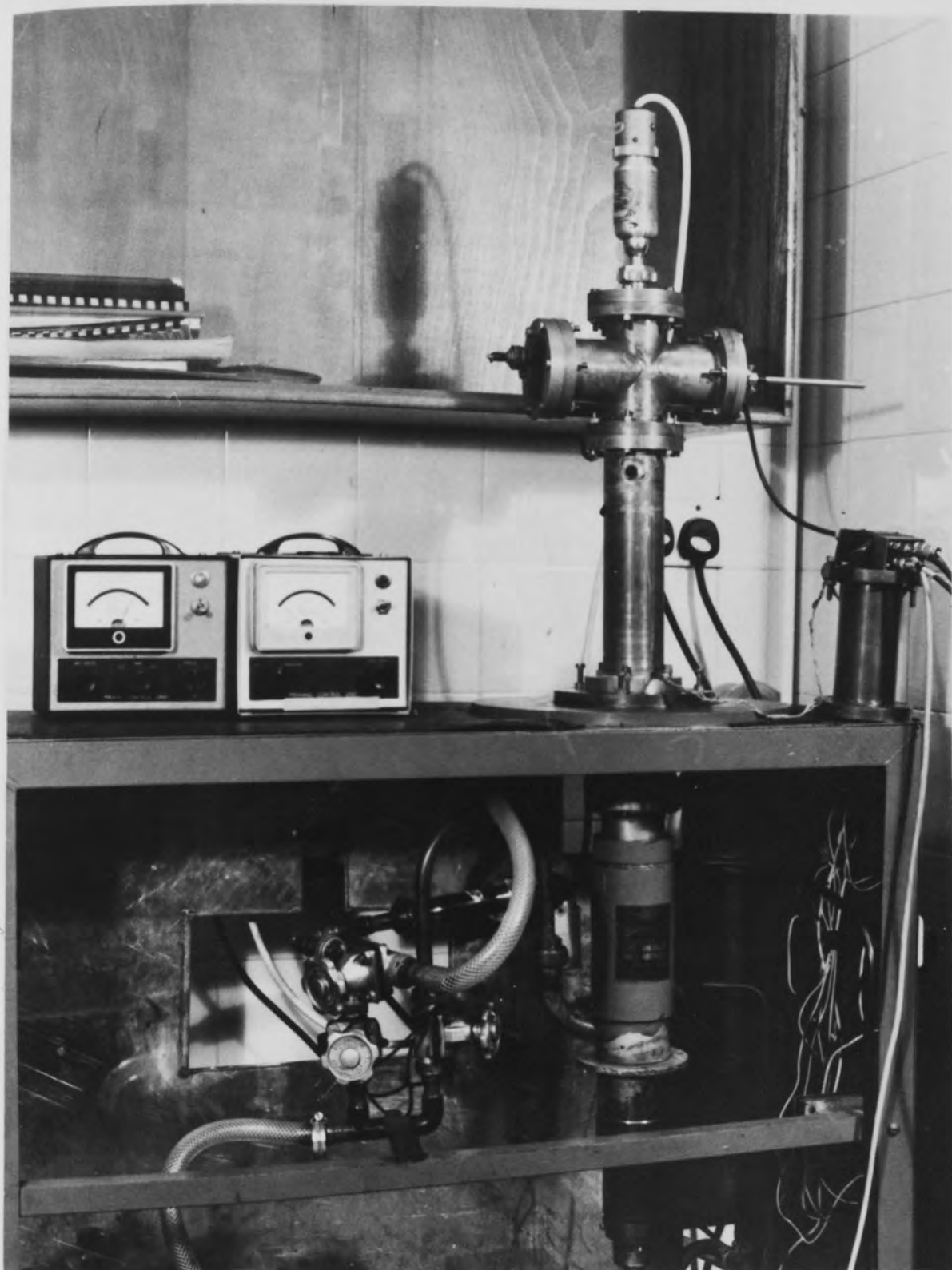
FIG. 5.10: THE VACUUM CHAMBER USED FOR
LOW GEOMETRY COUNTING
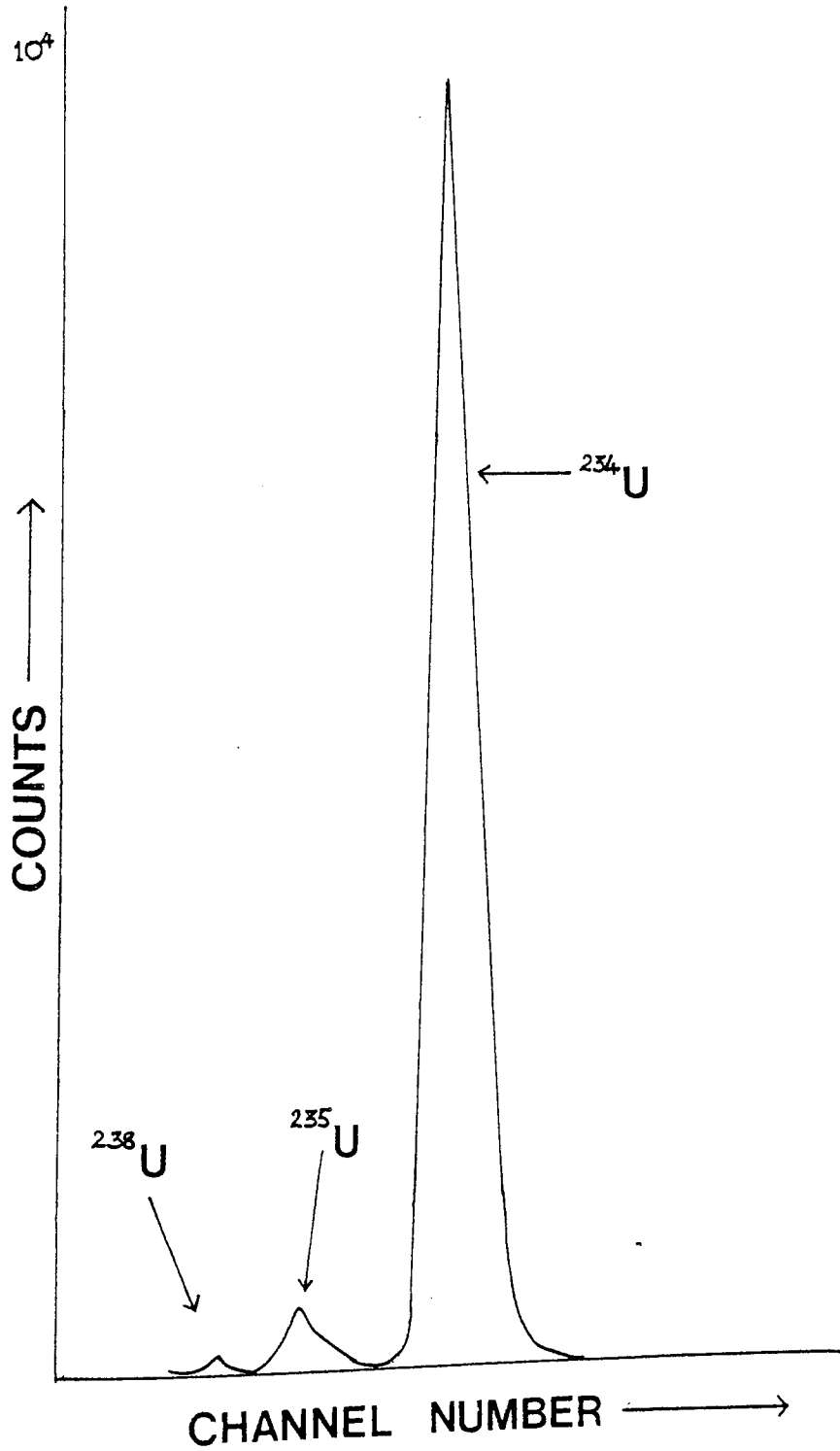
FIG. 5.11 LOW GEOMETRY SPECTRUM FROM SOLID STATE DETECTOR

5.2.1 Detection Efficiency

Given a detector count rate C from low geometry measurements , the 4π-activity , A , can be determined using the relation :

$$A = 4\pi C/\Omega \qquad (5.5)$$

where Ω is the solid angle subtended at the detector by the source . Thus , $\Omega/4\pi$ provides the detection efficiency . For a point source , the solid angle can be shown to be :

$$\Omega = 2\pi (1 - \cos \theta) \qquad (5.6)$$

where θ is the half angle subtended . For an extended source , in this instance , a disc source coaxial with , and with its plane parallel to a circular planar detector , a general expression for the solid angle can be described as :

$$\Omega = \int_{0}^{R_s} \frac{2\pi \, \Omega(R)}{\pi R_s^2} \, dR$$

where R_s is the source radius .

An exact solution of this solid angle is prohibitively difficult /74/ . Kojnin et al /75/ have used an approximate expression which is

integrated numerically . The calculation of Kojnin
et al fails , however , when applied to a source
having a radius larger than the sensitive radius of
the detector , which is the experimental configuration
used in this work . Jaffey /76/ provides a formula ,
in the form of a series expansion , applicable to
detector radii larger than the source radii . This
formula is given in equation 5.8 , where :

$$\varepsilon = \Omega/4\pi = (\tfrac{1}{2})(R_D^2 /H(H+1)) - (3/16)(R_s^2 \, R_D^2 \, D)/H^5$$
$$+ (5/32)(R_D^4 \, R_s^4 \, D)(D^2 - 3R_D^2 /4)/H^9 + \text{-----} \quad (5.8)$$

where R_s = source radius

R_D = detector radius

D = source detector distance

$H = (D^2 + R_D^2)^{\tfrac{1}{2}}$

A Monte Carlo method is an alternative
technique to the analytic approaches described above.
However , with the Monte Carlo approach , a large
amount of computer time is required to generate
sufficient statistical accuracy . (An accuracy of
1% requires 10,000 successful trials) . Hence , the
analytic formula of Jaffey was used in preference
to the Monte Carlo method .

The source-detector configuration provided a problem in the use of equation 5.8 . Since the detector was not flush mounted , the sensitive detector surface was 4.05 mm from the front surface of the detector casing (Fig. 5.13) . Where $R_s \leq R_D$, Jaffey's formula would still be applicable . Unfortunately , in this work , the source radius was larger than the detector radius , introducing a systematic error to the formula and necessitating the derivation of a further, approximate expression .

The geometric configuration is illustrated in fig . 5.13 . For equidistant point sources at a distance R from the centre of the source , equation 5.6 holds exactly for the case $\alpha = 0$, but is increasingly approximate as α is increased . As the source to detector distance D is increased , the maximum possible value for α (at $R = R_s$) decreases . Hence , equations 5.6 and 5.7 can be used to provide an approximate but sufficiently accurate solution at large values of D .

For $R_s \geq R_D$:

$$\mathcal{E}_1 = \int_{R_D}^{R_s} \left(1 - \left[\frac{L^2 + M^2 - P^2 + 2LM}{4LM} \right]^{\frac{1}{2}} \right) R dR \qquad (5.9)$$

FIG. 5.13
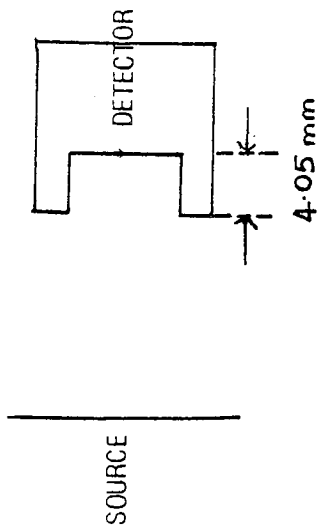
(a) SCHEMATIC DIAGRAM OF SOURCE -
DETECTOR CONFIGURATION
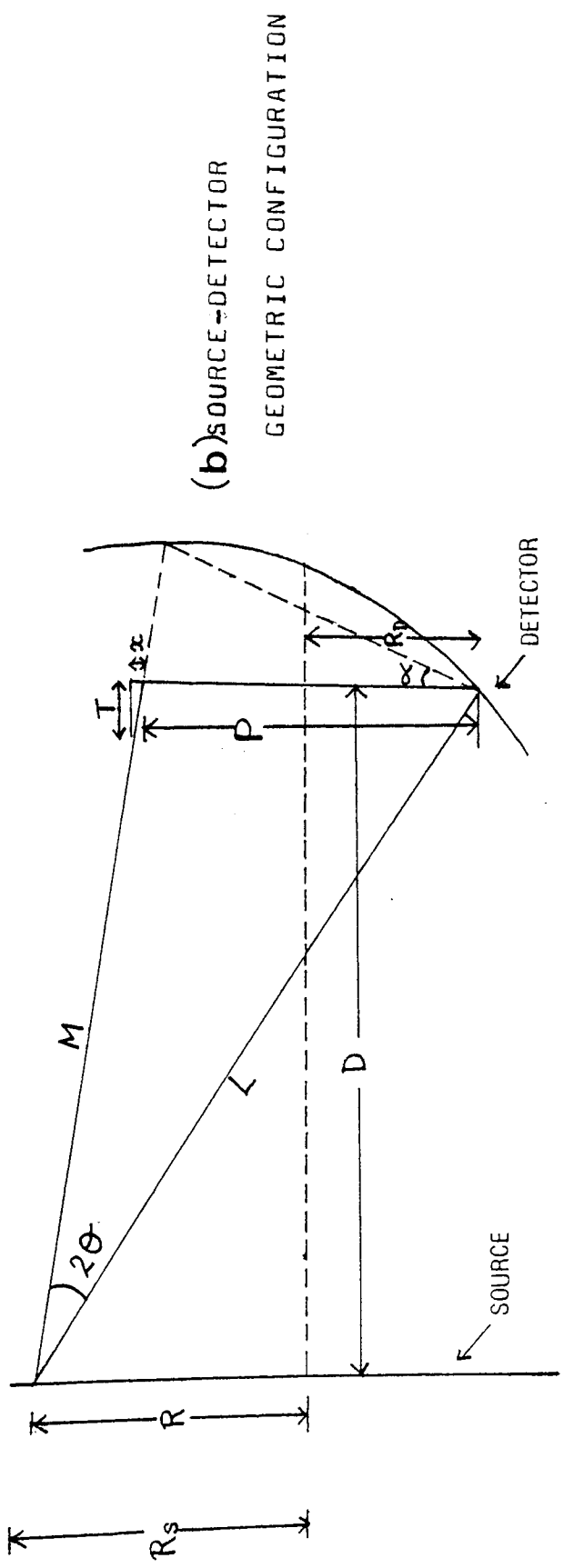
(b) SOURCE-DETECTOR
GEOMETRIC CONFIGURATION

where P = 2S - x

$$x = T(R - S)/(D - T)$$

$$M^2 = D^2 + (R + x - S)^2$$

$$L^2 = D^2 + (R + S)^2$$

For $R_s \leq R_D$

$$\mathcal{E}_2 = \int_0^{R_D} \left(1 - \left[\frac{L^2 + M^2 - P^2 + 2LM}{4LM} \right]^{\frac{1}{2}} \right) RdR \qquad (5.10)$$

where x = 0 .

In the case where $R_s > R_D$, the detection efficiency , $\mathcal{E}$, is given by $\mathcal{E}_1 + \mathcal{E}_2$, whilst for $R_s < R_D$ it is given by $\mathcal{E}_2$ with the limits of integration set to R=0 to R = R_s . The numerical integrations were performed using a Commodore PET 2001 series computer . The program is described in Appendix 1 .

In order to check the accuracy of these formulae , the calculated efficiencies were compared with results obtained from using the analytic method of Jaffey and the Monte Carlo method of Williams /77/. For comparison , the calculations were made for a flush mounted configuration . Table 5.5 illustrates the results of the calculation .

Although the Monte Carlo calculation was performed to an accuracy of 3% , the calculations differed systematically by 6% from the present

method and hence would agree only if a statistical
uncertainty of two standard deviations was considered.

Table 5.5 : Comparison of detection efficiencies at
various source to detector distances .

D (cm)	Williams	Jaffey	Present
1.905	0.026	0.0250	0.0243
4.205	$6.7E^{-3}$	$6.349E^{-3}$	$6.248E^{-3}$
4.405	$6.1E^{-3}$	$5.812E^{-3}$	$5.761E^{-3}$
8.5	-	$1.627E^{-3}$	$1.623E^{-3}$
8.6	-	$1.590E^{-3}$	$1.586E^{-3}$
8.705	$1.6E^{-3}$	$1.552E^{-3}$	$1.549E^{-3}$
8.90	-	$1.486E^{-3}$	$1.483E^{-3}$

At a source detector distance of 8.705 cm , the
efficiency using equation (5.9) and equation (5.10)
differed from that using the method of Jaffey by
only 0.2% .

The effect of this systematic difference
can be partially nullified if the method of Jaffey
is used to determine the detection efficiency for
a flush mounted configuration , and a correction
factor applied to these results . This correction
factor , E , was calculated from equations 5.9 and
5.10 , and is the ratio of the efficiencies with

flush mounting to that without . These calculations
are presented in Table 5.6 .

Table 5.6 : Comparison of Detection Efficiencies
With and Without Flush Mounting

Distance	$\varepsilon_{without}$	ε_{with}	E
1.905	0.235	0.243	0.96708
4.205	$6.165E^{-3}$	$6.248E^{-3}$	0.98671
4.405	$5.656E^{-3}$	$5.728E^{-3}$	0.98743
8.600	$1.5768E^{-3}$	$1.586E^{-3}$	0.99420
8.705	$1.531E^{-3}$	$1.549E^{-3}$	0.98838
8.8	1.5074	$1.5164E^{-3}$	0.994065

Given that a systematic error exists in
the calculation of efficiency through equations 5.9
and 5.10 , the correction factor E can be written as:

$$E = \frac{\varepsilon_{without}\ K_{without}}{\varepsilon_{with}\ K_{with}} \qquad (5.11)$$

where $K_{without}$ and K_{with} are the correction factors
for the systematic errors due to equations 5.9 and
5.10 , without and with flush mounting respectively.
Given that $K_{without} \simeq K_{with}$ = 0.9981 , the error in
E is largely eliminated . Following from a conservative

estimate , the error in ε is probably less than 0.05%.

5.2.2 The Alpha-particle Activity as determined from Low Geometry Measurements

Table 5.7 presents a set of results calculated from low geometry measurements at D=8.705 cm . The activities presented have been corrected for the detection efficiency , as described in section 5.2.1, and for large angle scattering . (White , op. cit.).

Table 5.7 : Activities in disintegrations s^{-1} from the ^{235}U foil determined from low geometry measurements . D = 8.705 cm

981 $\pm$ 3	983 $\pm$ 3
980 $\pm$ 3	984 $\pm$ 3
979 $\pm$ 3	980 $\pm$ 3
MEAN = 981 $\pm$ 1	

The corrections applied to the low geometry measurements and the associated uncertainties are listed in Table 5.8 .

Table 5.8 : Corrections and the associated
uncertainties for the ^{235}U foil
(low geometry) .

Efficiency D = 8.705 cm	$1.5340 \ E^{-3}$
Large Angle Scattering	0.9995
Dead Time	Negligible
Uncertainties	
Statistics	0.1 %
Efficiency	0.05 %
Total	0.1 %

The mean value of 981 $\pm$ 1 ds^{-1} differs
by 1% from the activity determined in 2π geometry
(990 $\pm$ 1 d s^{-1}) even though the necessary corrections
had been applied . The most likely cause for this
discrepancy is the non-uniformity in deposit
thickness (see fig . 5.8) . A similar discrepancy
has been observed by White /78/ . Whilst in 2π
geometry , the non-uniformity introduces an error
in the absorption correction in a manner which can
be accounted for through the method described in
subsection 5.1.2 , in low geometry , the non-uniformity
introduces an error in the efficiency calculation

where a uniform deposit has to be assumed .
Unfortunately , this error cannot be easily corrected
for in the low geometry measurement . In such
instances , activities obtained from low geometry
assays would require calibration relative to an
assay using a destructive method . However , this
is not possible , since the foils are required for
future use . In consequence , the results obtained
from the 2π geometry measurements are regarded to
be more reliable , and have been used in flux
measurements .

5.3 The Uranium Content

The number of uranium nuclei can be
determined using the relation :

$$\frac{dN}{dt} = N\lambda_{eff} \qquad (5.12)$$

where dN/dt represents the total activity , N the
total number of radioactive nuclei , and λ_{eff} the
effective decay constant associated with the sample.
Hence , λ_{eff} can be represented as :

$$\lambda_{eff} = (\lambda_{235} \ ^{o}\!\!\diagup\!\!_{o} \ _{235} + \lambda_{238} \ ^{o}\!\!\diagup\!\!_{o} \ _{238} + \ldots\ldots etc)$$

$$(5.13)$$

where $^o\!\backslash\!o$ is the fractional abundance of an individual
isotope in a sample .

The half-lives used in the calculation from
which the decay constants were obtained , are tabulated
in Table 5.9 /78,79/ .

Table 5.9 : Half-lives used in the calculation of
uranium content .

Isotope	$T_{\frac{1}{2}}$	Uncertainty
U - 234	$2.475 \times 10^5 y$	$\pm\ 0.65\%$
U - 235	$7.1 \times 10^8 y$	$\pm\ 2.8\%$
U - 236	$2.39 \times 10^7 y$	-
U - 238	$4.5 \times 10^9 y$	$\pm\ 1.5\%$

The uncertainties of 0.1% and 0.3% quoted
for the U - 235 and U - 238 foils respectively are
in general agreement with accuracies for 2π activity
measurements quoted in the literature . Nevertheless,
in considering achievable accuracies in determining
uranium content , uncertainties in the half-lives
would have to be included . An uncertainty of 0.65%
in the half-life of U - 234 and 1.5% in U - 238 ,
provides an overall uncertainty of 0.7% for the U-235
foil and 1.5% for the U - 238 foil . The contribution
to the overall uncertainty from the other isotopes
was found to be negligible , due to their low content.

Using relations 5.12 and 5.13 , the total number of uranium nuclei in the U - 235 and the U - 238 foils are $8.55 \pm 0.06 \times 10^{17}$ and $1.74 \pm 0.026 \times 10^{18}$ nuclei , respectively .

CHAPTER 6

THE NEUTRON SOURCE

CHAPTER 6

The Neutron Source

The selection of an appropriate reaction for the production of neutrons of a required energy range is primarily limited by available accelerator energies . In the Dynamitron accelerator used , the practical energy range is 0.75 Mev to 3.0 Mev . Where required , lower energies can be made available through the acceleration of doubly charged ions , e.g. d_2^{++} instead of d^+ .

Whilst target requirements can vary in accordance with the nature of an experiment , an ideal target should comply with the following requirements:

(a) High yield

(b) Small physical size

(c) Small energy spread with angle of emission

(d) Mimimum interference from competing neutron producing reactions

(e) Minimum amount of material in the vicinity of the target contributing to neutron scattering .

(f) Long life and ease of replacement

Where neutrons in the energy range of 1 Mev to 6 Mev are required , three commonly used source reactions are available . Table 6.1 lists these reactions

and their corresponding neutron energies from the
bombarding particle energies available from the
Dynamitron .

Table 6.1: Approximate neutron energies available

Reaction	Bombarding particle energy range (Mev)	Neutron energy range (Mev)
$^7Li(p, n)^7Be$	2.0 to 3.0	0.1 to 1.1
$^3T(p, n)^3He$	0.75 to 3.0	1.0 to 2.0
$D(d, n)^3He$	0.75 to 3.0	4.0 to 6.3

Fig . 6.1 illustrates the corresponding
excitation functions of the reactions listed above .
Although these reactions provide essentially mono-
energetic neutrons , in the $^7Li(p, n)^7Be$ reaction
at proton energies in excess of 2.38 Mev , transitions
to the first excited state of ^7Be result in a second
neutron group . However , the neutron flux contribu-
tion from this second neutron group can be corrected
for by use of the data of Bevington et al /80/ which
provides the ratios of the primary to secondary
neutron flux . Where neutron energies in excess of
8.5 Mev are required , the $D(d, n)^3He$ reaction produces
a secondary group of neutrons due to the break-up of
He-3 . In view of the requirement for neutron energies
of 4 Mev to 6 Mev , the $D(d, n)^3He$ reaction was

a. $T(p,n)^3He$ REACTION

E_n FROM 1.0 TO 2.0 Mev

b. $D(d,n)^3He$ REACTION

E_n FROM 4.0 TO 6.0 Mev

c. $^7Li(p,n)^7Be$ REACTION

E_n FROM 0.1 TO 1.3 Mev
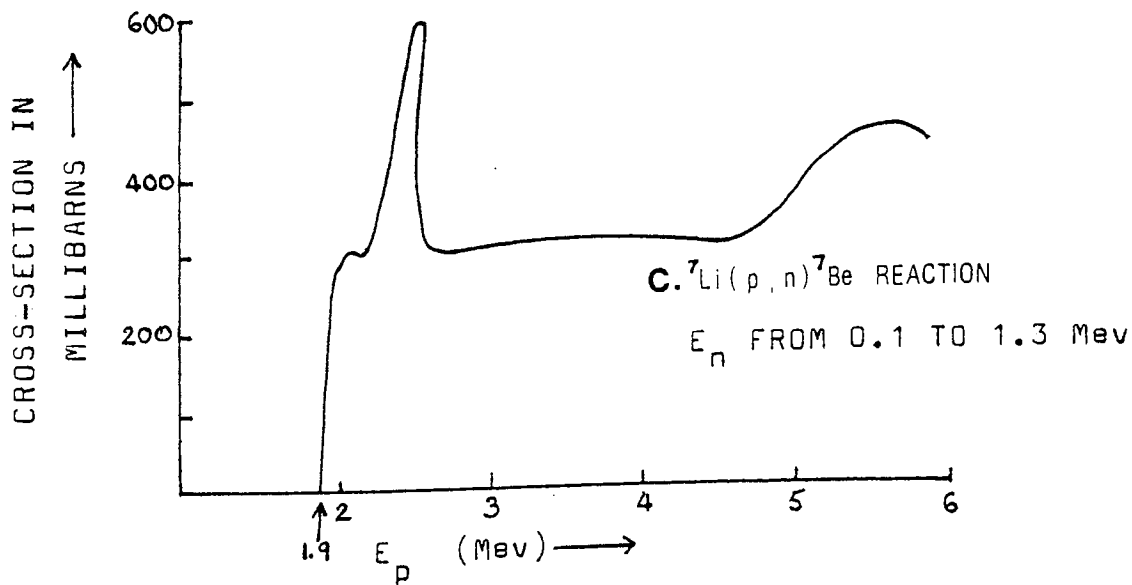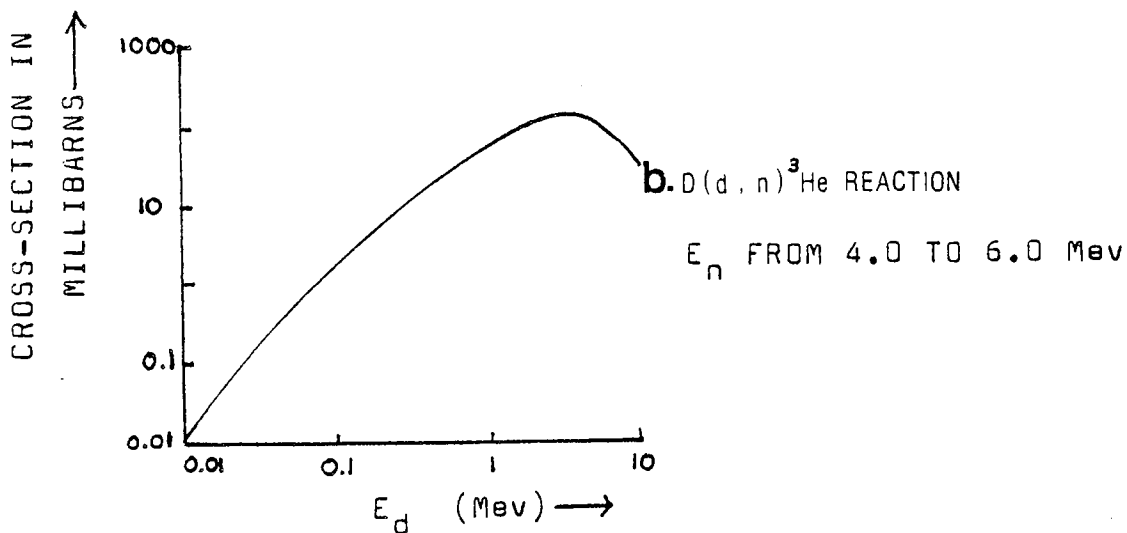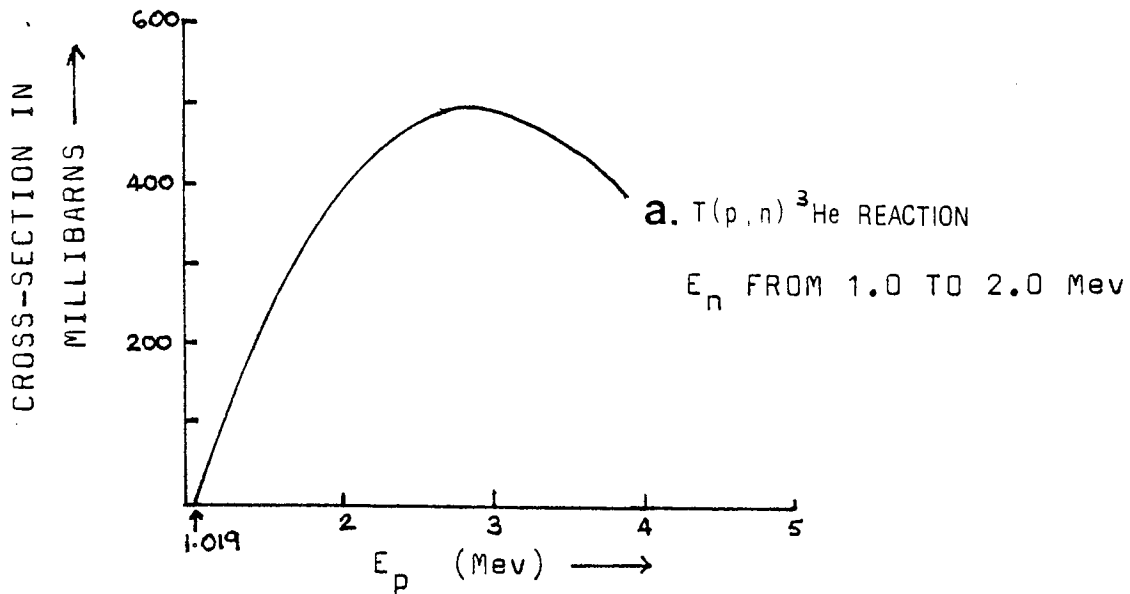
FIG. 6.1

selected for this work . A brief discussion of
deuterium targets follows .

6.1 Deuterium Targets

Various forms of deuterium targets are
available . These are :(1) heavy ice , (2) drive-in ,
(3) deuterated polythene , (4) deuterated metals and,
(5) gas targets . An excellent account of neutron
targets is presented by Coon /81/ , whilst deuterated
polythene targets are considered by Bartle et al/82/.

Heavy ice targets require sophisticated
cooling systems and are severely limited by vaporisa-
tion , unless beam pulsing , beam oscillation or
mechanical rotation of the target is employed . Extreme
measures of cold trapping are also necessary due to
rapid condensation of residual vapours . Drive-in
(loading of metals with deuterium through beam bombard
-ment) and deuterated polythene targets provide
relatively small neutron fluxes . Limitations in these
targets has led to the extensive use of deuterated
metal and deuterium gas targets .

A review of such metal targets is presented
by Morgan /83/ . Titanium is the most commonly used
metal substrate , due to its superior chemical
properties and low stopping cross-section . A ratio
of the order of 1:1 of hydrogen to titanium is

considered adequate . Significantly higher hydrogen content results in poor physical properties . Although the inherently high thermal conductivities of deuterated metal targets allows the use of higher beam currents than is possible in gas targets , the latter provide superior energy resolution .

In the course of a feasibility study for this work , the performances of deuterated titanium targets and gas targets were compared . For a deuterated titanium target of 0.62 cm^3 cm^{-2}* deuterium content , at 3.0 Mev bombarding particle energy , the energy degradation of the beam is 270 Kev , in comparison with 27 Kev for a gas target having the same deuterium content . Hence , at a given energy resolution , gas targets can provide fluxes of up to 10 times those available from deuterated metal targets , per microamp of beam current . On the Dynamitron , and where a 4 mm diameter collimator is used , the beam current limit on target is 10 μA. At beam energies of 3.0 Mev , the power dissipated in the target backing is 30 watts (at 10 μA) and , hence , target cooling is required .

* This is the thickest target available from the Radiochemical Centre , Amersham .

A further advantage of gas targets arises
from the production of background neutrons through
(d, n) reactions with low z target material
components . Usually , the contribution from these
background neutrons to the neutron flux and
irradiated sample activity can be corrected for .
However , in an investigation of the production of
background neutrons , Smith et al /84/ observed a
major contribution to originate from the formation
of a carbon deposit on the target . Whilst in a gas
target this contribution can be determined through
evacuation of the gas cell , determination of this
effect is not possible in a deuterated metal target.

Lastly , gas targets allow greater
flexibility of use since the gas pressure can be
readily varied to accomodate changes in the stopping
power of the gas with energy , and window thicknesses
may be varied to an extent , altering the deutron
energy range available .

Fowles /94/ has developed a water cooled
target assembly (fig . 6.5a) incorporating a
deuterated metal target which , when used in conjunc-
tion with a water cooled collimator , has withstood
up to 1.5 Kev of beam power . This target was used
in the present work when intense neutron fluxes were
required . However , the limitations of this target

are the poor energy resolution and the greater
quantity of material surrounding the target .
Consequently , for much of this work , a gas target
was used .

6.2 Gas Target Design

A gas target normally retains the gas in
a sealed enclosure . A thin metal window serves to
allow the accelerator beam to pass into the target
gas whilst retaining the gas pressure against the
beam-line vacuum .

The principal limitation of gas targets
relates to the puncture of the window at high beam
current densities . Whilst the maximum gas pressure
that can be retained by a window is directly
proportional to the window thickness , the maximum
permissible beam current density decreases with
thickness . Although higher gas pressures could
compensate for low beam currents , the limit on gas
pressure is set by the neutron energy resolution
required . Thus , in order to increase available
neutron fluxes , high beam currents are required .
Hence , the target window must be cooled .

Various methods have been employed to
provide increased heat removal , the simplest of
which uses a metal grid . This method is often

employed where large diameter windows are used .
In such instances , a significant portion of the
transmitted beam suffers scattering and energy
degradation by the edges of the grid .

More efficient methods of heat removal
employ direct air cooling of the target window .
One such method is described by Hill /85/ ; where
deuterium gas is circulated through a cooling
system and returned to the target cell through a jet
aimed at a 3 micron nickel window . Beam currents of
up to 7 microamps are reported for 2 Mev deutrons ,
over a 5 mm diameter beam spot . A more novel approach
is employed by Nobles /86/ , where two closely spaced
windows are utilised to provide two gas cells and
to increase gas cell pressure . The close proximity
of the windows and the elevated pressures provide
more efficient heat removal .

A further approach is available where beam
pulsing is employed as in time-of-flight experiments.
For a one micron nickel window and a beam pulse
duration of 10^{-5} s, (Coon, op. cit.) the temperature
rise is negligible for a 50 microamp beam of 6 Mev
deutrons and 1.5 mm diameter . Unfortunately ,
beam pulsing was not available .

A gas target design along the lines of
Nobles was initially envisaged . However , the

unavailability of pin-hole free nickel foils of 1
micron thickness at acceptable prices led to the
use of a single 3 micron window design .

Choice of Window Material

The required physical properties of the
gas cell window may be summarised as follows :

(1) Uniformity in thickness and pin-hole
free .

(2) Sufficient mechanical strength for the
retention of gas pressure over reasonably
large apertures.

(3) High thermal conductivity and melting
point , i.e. the ability to withstand
high beam currents .

(4) Low stopping cross-section to minimise
beam energy loss .

(5) Low multiple coulomb scattering .

(6) Low neutron production cross-section .

Four commonly used window materials are
nickel , molybdenum , aluminium and tantalum . Each
of these materials has particular advantages under
specific operating conditions .

Where good neutron energy resolutions (lower gas pressure) and minimum energy losses in the window are required , aluminium provides an optimum choice . Aluminium has a high thermal conductivity and , therefore , in spite of its low melting point , the maximum beam current density tolerable is $2\frac{1}{2}$ times greater than for nickel . The disadvantages of aluminium are its low mechanical strength and large neutron production cross-section (low Z).

Tantalum has a low (d, n) reaction cross-section (high Z) and poor drive-in properties . The stopping power , however , is high . Also , it is subject to embrittlement when allowed to cool in the presence of hydrogen .

Where intense neutron fluxes are required , molybdenum is perhaps the best choice . Its high thermal conductivity and melting point allows $12\frac{1}{2}$ times more beam current densities than is possible with nickel . The tensile strength of molybdenum is twice that of nickel , permitting the use of higher gas pressures . Unfortunately , the thinnest pin- hole free foil readily available was 5 microns thick.*

*5 μm foil available from Goodfellow Metals , Ltd., Cambridge . Four micron thick pin-hole free molybdenum foils are available from Reactor Experi-ments INC. , SAN CARLOS 94070 , U.S.A. The agents in the U.K. are Ortec Ltd .

The corresponding energy loss in the window would
be 416 Kev at a deutron energy of 3.0 Mev , whilst
at lower energies the energy loss would be greater .

Some data relevant to the selection of an
appropriate window material is presented in tables
6.2 and 6.3 , and fig . 6.2 . For this work , nickel
was considered to provide acceptable properties .
Deutron energy losses across the window may be
computed from stopping cross-section presented in
fig . 6.1 .

Fig. 6.3 illustrates the gas target designed
for this work . A 3 microns thick nickel window was
soft soldered onto a copper washer of external
diameter 1 cm and internal diameter of 0.6 cm . The
maximum gas pressure which can be retained by the
window is determined from the yield strength data
presented in table 6.2. The force exerted by the gas
on the window is taken up by the circumference of
the foil at the point where it is pivoted , viz. the
inner diameter of the washer . Hence , the maximum
permissible pressure across the window , P_{max} , is
given by :

$$P_{max} = \frac{2Yt}{R}$$

(6.1)

where Y is the yield strength , t the foil thickness

Table 6.2 : Physical Properties of some Materials

used in Neutron Targets /95/

Metal	Atomic Number	Tensile Strength	Yield Strength	Thermal Conductivity	Melting Point
Aluminium	13	46.8 MPa	11.7 MPa	$2.37\,wcm^{-1}°C^{-1}$	$660°C$
Titanium	22	237 MPa	137 MPa	0.17 "	1660
Nickel	28	317 MPa	59 MPa	0.92 "	1453
Molybdenum	42	620 MPa	-	1.4 "	2617
Tantalum	73	344 MPa	214 MPa	0.54 "	2996

Table 6.3 : Changes in the Tensile Strength of

Nickel with Temperature /96/

Temperature	Tensile Strength
$20°C$	317 MPa
$150\ °C$	310 MPa
$250°C$	310 MPa
$370°C$	255 MPa
$480°C$	155 MPa

Fig.6.2 Stopping cross-sections for various materials used in neutron sources. Stopping cross-sections are multiplied by the target thickness in nuclei cm-2 to provide energy loss. Ref. /81/ .

and R the foil radius . Using R=0.3 cm and Y=59 MPa ,
P_{max} is 1.2 bars . The gas cell was used at a pressure
of 1 bar without damage to the window .

Choice of other gas cell materials

The primary design requirements of the
gas cell are summarised as follows :

(1) Thin walls to minimise scattering

(2) Low (d, n) reaction cross-section
material

(3) An end window (beam stop) with high
tensile strength , high thermal
conductivity and poor drive-in properties.

The gas cell was made from stainless steel
of 0.25 mm thickness , with a 0.1 mm thick molybde-
num beam stop . For low neutron production , the
ideal material would have been tantalum , but the
use of tantalum was eliminated by consideration of
the cost of the material required . Where deutron
energies significantly higher than 3 Mev are available,
the gas cell (excluding the window) may be lined with
gold (Smith et al , op. cit.) . The thickness of
the gold layer should be sufficient to degrade the
deutron energy below the threshold for neutron
production in the walls of the gas cell , but not
completely , in order to avoid drive-in neutron

production in the gold layer .

Molybdenum was selected for the beam stop material due to its superior heat conducting proper- ties . Whilst gold has been used by some workers (Nobles , op. cit .) for its high thermal conductivity and high threshold for neutron production , it provides an undesirably high drive-in neutron yield/87/.

Gas Cell Dimensions

The limit on target length is set by divergence of the beam through multiple Coulomb scattering as it traverses the window . Divergence of the beam can be determined through the formulae of Fermi /88/ . The mean square scattering angle , $\langle \Theta^2 \rangle$, can be calculated from :

$$\langle \Theta^2 \rangle = (2\pi z^2 Z^2 e^4 N/E^2) \ln (Ea_0/e^2 Z^{4/3} z) \qquad (6.2)$$

where z and Z are the atomic numbers of the bombarding and target (window) nuclei , e is the electronic charge , N the number of window nuclei per centimetre square , E the bombarding particle energy in electron volts and a_0 the radius of the hydrogen atom . From (6.2) , the root mean square scattering angle is 2.5^o for a 3 microns thick nickel window . Hence , for a 30 mm long gas cell

- the length of the gas cell used in this work - the deviation of the beam is only 1.3 mm at the beam stop . The gas target designed is depicted in figs. 6.3 to 6.5 .

The target cooling and gas filling system

The permissible beam current was maximised by introducing a cooling system in which the deuterium gas in the target was circulated past the target window at high speeds . Further , in order to achieve more effective heat removal from the window , the deuterium gas was pre-cooled with liquid nitrogen . A schematic diagram of the cooling system and the gas filling system is shown in fig . 6.6 .

In order to avoid accidental damage or weakening of the window during evacuation of the target chamber , the beam line and the gas cell are evacuated simultaeously . The following procedure was adopted :

With valves A and C open , but B and D closed , valve B was opened slowly . At a pressure of 10^{-3} mbar , valve C was closed . The system was filled slowly with deuterium through the fine control valve D . When the beam line vacuum reached a pressure low enough for the operation of the ion pump , valve A was closed in order to isolate the beam line from

INLET

NICKEL WINDOW
(3 micron)

VITON O-RINGS

MOLYBDENUM
BEAM STOP

COPPER WASHER

OUTLET
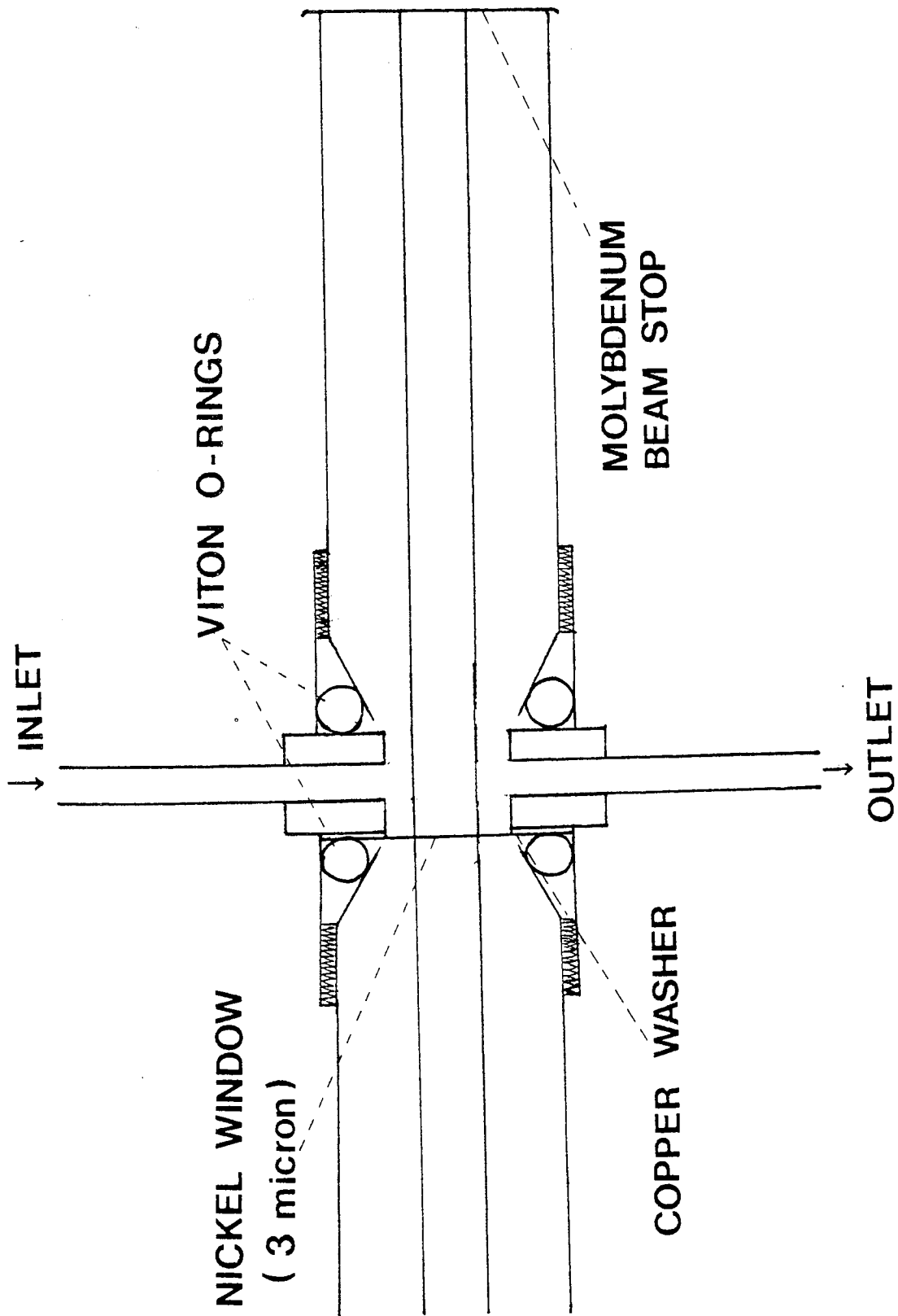
FIG. 6.3: SECTIONAL VIEW OF THE GAS TARGET
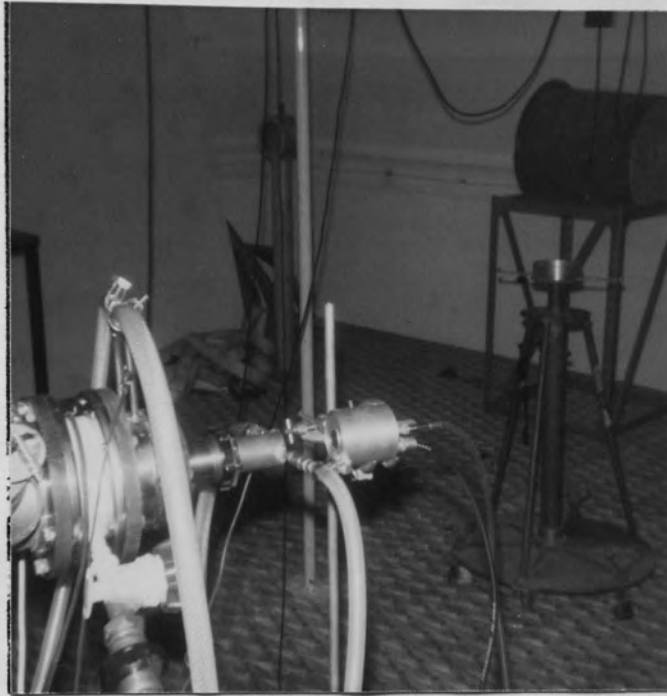
(a) THE TARGET OF FOWLES
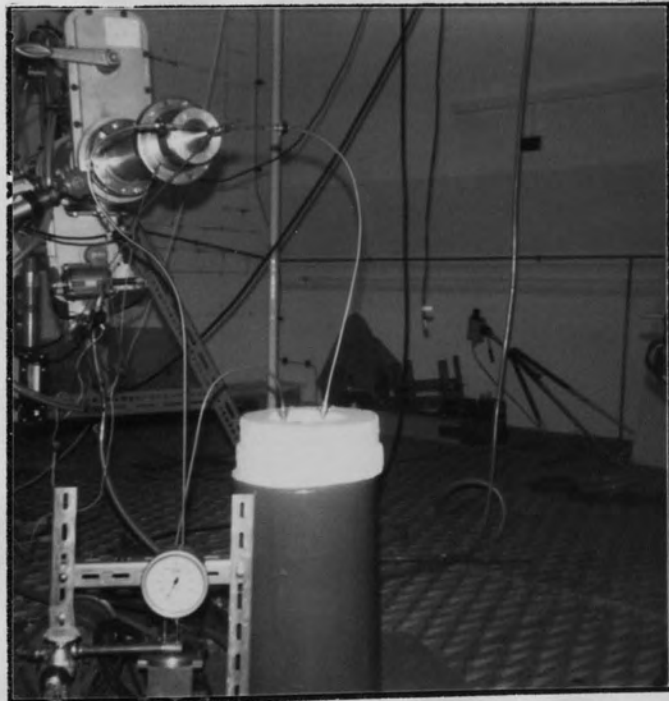

(b) TARGET USED FOR THE PRESENT WORK

FIG. 6.5

BEAM LINE

GAS TARGET

APERTURE (3 mm)

APERTURE (5 mm)

AUTOMATIC GATE VALVE

LIQUID NITROGEN

CIRCULATION PUMP

PRESSURE GAUGE

DEUTERIUM CYLINDER

C

D

A

B

ROUGHING CART (ROTARY AND DIFFUSION PUMP)
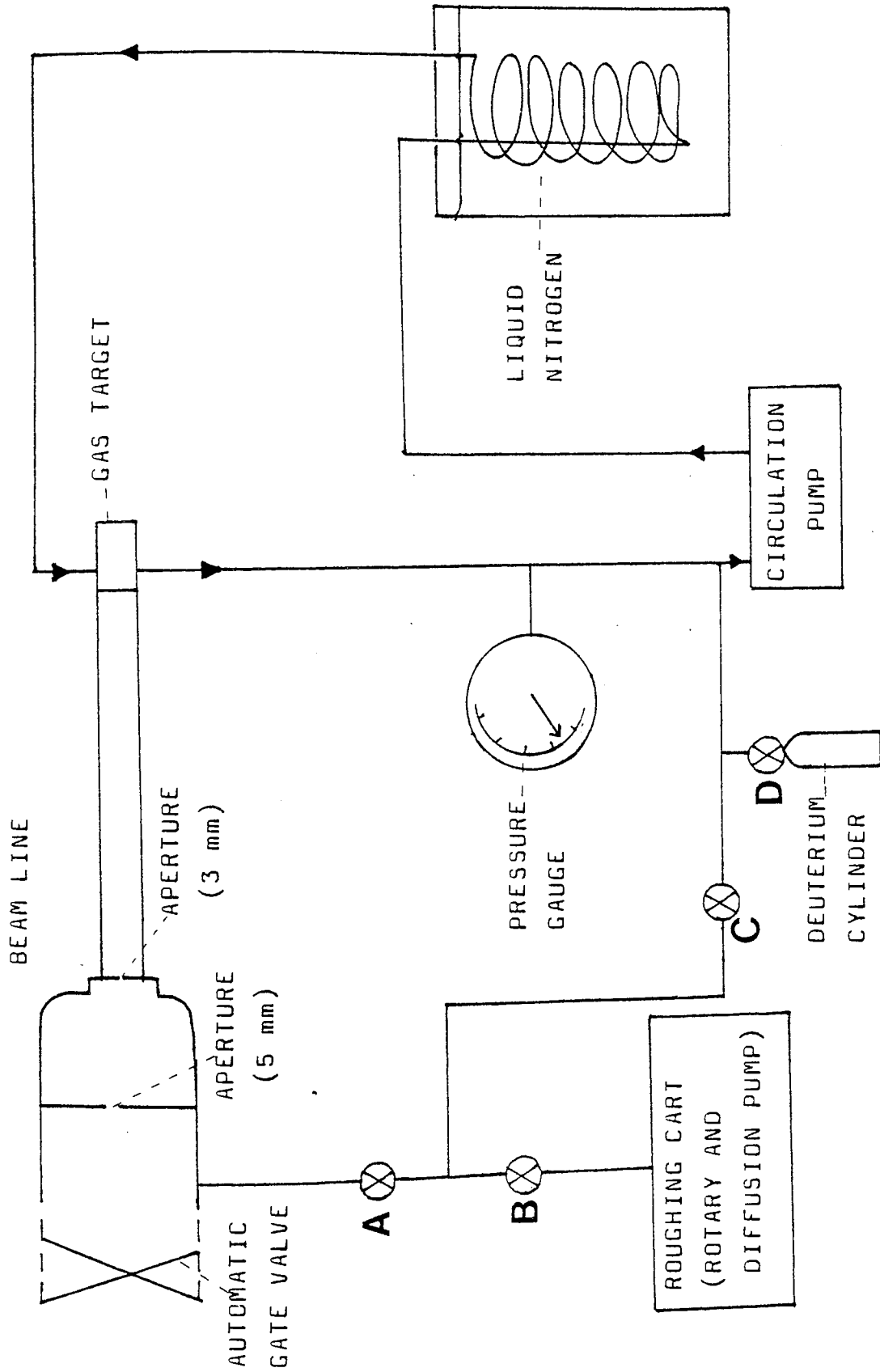
FIG. 6.6: THE GAS FILLING SYSTEM

the diffusion pump . This was necessary in order to
avoid the introduction of carbon from the vacuum
system , onto the target window during beam bombard-
ment . A liquid nitrogen trap further minimised the
introduction of hydrocarbons . The gas circulation
pump (fig. 6.7) consisted of a rubber diaphragm
oscillating at 11,200 r.p.m. . The diaphragm was
driven by a 190 watt , 2800 r.p.m. motor driving a
pulley . The rotational motion of the pulley is
converted into vertical translations in the diaphragm
through a cam shaft pivoted 0.1 cm off-centre from
the rotational axis of the drive shaft . A set of
bearings serves to reduce the frictional forces
induced , thus allowing the pump to operate at high
speeds .

Whilst the pumping speed S_p was calculated
to be 2.37 litres s^{-1} , the effective pumping speed ,
S_e , is reduced due to the conductance of the pipe-
work . The effective pumping speed , however , can
be determined from the relation /89/ :

$$S_e = \frac{CS_p}{C + S_p}$$

(6.3)

where C is the conductance of the pipe in litres
s^{-1} . For round , smooth bore pipes , the viscous
conductance of air at 20°C can be determined to
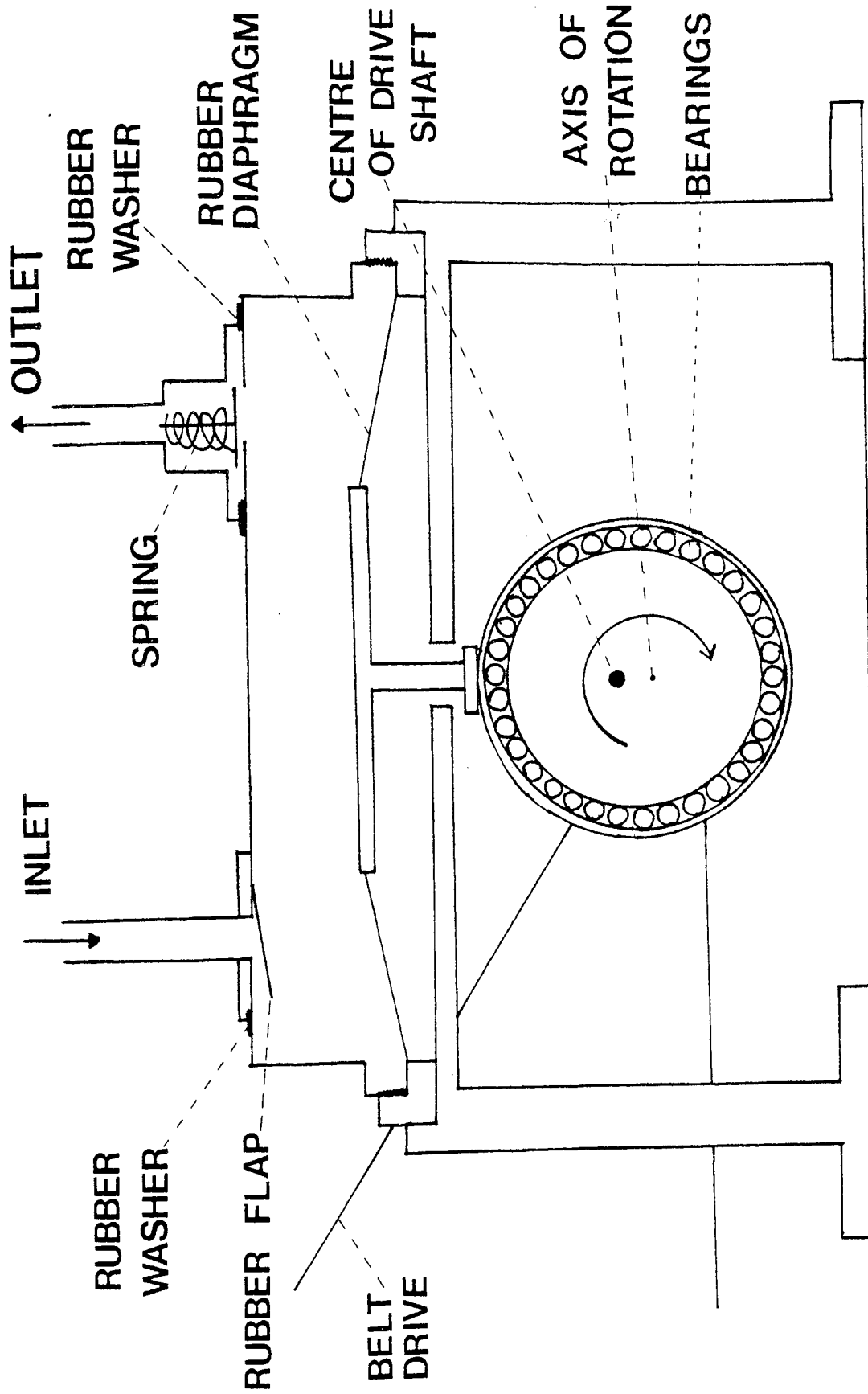
FIG. 6.7: THE HIGH SPEED PUMP

OUTLET

RUBBER WASHER

RUBBER DIAPHRAGM

CENTRE OF DRIVE SHAFT

AXIS OF ROTATION

BEARINGS

SPRING

INLET

RUBBER WASHER

RUBBER FLAP

BELT DRIVE

within 10% using the relation :

$$C = \frac{250 \ D^4 P}{L} \qquad (6.4)$$

where D is the internal diameter of the pipe , P the gas pressure and L the length of the pipe in centimetres . The use of deuterium instead of air in the pipe-work requires a correction factor of 2.07 to be applied to the conductance .*

Using equations (6.3) and (6.4) , for deuterium at a pressure of one atmosphere and a pipe bore of 0.2 cm and 3 metres long , the effective pumping speed was calculated to be 1.12 litres s^{-1} . However , this value does not take into account the reduction in pipe conductance resulting from the bends in the pipe .

Following from Langmuir /90/ , the factor by which heat removal from a vertical surface is increased through forced convection is given by :

$$\sqrt{(\ V + 35 \ )/35} \qquad (6.5)$$

where V is the gas velocity in centimetres per second . Using the calculated effective pumping speed of 1.12 l s^{-1} , heat removal from the front surface of the window is calculated to increase by a factor

*See Edwards Vacuum Catalogue , Crawley , Sussex .

of approximately 16 times .

Whilst a direct calculation of heat flow from the gas cell window would prove difficult , an estimate of the effectiveness of this method of cooling , and hence , the sufficiency of the pumping speed may be inferred as follows .

Ennis and Walton , through a private communication with Coon , op. cit. , calculate that at near maximum beam current , and for a 1.5 microns nickel foil , heat conduction is 85% through lateral conduction , 10% through conduction to the gas , and 5% through radiation . Although the window thickness used in the present work is twice that considered by Ennis and Walton , and therefore the energy dissipated in the window is double , the maximum beam current is set by the temperature at which the yield strength is just sufficient for the retention of gas pressure. Hence , the temperature of both foils at maximum beam current is approximately the same . Thus , given that lateral conduction is increased by a factor of 2 and conduction to the gas by a factor of 16 , the overall increase in heat removal increases by a factor of 2 . Pre-cooling of the deuterium gas provides a further improvement .

6.3 Gas Target Performance

Beam Current Characteristics

An assessment of the performance of the
cooling system was made by taking several foils to
destruction , with and without gas cooling . During
these tests an automatic gate valve was put into
operation as a precautionary measure against possible
failure of the accelerator vacuum system following
puncture of the window .

Beam currents were increased in steps of
0.1 micoramps and , at each current level , the
performance of the accelerator vacuum was observed
for periods lasting approximately 10 minutes . Without
the gas cooling system , one foil was observed to
fail at 1.1 microamps , whilst a second failed at
1.2 microamps . Failure was indicated through a
gradual rise in beam line pressure . With the cooling
system operating , a beam current of 2.6 microamps
was reached .

These tests were performed at deutron
energies of 2.8 Mev . At lower energies , the increase
in stopping power of the window requires the use of
lower beam currents . In considering the maximum
beam current at a given beam energy , a more impor-
tant parameter is power density . As a result of the
tests performed , the recommended beam power densities

for the nickel foil , with and without the cooling

system , are 7.1 watts cm^{-2} and 2.8 watts cm^{-2}

respectively . Whilst the maximum power density may

vary between foils having the same dimensions , the

values recommended allow for a margin of safety of

between 30% to 50% . In order to increase the

working life of foils , the beam current was increased

gradually . This provides an annealing effect , thus

improving the mechanical properties of the window .

At a beam current of 2.6 microamps and a

beam energy of 2.8 Mev , the use of a single tantalum

collimator before the gas cell , having a 3 mm

diameter aperture , results in 13 microamps (40 watts)

of beam current being deposited onto the collimator.

The use of two collimators , having apertures of

5 mm and 3 mm in diameter , serves to divide the

beam current between the two , whilst ensuring that

the beam strikes the target centrally .

Neutron Energy Profile

A knowledge of the neutron energy distri-

bution from the gas cell was required for this work.

The neutron spectrum and spatial distribution is

dependent upon several factors : (1) energy loss in

the nickel window and in the gas , (2) energy

broadening in the gas , (3) variation of energy and

intensity with angle of emission .

An ideal neutron energy distribution or
profile at a sample is preferably one which is
square . The ideal square profile , however , is
not normally achieved unless beam energy cycling is
employed /91/ . The energy distribution for the gas
target used has been reconstructed through a Monte
Carlo treatment of the gas target as an extended
line source .

The Monte Carlo program NPROFILE is
described in detail in Appendix 2 and , hence , only
a brief discussion is entered upon here .

For a given input of beam energy , the
program determines the position at which a neutron
is created in the target . This provides the
corresponding deutron energy following energy losses
in the window and gas . The neutron emission at a
given angle is weighted by using the differential
cross-section data of Liskien et al /92/ . From the
position co-ordinates of the point of creation , the
polar co-ordinates for direction of emission and the
source-sample distance , the program determines
whether a hit on the sample is scored . An energy
profile at the sample is obtained from following a
large number of histories .

Given the small neutron source-sample

distances employed in this work (2.0 to 2.5 cm) ,
the combination of energy degradation in the gas
and the source-sample configuration results in an
asymmetric neutron energy distribution at the
sample .

Calculated spectra at deutron beam energies
of 3.0 Mev and 1.0 Mev respectively are presented
in fig . 6.8 .

The neutron spectrum from the target is
degraded also by beam energy straggling . However ,
this contribution is small /93/ , and , due to its
statistical nature, it has a Gaussian distribution
and would contribute equally to each end of the
profile . Hence , its contribution to the mean
energy can be neglected .
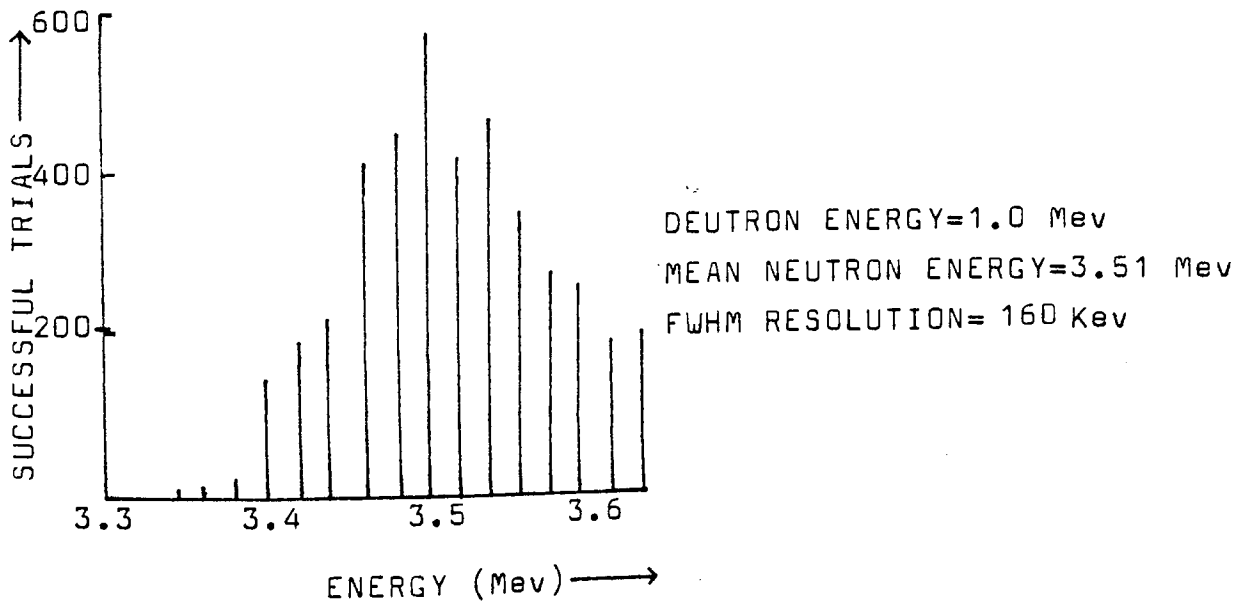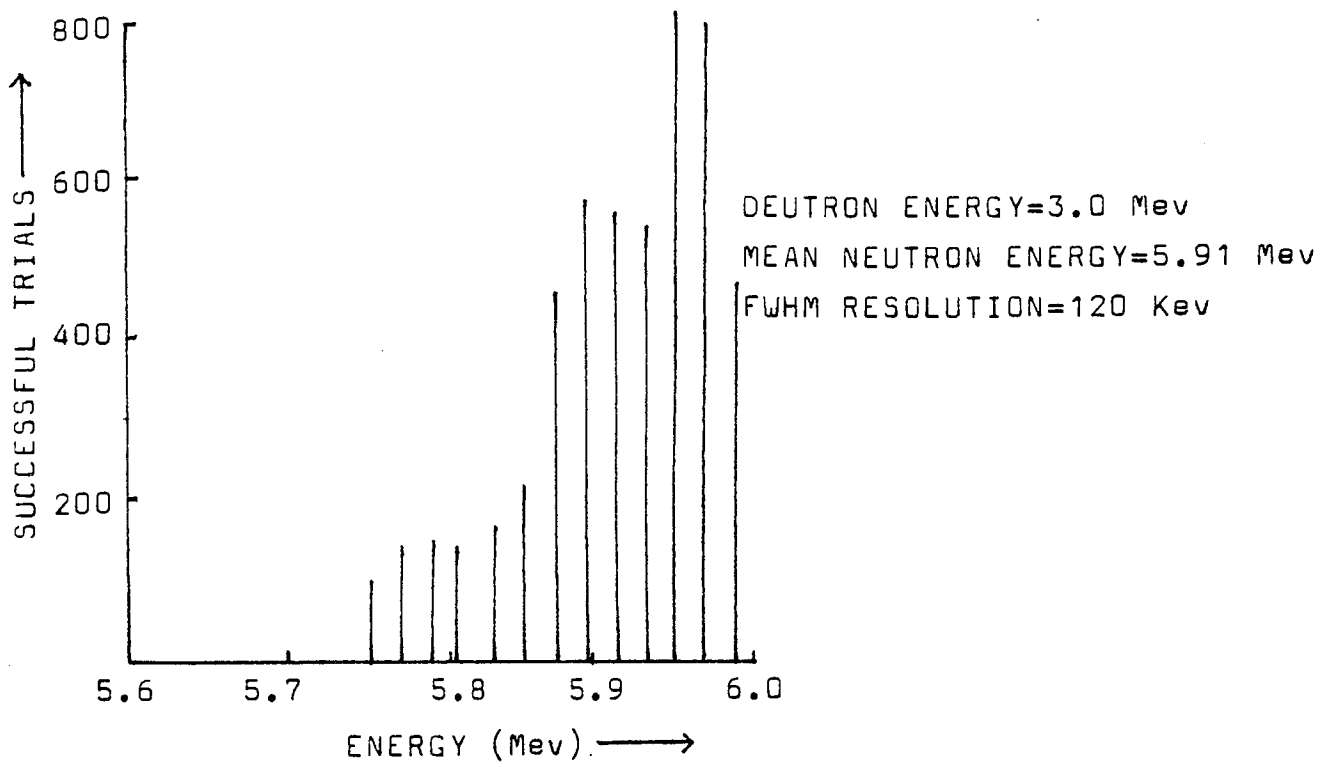
FIG.6.8: NEUTRON SPECTRUM AT SAMPLE AS
DETERMINED FROM MONTE CARLO CALCULATION

CHAPTER 7
MEASUREMENT OF IRRADIATED SAMPLE ACTIVITY

CHAPTER 7

Measurement of irradiated sample activity

Measurements of gamma-ray activities from the Ti(n, p) reaction products ^{46}Sc , ^{47}Sc and ^{48}Sc were made using a 7.62 cm x 7.62 cm NaI (Tl) scintillation detector . The use of a NaI scintillator, in preference to a Ge(Li) detector , was influenced by the anticipated low gamma-ray activities in ^{46}Sc and ^{48}Sc . Although energy resolutions in Ge(Li) detectors are superior , the 7.5% energy resolution of the NaI(Tl) detector was found adequate , and provided the advantage of greater detection efficiency.

The decay schemes of ^{46}Sc , ^{47}Sc and ^{48}Sc are presented in Table 7.1 .

Table 7.1 : Decay schemes of ^{46}Sc , ^{47}Sc and ^{48}Sc

	Gamma-ray Energy(Mev)	Half-life	Branching Ratio
^{46}Sc	0.887	83.8 days	1
	1.12		1
^{47}Sc	0.159	3.4 days	0.685
^{48}Sc	0.983		1
	1.037	43.8 hours	0.98
	1.31		1

It is apparent that whilst there is overlap between the 1.12 Mev and 0.89 Mev gamma-rays from ^{46}Sc and

the 0.983 Mev and 1.037 Mev gamma-rays from ^{48}Sc ,

the difference in half-lives of the two isotopes

allows analysis of the ^{46}Sc activity following the

decay of ^{48}Sc .

Natural titanium samples of 99.99% purity

were irradiated as described earlier (Section 1.5),

with typical neutron exposures of 10 to 12 hours .

The methods employed in the analysis of the gamma-

ray spectra and the determination of their respective

activities are described in the following sections .

7.1 Gamma-ray spectrometry with NaI scintillators

In the NaI(Tl) detector , the response to

a monoenergetic gamma-ray of energy around 1 Mev is

characterised by a Compton continuum and a single ,

approximately Gaussian peak . The pulse height and

intensity of this peak is a measure of the energy

and intensity of the incident gamma-rays .

However , the response of NaI detectors is

not unique in that the shape and magnitude of the

observed pulse height spectrum is not solely dependent

upon the energy of the gamma-ray and the source-

detector configuration , but is also dependent upon

the experimental environment . Whilst an excellent

account of this response is presented by Heath /97/,

its importance in relation to the reproducibility

of measurements and to the analysis of data requires brief discussion .

Under non-ideal experimental conditions , extraneous contributions appear in the measured spectrum which are not representative of the detector response to gamma-radiation incident directly on the detector . A small backscatter peak is generally evident on the Compton distribution , resulting from gamma-rays which are Compton scattered from the surrounding materials in the detector shield , air , source and source mounting . This extraneous contribution to the total counts could be a source of error in measurement of the gamma activity of a sample . Further , extrapolation of the spectrum to zero pulse height is often difficult , due to the preponderence of background radiation and the photo-multiplier tube dark current .

In consequence , such measurements are generally made in conjunction with background suppression techniques , such as $\gamma - \gamma$ and $\beta - \gamma$ coincidence counting . In the presence of several gamma-rays from an activated sample , experimental spectra are complex ,and hence , the total number of counts in the full energy gamma-ray peak provides a better quantity for activity measurements .

In the region above the photopeak , and at high count rates , a continous distribution of pulses

extending up to twice the amplitude of the full

energy peak is evident . This contribution results

from the pile-up of detector pulses through random

time-coincidence between pulses , and is dependent

upon the count rate N , and the resolving time τ ,

of the system. The pulse pile-up rate(Heath,op.cit.)

is given by the relationship :

$$I_{rss} = 2N^2\tau \qquad (7.1)$$

Thus , at high count rates , significant counts are

lost from the full energy peak and Compton spectrum.

In measurements involving the emission of

multiple gamma-ray cascades , additional peaks are

evident in the pulse height spectrum . Where no

isomeric states are involved , the lifetime of an

intermediate state of a nucleus is short-lived ,

which results in the emission of two or more gamma-

ray photons in virtual coincidence . Where the angle

of emission between the emitted cascade photons is

less than that subtended by the detector at the source

and where both incident photons interact in the

detector , a sum-coincidence spectrum corresponding

to their combined energies is observed . Thus ,

whilst the time-coincidence spectrum is count rate

-dependent , the sum-coincidence spectrum from gamma-

ray cascades is solid angle dependent .

To reduce counting losses from this latter effect , a low geometry counting configuration is desirable . However , where the low activity of a sample is the limiting factor , sum-coincidence losses can be corrected for . These corrections will be described in Section 7.3.3 .

7.2 Analysis of gamma-ray spectra

It is evident from the preceeding discussion that a sample containing several gamma-active nuclides exhibiting complex decay schemes will produce complex gamma-ray spectra . Unless the corresponding full-energy peaks are resolved , accurate quantitative measurements are not possible . In such instances , spectrum stripping or unfolding methods can be employed , currently through computer methods /97-99/.

In the analysis of spectra where the full-energy peaks are resolved , several methods of quantifying the full-energy peak area are available. These methods can be divided into two groups : those which determine the peak area through direct summation of the digital data /100,101/ and those which obtain the area from a fitted analytic function /102-106/. In either approach , the background upon which the peak is superimposed must be subtracted . Direct

background subtraction is not always possible ,
however , where a peak of interest is superimposed
upon a Compton continuum . Where this is so , the
data on the channels on either side of the peak can
be used to define the continuum . A linear or
quadratic curve is used to provide an estimate of the
continuum in the region of interest . In the present
work , the analytic approach has been adopted .

Typical gamma-ray spectra obtained are
presented in Figs. 7.1 to 7.3 . The spectrum shown
in Fig.7.1 is that obtained immediately following
irradiation . In this spectrum , the full-energy peaks
from ^{46}Sc and the 0.98 Mev and 1.04 Mev full-energy
peaks of ^{48}Sc are not resolved . Nevertheless , the
1.31 Mev full-energy peak of ^{48}Sc and the 0.159 Mev
full-energy peak of ^{47}Sc are clearly resolved and
can be analysed using the methods to be described in
Section 7.2.1 .

The spectrum shown in Fig.7.2 corresponds
to that shown in Fig.7.1 , but obtained at a lower
amplifier gain . Three distinct sum-coincidence
peaks are visible . The first is a composite of the
^{46}Sc(0.89 + 1.12)Mev sum-coincidence peak and the
^{48}Sc(0.99 + 1.04)Mev sum-coincidence peak . The second
is due to the (0.99 or 1.04 + 1.31)Mev sum-coincidence
peaks of ^{48}Sc , whilst the third is the triple sum-
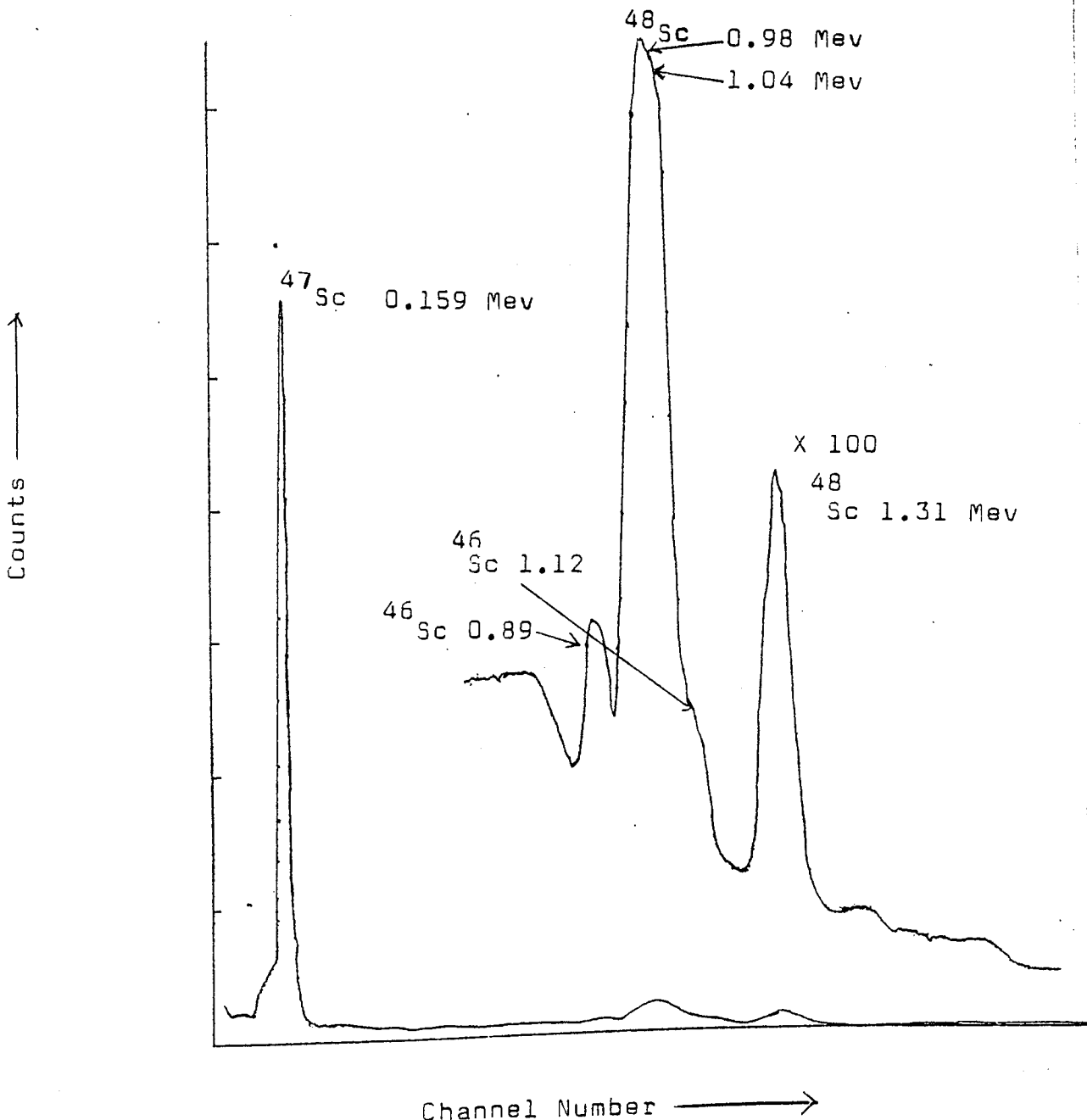
Fig. 7.1 GAMMA-RAY SPECTRUM FROM SCANDIUM
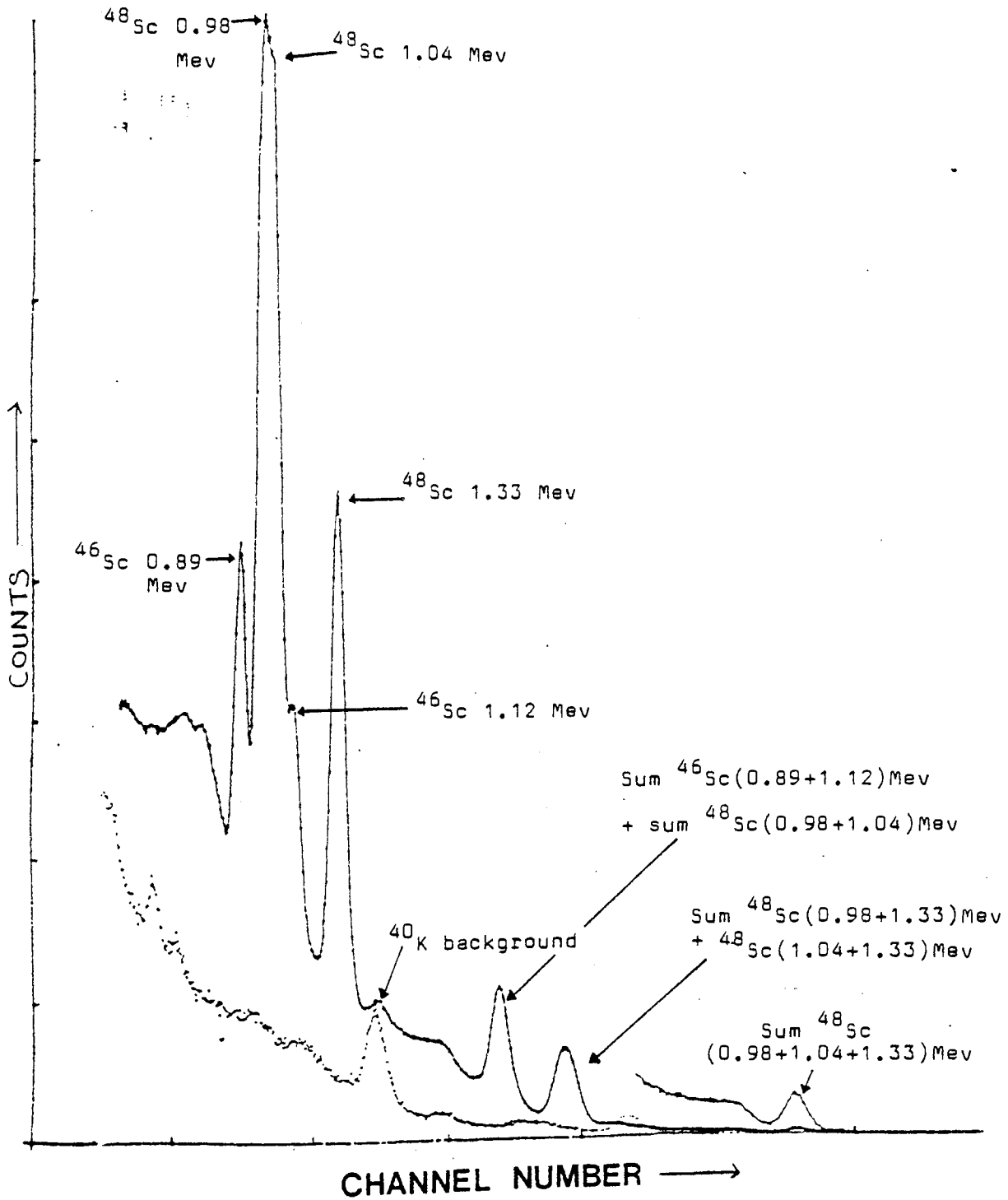
FIG. 7.2 : GAMMA-RAY SPECTRUM FROM SCANDIUM .
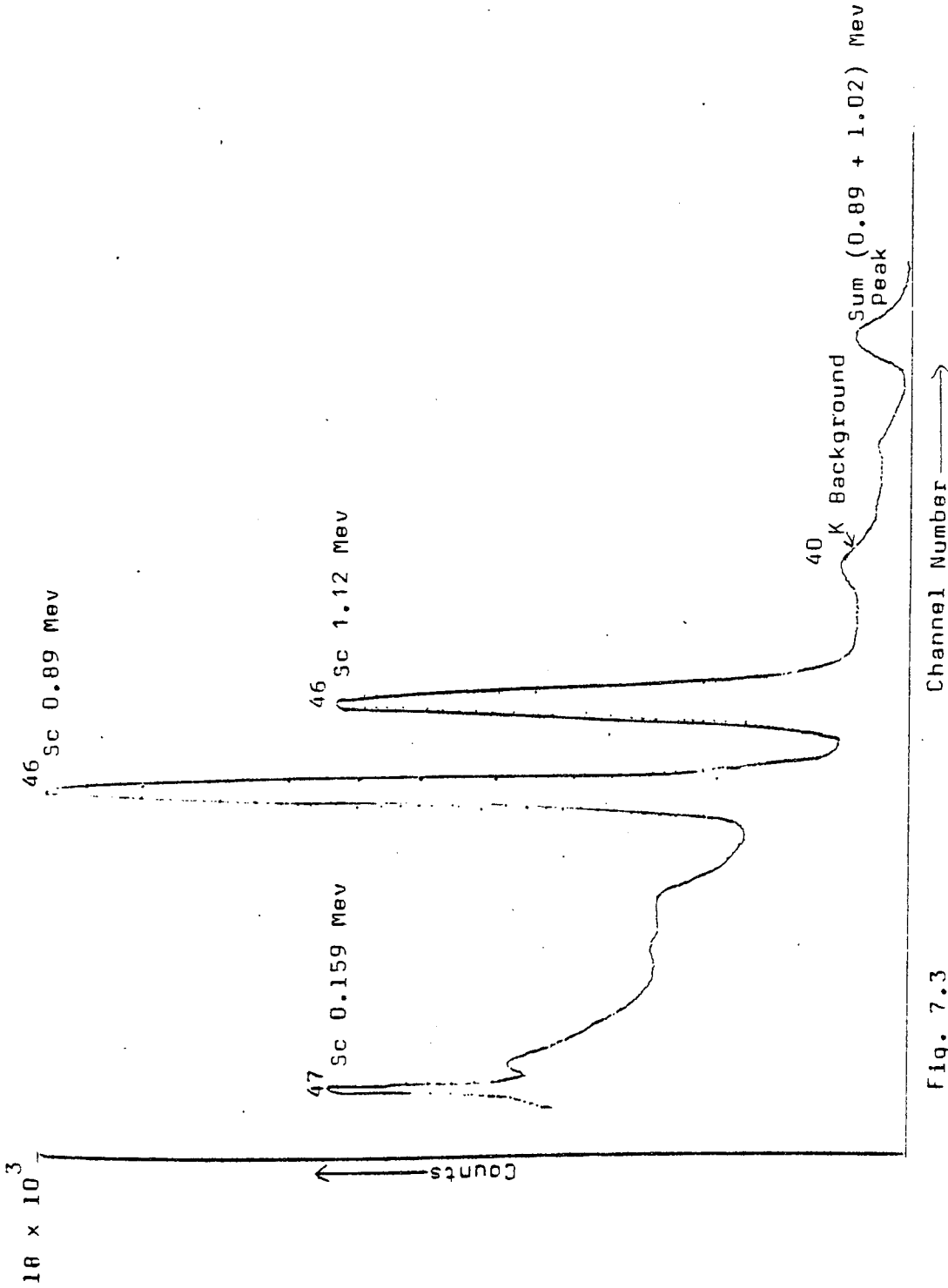
Fig. 7.3

GAMMA-RAY SPECTRUM THREE WEEKS FOLLOWING IRRADIATION

coincidence peak of ^{48}Sc . The background spectrum
has been included in Fig .7.2 and shows a peak
identified as that of ^{40}K , a component of the
background gamma radiation .

The spectrum shown in Fig .7.3 is that of
^{46}Sc with both the 0.89Mev and the 1.12 Mev full-
energy peaks resolved . This spectrum was obtained
three weeks after irradiation , when the ^{48}Sc
activity had decayed completely but when some ^{47}Sc
activity remained .

A description of the methods applied in the
analysis of these spectra follows .

7.2.1 Full-energy peak area analysis

In instances where the complicating effects
of background continuum and peak tails are not
significant or can be subtracted , the full-energy
peak can be adequately expressed as a Gaussian of the
form :

$$y(x) = y_0 \exp(-(x-p)^2/2\sigma^2) \qquad\qquad (7.2)$$

where y_0 is the peak amplitude , x the channel
number , p the peak centre position and σ the peak
standard deviation .

A small deviation from the Gaussian function,
however , is generally evident at the low energy wing

of a peak , for which a modified Gaussian function
is proposed by Heath et al /99/ and is of the form:

$$y(x) = y_0 \left[1 + \alpha_1 (x-p)^4 + \alpha_2 (x-p)^{12} \right] \exp(-(x-p)^2 / 2\sigma^2) \quad (7.3)$$

where α_1 and α_2 are coefficients of the polynomial .

Either function can be fitted to an experi-
mental peak using the method of least squares such
that the weighted sum of the squares , χ^2, is minimised.

$$\chi^2 = \sum_{i=1}^{N} w_i \left[Y_i - y(x_i) \right]^2 \quad (7.4)$$

where Y_i are the experimental counts in channel i ,
w_i the associated weight , $Y(x_i)$ the fitted function,
and N is the number of channels over which the fitting
is performed .

The procedure for minimisation of χ^2 requires
that the set of equations of the partial derivative
of χ^2 with respect to the parameters p , σ, α_1 and α_2
is linear in those parameters . Unfortunately , these
conditions are not observed and no solution exists
unless a linearisation procedure is applied . These
procedures require iterative methods as described
by Helmer et al /106/ .

A simpler non-iterative method which can
be applied to the Gaussian function in equation 7.2

has been reported recently by Mukoyama /107/ . This method has been applied to the analysis of the gamma-ray data .

The Method

Given the Gaussian function of equation 7.2, a function $Q(x)$ can be defined as the ratio of y as a function of $(x-1)$ to that of y as a function of $(x+1)$. Thus :

$$Q(x) = \frac{y(x-1)}{y(x+1)} = \exp\left[2(x-p)/\sigma^2\right] \qquad (7.5)$$

and :

$$\ln Q(x) = 2(x-p)/\sigma^2 \qquad (7.6)$$

Hence , a linear function of x is obtained , to which a linear least-squares fit can be applied . The peak position p and the standard deviation σ in the peak can now be represented as :

$$\sigma = \sqrt{\frac{2}{m}} \qquad \text{and} \quad p = \frac{-b}{m} \qquad (7.7)$$

where m and b are the least-squares fit gradient and intercept of equation (7.6) . The weighting factor w_i associated with the counts in channel i is

selected to vary inversely with the statistical
variance of the counts in that channel , such
that :

$$W_i = \left[\frac{1}{Y_i + 1} + \frac{1}{Y_i - 1}\right]^{-1} \qquad (7.8)$$

Once the parameters σ and p are obtained,
the peak height y_o can be determined from the fitted
data using a weighted mean from the data points used.
The expression for peak height is :

$$\ln y_o = \frac{\sum_{i=1}^{N} W_i \left[\ln Y_i + (x_i - p)^2 / 2\sigma^2\right]}{\sum_{i=1}^{N} W_i} \qquad (7.9)$$

where W_i is expressed as :

$$W_i = \left[\frac{1}{Y_i} + \frac{(x_i - p)^2}{\sigma^4}\left\{(\Delta p)^2 + \frac{(x_i - p)^2}{\sigma^2}(\Delta\sigma)^2\right\}\right]^{-1} \qquad (7.10)$$

and Δp and $\Delta\sigma$ are the standard deviations of p and σ
from the linear fit .

The total peak area A is given by :

$$A = 2.507\sigma y_o \qquad (7.11)$$

A computer program"PEAKFIT" was written for
use on a 2001 series Commodore PET computer (see

Appendix 3) . The program requires as input the
number of data points to be fitted and the correspon-
ding experimental data, x_i , y_i , and computes the
peak position , its standard deviation , peak height
and peak area . Data is input only for those points
above the full-width at half maximum of the peak .
This serves to overcome the uncertainty associated
with the data in the wings of the peak , and provides
a better fit ./105/. Lastly , the fitted Gaussian
function serves to smooth out statistical variations
in the experimental data .

Prior to input of the experimental data ,
the background contribution in the region of interest
must be determined and subtracted from the counts in
each channel . Whilst the contribution from background
radiation can be subtracted directly , the resultant
spectrum is superimposed on the continuum of sum-
coincidence spectra . Provided that the continuum
in the region under the peak does not exhibit marked
variation , an accurate representation of tbe continuum
can be derived through the fitting of a third order
polynomial of the form :

$$y(x_1) = a_o + a_1 x + a_2 x^2 + a_3 x^3 \qquad (7.12)$$

The fitting is performed using data to the right of

the peak of interest through the usual method of linear least squares . Then , the fitted function is extrapolated to include the region under the peak of interest and subtracted from the experimental data. For the 0.159 Mev peak of ^{47}Sc , the 1.12 Mev peak of ^{46}Sc and the 1.31 Mev peak of ^{48}Sc , a linear fit was found sufficient , the higher order coefficients being negligibly small . However , the 0.89 Mev ^{46}Sc peak is superimposed upon the 0.93 Mev Compton edge of the 1.12 Mev ^{46}Sc peak , and the background subtraction is subject to some error . For the 0.89 Mev ^{46}Sc peak , the fitting was obtained using data on both wings of the peak and a third order polynomial applied . Fortunately , in the ^{46}Sc(n, p) cross - section computation , the 0.89 Mev ^{46}Sc peak is used only to provide an approximate check on the value obtained from the 1.12 Mev peak .

The adequacy of the methods used in the analysis of the full energy peak is demonstrated in Figs . 7.4 and 7.5 , where the overlap between the low energy wing of a peak with its corresponding Compton edge can be resolved .

7.3 Activity of the irradiated samples

7.3.1 Full Energy Peak Efficiency

To determine the total activity of an irradiated sample , a knowledge of the detection
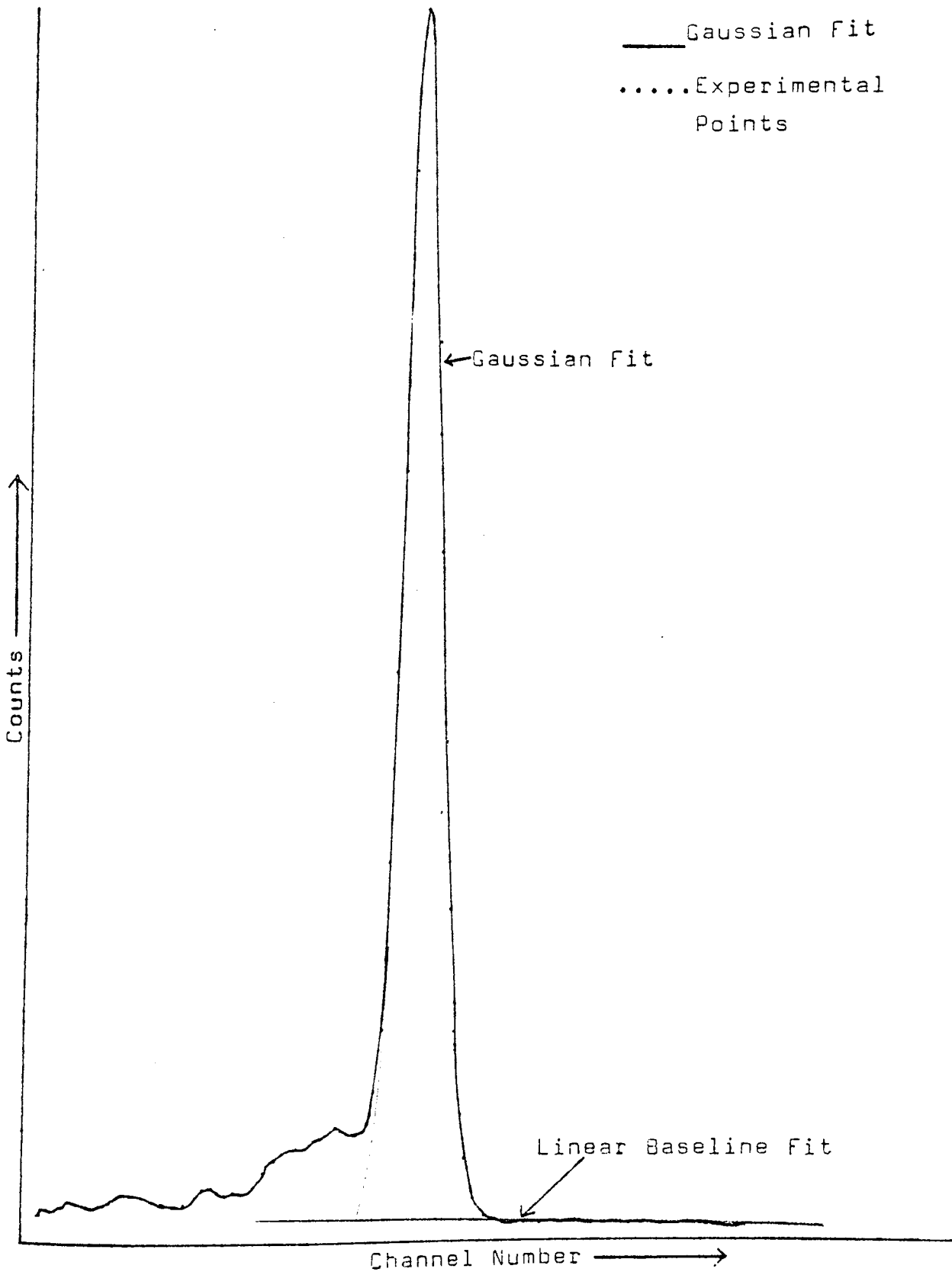
Fig. 7.4 :
COMPUTER FIT TO THE SCANDIUM-47 FULL-ENERGY PEAK .
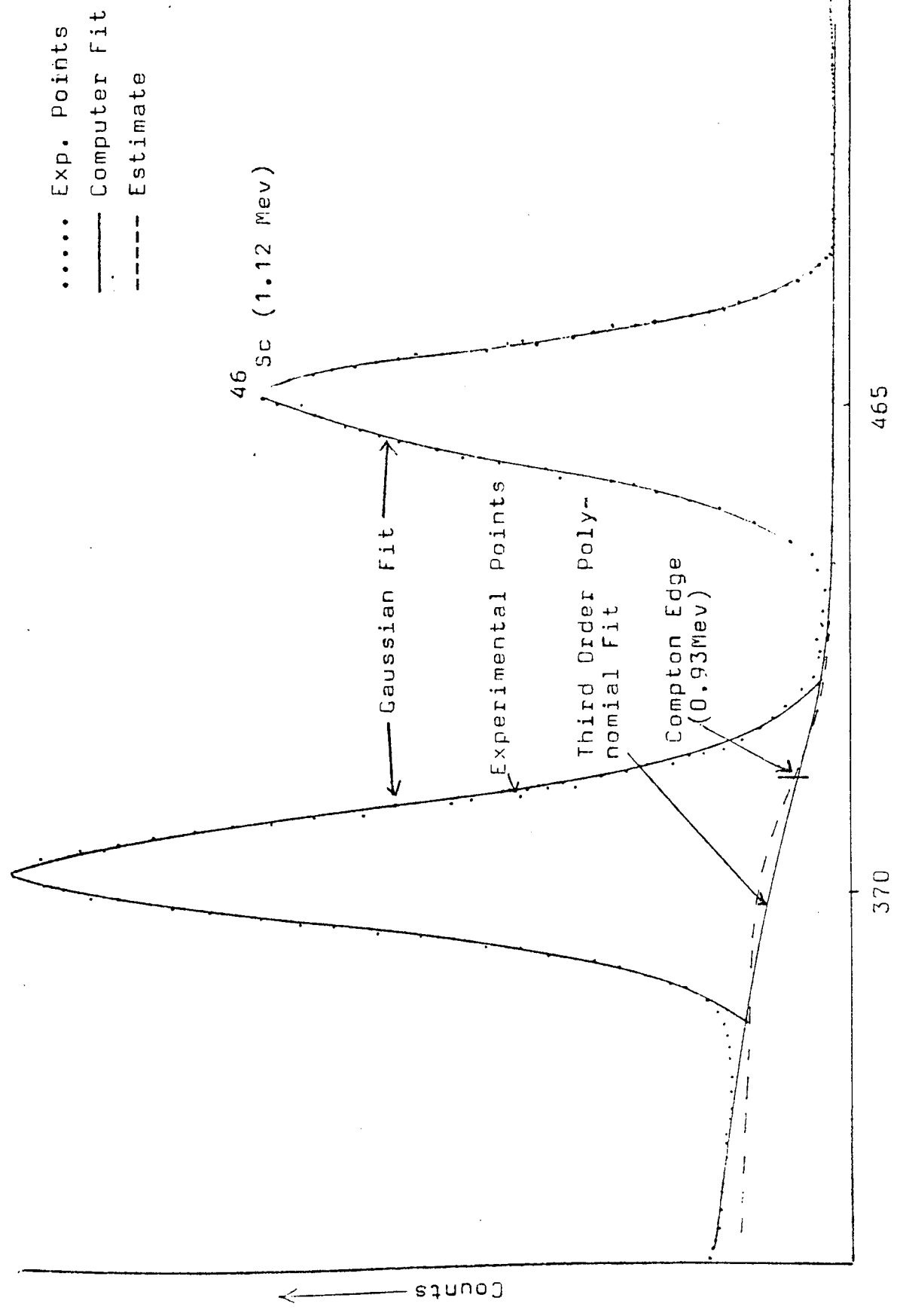
Fig. 7.5 : COMPUTER FIT TO THE SCANDIUM-46 PEAK .

efficiency of the γ-ray spectrometer is required.
The absolute detection efficiency, ε_T, is defined
as the ratio of the total number of gamma-rays
interacting in the crystal to that of the total
number emitted in the sample. Under ideal experimental
conditions, where a source and detector can be
isolated from their surroundings, the total area
under the resultant pulse height spectrum divided by
the detector efficiency would provide the total activity
of the source. In practice, as described in Section
7.1, the pulse height spectrum contains additional
counts from gamma-rays scattered in the vicinity of
the detector. However, the full energy peak repre-
sents a true measure of the activity since these
additional counts do not appear in the full-energy
peak due to the energy degradation accompanying the
scattering process. Thus, a further quantity, the
full energy peak efficiency, ε_p, can be defined as
the total number of interactions appearing in the
full energy peak to the total number emitted by the
source, such that :

$$\varepsilon_p = P \varepsilon_T \qquad (7.13)$$

where P represents the ratio of the full energy peak
to the area of the full spectrum in the absence of

extraneous counts .

For given source-detector configurations ,
detection efficiencies can be derived either experi-
mentally or by calculation . The simplest experimental
approach requires the availability of a set of
accurately calibrated standards . The absolute activities
of such standard sources are known to better than 1%.
The detection efficiencies can then be determined
from the observed activity in the detector and am
experimental efficiency curve produced covering the
energy range of interest .

Where such standards are not available or
do not accurately represent the experimental config-
uration , detection efficiencies can be calculated
analytically . The quantity ε_T , defined earlier as
the absolute detection efficiency , can be expressed
mathematically as the integral of $(1-\exp(-\mu_T l)$
over all path lengths l in the detector and over the
corresponding solid angle , where μ_T is the total
absorption cross-section.

The most extensive set of tables for
absolute detection efficiency to date are provided
for by Grosjean/108/ . These tables cover a wide range
of scintillator crystal dimensions and source config-
urations , including point , line , plane rectangular
and disc sources . From these tables , the corresponding

detection efficiencies for disc sources of any diameter could be obtained . Furthermore , where the data for any given source-detector distance and energy is not included , Grosjean suggests the use of Lagrangian interpolation for which the required efficiency can be computed to an accuracy of up to 4 decimal figures .

In this work , the titanium disc samples were placed centrally on the NaI(Tl) detector casing. The distance between the crystal surface and the front face of its aluminium casing was measured using a method described by McElroy /109/ . This distance , l , is found from the relationship :

$$l = \frac{d_1 \sqrt{A_1} - d_2 \sqrt{A_2}}{\sqrt{A_2} - \sqrt{A_1}} \qquad (7.14)$$

where A_1 and A_2 are the count rates measured at two source to outer casing distances d_1 and d_2 . Equation 7.14 is applicable where the inverse square distance law applies , which is generally true for point sources at $d > 9.0$ cm . Hence a ^{137}Cs point source was placed at d=10.0 cm , 11.0 cm and 12.0 cm , and the corresponding activities measured . In this instance, for reproducibility , the total counts in the 10 channels below and above the centre of the peak were

used as a relative measure for activity (Covell/110/).

The values obtained for l were found consistent to within 2% with a mean value of 4.25 mm.

Whilst the absolute detection efficiencies calculated by Grosjean relate to plane disc sources , the titanium samples used in this work were 2 mm thick, 4.25 mm from the front face of the scintillator crystal. The corresponding absolute detection efficiencies were determined as follows . The absolute detection efficiencies determined from the data of Grosjean for plane disc sources at source-detector distances ranging from zero to 1.0 cm , were plotted as a function of source-detector distance . The average absolute detection efficiency was determined from the area under the curve corresponding to source-detector distances of 0.425 cm to 0.625 cm . However , a further correction has to be applied for sample self-absorption and self-scattering . This is described in Section 7.2.2 .

The peak to total ratio P , or photofraction, cannot be readily determined through analytic methods, due to the multiple nature of the process . Hence , Monte Carlo methods are relied upon /112-115/ . Extensive data from experimental measurements is also available /116-119/ , but are limited to accuracies of no better than 2% , with calculated values being

systematically greater than the experimental values .
The discrepancy between these values increases with
energy and is significant above 2.0 Mev .

It is generally accepted that both Monte
Carlo and experimental methods for photofraction
determination suffer drawbacks . Whilst Monte Carlo
methods have the advantage of simulating ideal
experimental conditions , inherent errors in the
treatment of secondary particle transport are present[*].
In the experiments conducted by Heath /111/ , measure-
ments were made with the source and detector placed
in a plastic bag containing helium gas in a large
open room to minimise scattering . In the Monte Carlo
calculation of Snyder /126/ , where a more sophisti-
cated model for secondary particle transport was used,
there was good agreement with the results of Heath .

Although there have been several recent
experimental measurements of peak to total ratios ,
most authors refer their measurements to those of
Heath for comparison . Hence , the peak to total
ratios of Heath have been used in the calculation of
full energy peak efficiency in the present work .

[*]

The accuracy is limited by the knowledge of the reactions
occuring .

Table 7.2 : Absolute detection efficiencies , peak
to total ratios and the full energy
peak efficiencies (Grosjean, op. cit &
Heath, op. cit.)

	Energy (Mev)	Peak/Total	Absolute Efficiency	Full energy peak efficiency
^{46}Sc	0.89	0.440	0.2366	0.1041
	1.12	0.385	0.2252	0.0867
^{47}Sc	0.159	0.960	0.4290	0.4118
	0.98	0.415	0.2298	0.0954
^{48}Sc	1.037	0.40	0.2276	0.0910
	1.31	0.345	0.2212	0.0763

7.3.2 Sample self-scattering and self-absorption

The finite dimensions of the 20 mm diameter
by 2 mm thick titanium samples used in this work
necessitates a correction for self-scattering and
self-absorption in the samples . Counts are lost from
the full-energy peak through interaction of the
emitted gamma-rays within the sample through either
the photoelectric process or Compton scattering .
Whilst the photoelectric process results in total
absorption of the emitted gamma-rays , Compton scattering
results in either a "scatter in" to the detector or
a "scatter out" from the detector . Although the
scattered gamma-rays may interact subsequently within

the detector , they will not contribute to the full-
energy peak as a result of energy lost in the scattering
process .

Since only the counts in the full-energy peak
are required , all gamma-rays interacting within the
sample can be regarded as lost . Hence , the fraction
of events lost to the full-energy peak can be repre-
sented as the integral of $(1-e^{-\mu_T l})$ over all path
lengths l in the sample . The quantity μ_T is the
total linear absorption coefficient . The wide distri-
bution of gamma-ray path lengths in the sample ,
however , renders an analytic approach to the solution
of this integral prohibitively difficult . A simpler
approach is to use a Monte Carlo method .

The fraction of gamma-rays leaving the sample
without loss of energy may be expressed as :

$$T_f = 1/N_{hist} \sum_{J=1}^{N_{hist}} ExP(-\mu_T l) \qquad (7.15)$$

where N_{hist} is the total number of histories used in
the Monte Carlo program . A program GAMMA (see
Appendix 4) has been written and used to perform
this calculation to an accuracy of 1% , using the
linear attenuation coefficient data of Storm et al
/120/. The program was also used to calculate the

fraction of all gamma-rays , T_a , which succeed in leaving the sample . The photoelectric absorption coefficient , μ_p , replaces μ_T in equation 7.15 , since multiple Compton scattering events leading to total energy loss in the sample is assumed to be negligible . With the exception of the 0.159 Mev gamma-ray from ^{47}Sc , this is a good approximation , since only 6% of the gamma-rays scatter more than once within the sample . For larger sample dimensions, multiple scattering is significant and a more sophisticated Monte Carlo program /113/ is required .

The results following from these calculations are tabulated in Table 7.3 .

Table 7.3 : Absorption corrections listed as transmission factors

	Energy (Mev)	T_f	T_a
^{46}Sc	0.891	0.719	0.9978
	1.12	0.743	0.9987
^{47}Sc	0.159	0.593	0.7779
	0.98	0.728	0.9983
^{48}Sc	1.037	0.735	0.9985
	1.31	0.749	0.9991

Using the data from Table 7.3 , the detection efficiencies listed in Table 7.2 can be

corrected to account for sample self-absorption .
The corrected efficiencies are listed in Table 7.4
and represent the detection efficiencies for a
titanium disc source of 20 mm diameter , 2 mm thick,
and 4.25 mm from the front face of the detector
crystal .

Table 7.4 : Corrected detection efficiencies

	Energy (Mev)	Full-energy peak efficiency (ε_p)	Absolute detection efficiency (ε_T)
^{46}Sc	0.89	0.07485	0.2361
	1.12	0.0644	0.2249
^{47}Sc	0.159	0.2442	0.3337*
	0.98	0.06945	0.2294
^{48}Sc	1.037	0.06689	0.22726
	1.31	0.05715	0.2210

* Approximate

Although the corrected absolute detection
efficiency quoted for ^{47}Sc is only approximate , only
the full-energy peak efficiency , ε_p, is required in
determining the activity of ^{47}Sc , and this is known
to 2% accuracy . The accuracies of the other detection
efficiencies listed are 2% and 1% for ε_p and ε_T
respectively .

A further correction for sum-coincidence
losses is required for ^{46}Sc and ^{48}Sc measurements .

These corrections are described in the following section .

7.3.3 Sum-coincidence corrections

Where the decay scheme of a nuclide results in the simultaneous emission of two cascade gamma-rays, the intensity of the observed sum-coincidence spectrum is given by :

$$N_{12} = S\varepsilon_{T1} \ y_1 \ \varepsilon_{T2} \ y_2 \ W_{12}(0^O) \tag{7.16}$$

where S is the decay rate of the nuclide , y_1 and y_2 the branching ratios and $W_{12}(0^O)$ the angular correction function , where 0° refers to the fact that the two gamma-rays are incident upon the same detector . ε_{T1} and ε_{T2} are the absolute detection efficiencies for the two gamma-rays .

Theoretical angular correlation functions have been listed for a variety of solutions by Rose /121/ and West /122/ . $W(0^O)$ can also be determined experimentally /123/ with two detectors placed equidistantly from the source; the observed variation in coincident counts with the angle between the two detectors , Θ, provides the angular correlation function .

The usual convention is to normalise the

angular correlation function such that :

$$\int W(\theta) \, d\Omega = 1 \qquad (7.17)$$

where $W(\theta) = 1 + a_2 \cos^2\theta + a_4 \cos^4\theta + \ldots\ldots (7.18)$

At $= 180°$, $W(\theta)$ is at a maximum , whilst at $\theta=90°$, it is at a minimum . From equation (7.17), in 2π geometry , $\Omega W_{12}(\theta)$ is 0.5 , whilst in 4π geometry , it is 1 .

The effect of coincidence events in a detector is to remove counts from the spectrum of interest . In the case of ^{46}Sc , where two cascade photons γ_1 and γ_2 are present , since there are losses to both the sum-coincidence spectrum and the full-energy sum peak , the number of remaining full energy events associated with γ_1 can be written as:

$$N_{p1} = S \, \varepsilon_{p1} \, y_1 (1 - \varepsilon_{T2} \, y_2 W(0°)_{12}) \qquad (7.19)$$

where the subscripts 1 and 2 refer to the 0.89 Mev and 1.12 Mev gamma-rays , respectively .

· The full energy sum-coincidence events can be written as :

$$N_{p12} = S \, \varepsilon_{p1} \, \varepsilon_{p2} \, y_1 y_2 W(0°)_{12} \qquad (7.20)$$

Although the angular correction factor is not known for the source detector configuration used in this work , an effective value can be determined from the ratio of the sum-coincidence peak , N_{p12}, to the full energy peak of either γ_1 or γ_2 . Using relations (7.19) and (7.20) , this ratio is represented as :

$$R = \frac{N_{p12}}{N_{p1}} = \frac{y_2 \, \varepsilon_{p2} W(0^o)_{12}}{(1 - \varepsilon_{T2} y_2 W(0^o)_{12})} \tag{7.21}$$

Hence ,

$$W(0^o)_{12} = \frac{R}{(y_2 \, \varepsilon_{p2} + R \, \varepsilon_{T2} y_2)} \tag{7.22}$$

The angular correlation factor obtained in equation (7.22) is referred to as "effective" due to the fact that $W(0^o)$, in this instance , is obtained from an extended source configuration and therefore does not correspond to the actual angular correlation function of ^{46}Sc nuclei .

For ^{46}Sc , the ratio R has been determined from the 2.01 Mev sum-coincidence peak and the 1.12 Mev peak and a value of 1.14 for $W(0^o)$ is obtained . Since the value of Ω for the experimental configuration is

approximately 0.4 , this value corresponds closely to the value of 0.5 for $\Omega W(0^{\circ})$ in 2π geometry .

In the case of ^{48}Sc , where there are three gamma-ray cascades , only the 2.36 Mev triple coincidence sum peak and the 1.33 Mev peaks can be resolved . The number of remaining full energy events due to the 1.33 Mev gamma-ray is given by the relationship :

$$N_{p3} = S \varepsilon_{p3} y_3 \left[1 - \varepsilon_{T1} y_1 W(0^{\circ})_{13} - \varepsilon_{T2} y_2 W(0^{\circ})_{23} \right.$$
$$\left. - \varepsilon_{T1} \varepsilon_{T2} y_1 y_2 W(0^{\circ})_{123} \right] \qquad (7.23)$$

where the subscripts 1, 2 and 3 refer to the 0.89 Mev, 1.04 Mev and 1.33 Mev gamma-rays respectively . The ratio of the two peaks can be represented as :

$$\frac{N_{p123}}{N_{p3}} = R = \frac{\varepsilon_{p1} \varepsilon_{p2} y_1 y_2 W(0^{\circ})_{123}}{(1 - \varepsilon_{T1} y_1 W(0^{\circ})_{13} - \varepsilon_{T2} y_2 W(0^{\circ})_{23} - \varepsilon_{T1} \varepsilon_{T2} y_1 y_2 W(0^{\circ})_{123})} \qquad (7.24)$$

From relation (7.24) , the triple coincidence angular correlation factor can be expressed as :

$$W(0^{\circ})_{123} = \frac{R(1 - \varepsilon_{T1} y_1 W(0^{\circ})_{13} - \varepsilon_{T2} y_2 W(0^{\circ})_{23})}{(\varepsilon_{p1} \varepsilon_{p2} y_1 y_2 + \varepsilon_{T1} \varepsilon_{T2} y_1 y_2 R)} \qquad (7.25)$$

If all the peaks can be resolved , the
angular correction factors $W(0^O)_{13}$ and $W(0^O)_{23}$
can be solved from a set of simultaneous equations
derived from the ratios of these peaks . However ,
the resolution of the NaI detector did not allow these
peaks to be resolved and hence , a value of $W(0^O)_{23} =$
$W(0^O)_{113} = 1.0$ has been assumed . This provides an
effective value for $W(0^O)_{123}$, which partially corrects
for the errors in the assumed values of $W(0^O)_{23}$ and
$W(0^O)_{13}$. From equation (7.25) , the effective value
for the triple coincidence angular correction factor
was calculated as 2.39 .

In the treatment of sum-coincidence correc-
tions , the detection efficiencies in equations (7.16)
through to (7.25) are those which have been corrected
for self-scattering and absorption and , hence , the
data listed in Table 7.4 should be used . Following
the treatment described , the formulae used to repre-
sent the sum-coincidence corrected full-energy peak
efficiencies are as follows :

^{46}Sc

$$\mathcal{E}_{P(0.89)}\Bigg]_{\substack{\text{sum-coincidence} \\ \text{corrected}}} = \mathcal{E}_{P(0.89)}\ ^{Y(0.89)}\left[1 - \mathcal{E}_{T(1.12)}\ ^{Y(1.12)}W_{12}(0^O)\right]$$

(7.26)

$$\left. \varepsilon_{P(1.12)} \right]_{\substack{\text{sum-coincidence}\\\text{corrected}}} = \varepsilon_{P(1.12)} Y(1.12) \left[1 - \varepsilon_{T(0.89)} Y(0.89) W_{12}(0^\circ) \right]$$

<div align="right">(7.27)</div>

48Sc

$$\left. \varepsilon_{P(1.33)} \right]_{\substack{\text{sum-coincidence}\\\text{corrected}}} = \varepsilon_{P(1.33)} Y(1.33) \left[1 - \varepsilon_{T(0.98)} Y(0.98) W_{13}(0^\circ) \right.$$
$$- \varepsilon_{T(1.04)} Y(1.04) W_{23}(0^\circ)$$
$$\left. - \varepsilon_{T(0.98)} Y(0.98) \varepsilon_{T(1.04)} Y(1.04) W_{123}(0^\circ) \right]$$

<div align="right">(7.28)</div>

where the subscripts 1, 2 and 3 refer to the first , second and third peaks , in order of energy , due to 46Sc and 48Sc .

The sum-coincidence full energy peak efficiencies are listed in Table 7.5 .

Table 7.5 : Sum-coincidence corrected full-energy peak efficiencies

	Energy (Mev)	ε_p sum corrected
46Sc	0.89	0.05057
	1.12	0.04818
48Sc	1.33	0.02433

The sum-coincidence corrected full-energy peak efficiencies for the 0.98 Mev and the 1.04 Mev

gamma-rays are not listed in Table 7.5 since these peaks could not be resolved and , therefore , not corrected for .

The 1.33 Mev full-energy peak efficiency for ^{48}Sc must be regarded as approximate only since the corrections applied are approximate . The 0.159 Mev full-energy peak efficiency for ^{47}Sc does not require sum-coincidence corrections and , hence , the data presented in Table 7.4 can be used to determine the activity .

7.3.4 Sample activity

The total counts under a full-energy peak (N_{total} = peak area) were determined using the methods described in Section 7.2.1 . The integrated activity over a period of accumulation , Ac_{total}, is given by:

$$Ac_{total} = Ac_o \int_o^{t_a} e^{-\lambda t} dt = N_{total}/\varepsilon_p \qquad (7.29)$$

Hence ,

$$Ac_o = \frac{\lambda N_{total}}{\varepsilon_p(1-e^{-\lambda t_A})} \qquad (7.30)$$

where Ac_o is the activity at the start of counting , λ the decay constant of the nuclide and t_a the accumulation time . The sample activity immediately following irradiation was determined from a measure-

ment of the activity at the start of the counting
period and the time interval following irradiation .

CHAPTER 8

Computation of Cross-section

and

Results

CHAPTER 8

The methods employed in the measurement of neutron flux have been described in Chapter 4 , whilst the techniques employed to determine the induced gamma-ray activity have been described in the previous chapter . A description of the treatment of experimental data relevant to the computation of neutron cross-sections follows .

8.1 Computation of neutron cross-sections

Under ideal conditions , for a parallel neutron beam and where all nuclei under irradiation exhibit negligible self-shielding and attenuation of the incident neutron flux , the (n, p) reaction rate, R , is given by the equation :

$$R = \sigma_R \, \phi A x_s N \qquad (8.1)$$

where σ_R represents the microscopic (n, p) reaction cross-section in barns (10^{-24} cm^2) , ϕ the neutron flux in neutrons cm^{-2}s^{-1} , A the area of the sample exposed to the neutron flux in cm^2 , x_s the sample thickness in cm and N the number of nuclei per unit volume (cm^{-3}) . Alternatively , the reaction rate R can be written in terms of the macroscopic (n, p) reaction cross-section ,Σ_R , where :

$$\Sigma_R = \sigma_R N$$

and hence ,

$$R = \Sigma_R \phi A x_s \qquad (8.2)$$

However , the neutron flux is attenuated as it traverses the sample , such that :

$$\phi = \phi_0 e^{-\Sigma_T x_s} \qquad (8.3)$$

where ϕ_0 is the neutron flux incident upon the sample surface and Σ_T the total macroscopic cross-section . Hence , for a parallel neutron beam , the reaction rate R is more rigourously defined by the equation :

$$R = \frac{\Sigma_R}{\Sigma_T} \phi_0 A \left[(1-\exp(-\Sigma_T x_s) \right] \qquad (8.4)$$

In the present work , there was non-uniform irradiation of the sample . The divergence of the incident neutron beam resulted in a variation of neutron flux both radially and transversely across the sample volume . These conditions were complicated further by the anisotropy in neutron emission .

The irradiation conditions were simulated through the use of a Monte Carlo program NPROFILE (Appendix 2) , to provide the spatial and energy distributions of neutrons incident upon the sample .

This program was extended so as to determine the activation rate in the sample .

If the effect of divergence of the beam is considered negligible across the sample , the activation rate can be represented by the equation :

$$R = \frac{\Sigma_R}{\Sigma_T} \phi_0 A \left[1 - \langle \exp(-\Sigma_T \xi) \rangle \right] \qquad (8.5)$$

where :

$$\langle \exp(-\Sigma_T \xi) \rangle = 1/N_{hist} \sum_{j=1}^{N_{hist}} \exp(-\Sigma_T \xi_j) \qquad (8.6)$$

and where ξ_j represents the path length of individual neutrons traversing the sample , N_{hist} is the number of neutron paths followed . To account for the divergence of the neutron beam incident upon the sample , the sample is divided into n disc elements of equal thickness. If the divergence of neutron flux across each of these elements is considered negligible , equation (8.5) can be applied to each element and the individual contributions to the reaction rate summed, such that :

$$R = \frac{\Sigma_R}{\Sigma_T} \phi_0 A \sum_{i=1}^{n} \frac{N_i}{N_1} \left[\langle \exp(-\Sigma_T \xi_{i-1}) \rangle ! (1 - \langle \exp(-\Sigma_T \xi_i) \rangle) \right]$$

$$(8.7)$$

N_i/N_1 represents the ratio of the unattenuated neutron flux at the ith element to that at the sample face and is represented in the Monte Carlo calculation by the ratio of the number of successful trials in element i to that in the first element . The factorial term in equation (8.7) is required to account for the flux attenuation in the preceeding elements of the flux incident upon that element . A mathematical represen- tation of the irradiation geometry is illustrated in Fig . 8.1 .

The neutron flux , ϕ_F , monitored by the uranium deposit is related to ϕ_0 by the equation :

$$\phi_F = \phi_0 \; N_F/N_1 \; \langle \exp(-(\Sigma_T \xi + \Sigma_{Tb} \xi_b)) \rangle \qquad (8.8)$$

where the term $\langle \exp(-(\Sigma_T \xi + \Sigma_{Tb} \xi_b)) \rangle$ arises from the attenuation of the neutron flux by the sample and the platinum backing of the uranium deposit, Σ_{Tb} is the total macroscopic cross-section of the platinum backing , ξ_b the neutron path lengths in the platinum backing and , N_F the number of successful trials in the uranium deposit . From equations (8.7) and (8.8) , the microscopic(n, p) reaction cross-section can be written as :

$$\sigma_R = \frac{R}{N \; \phi_F \; A f(\langle \xi, \Sigma_T \rangle)} \qquad (8.9)$$
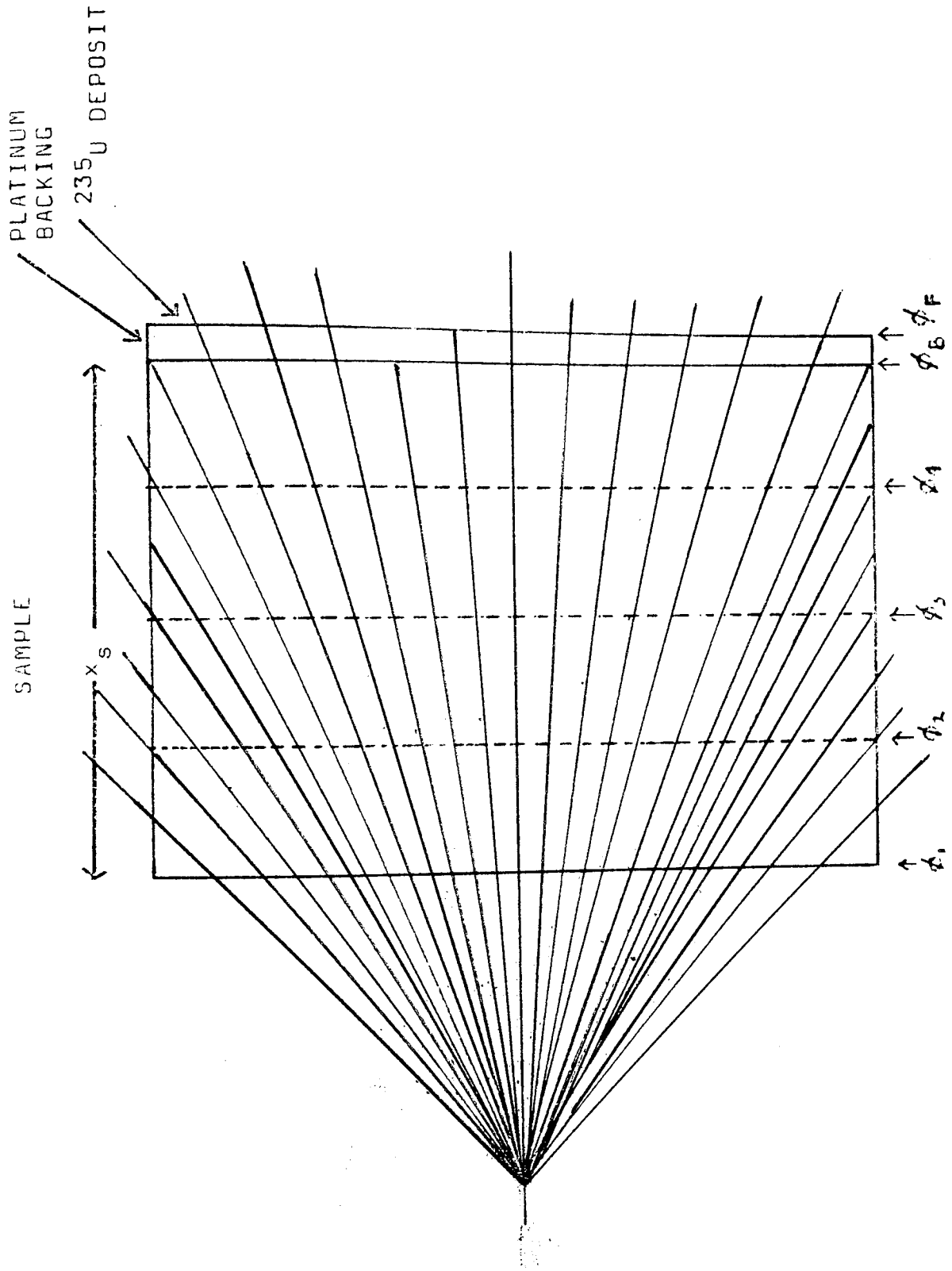
Fig. 8.1 : Mathematical representation of the irradiation geometry.

where :

$$f(<\xi>, \Sigma_T>) = \left[\frac{1}{\Sigma_T N_F <\exp[-(\Sigma_T\xi + \Sigma_{Tb}\xi)]>} \right]$$

$$\cdot\left[\sum_{i=1}^{n} N_i (1 - <\exp(-\Sigma_T\xi_i)>) (<\exp(-\Sigma_T\xi_{i-1})>!) \right]$$

$$(8.10)$$

The averaged terms in equation (8,10) are
determined using the program NPROFILE .

The remaining experimentally determined
variables in equation (8.9) are the reaction rate ,
R , and the neutron flux , ϕ_F , monitored by the
fission chamber . Both these variables are obtained
from the experimental measurements described in Chapter
8 and Chapter 4 , respectively .

In providing the neutron energy profile ,
and , therefore , the energy resolution relating to
a particular cross-section measurement , the program
NPROFILE provides also the mean neutron energy . This
is determined by weighting the individual neutron
energies E_n by the corresponding neutron path lengths
in the sample and provides a more accurate represen-
tation of the neutron energies contributing to an
observed activity . The program NPROFILE determines
the mean energy , E , from the equation :

$$\langle E \rangle = \cfrac{1}{\sum\limits_{J=1}^{N_{hist}} \xi_j} \sum\limits_{j=1}^{N_{hist}} E \, \xi_j \qquad (8.11)$$

If necessary , the program can be extended to provide the mean neutron energy incident upon the uranium-235 monitor . However , the uranium-235 fission cross-section is slowly varying over the neutron energy range 3.5 Mev to 6.0 Mev covered by this work and is found not to be particularly sensitive to an energy change of several Kev .

Reaction Rate

The reaction rate , R, is related to the experimentally determined activity Ac at the start of gamma-ray counting through the equation :

$$R = \frac{Ac \, e^{\lambda t_d}}{y(1-e^{-\lambda t_i})} \qquad (8.12)$$

where λ is the decay constant of the induced gamma-ray activity , t_d the time interval between the end of irradiation and the start of counting , t_i the irradiation time and y the branching ratio of the gamma-ray decay scheme .

During long irradiations , it was often necessary to stop the irradiation for short intervals

of time . In these circumstances , the irradiation
time , t_i , was obtained by subtracting the time of
stoppage from the total irradiation time .

Neutron Flux

The neutron flux , ϕ_F , was determined from
the uranium-235 fission count rate , C_f , by the
equation :

$$\phi_f = C_{f/} \, \mathcal{E}_f \qquad\qquad (8.13)$$

where $\mathcal{E}_f$ is the neutron detection efficiency of the
fission counter .

The fission count rate was obtained from
the experimentally observed fission counts following
corrections for fragment absorption and momentum effects
as described in Chapter 4 ; the other correction factors
such as dead time and alpha-particle pulse pile-up ,
were negligible . The absorption correction factor
was 1.0084 for the U-235 foil , for a mean fragment
range of 7.5 mg cm^{-2} /63/ and a lower pulse height
discriminator setting corresponding to 15 Mev fragment
energy (equation 4.6) , and 1.0171 for the U-238 foil.
When multiplied by a further correction factor for
the effect of the momentum of incoming neutrons
(equation 4.7) , an overall energy-dependent correction

factor is obtained . Table 8.1 presents these correc-
tion factors .

Table 8.1 : Correction factors applied to the observed
fission counts in the ^{235}U foil and the
^{238}U foil .

Neutron Energy E_n (Mev)	Correction Factor	
	^{235}U foil	^{238}U foil
3.51	1.0034	1.0120
4.07	1.0031	1.0117
4.32	1.0030	1.0115
4.57	1.0029	1.0114
4.81	1.0027	1.0112
4.93	1.0027	1.0112
5.04	1.0026	1.0111
5.16	1.0025	1.0111
5.27	1.0025	1.0111
5.38	1.0024	1.0110
5.54	1.0023	1.0109
5.65	1.0021	1.0109
5.91	1.0020	1.0107

For the U-235 foil , the neutron detection
efficiency is :

$$\varepsilon_{f235} = N_u \, (\sigma_{235} \, \%_{235} + \sigma_{238} \, \%_{238} + \sigma_{234} \, \%_{234})$$

$$(8.14)$$

and for the U-238 foil :

$$\varepsilon_{f238} = N_u (\sigma_{238} \%_{238} + \sigma_{235} \%_{235}) \qquad (8.15)$$

where N_u is the total number of uranium nuclei (see Chapter 5) , σ_{234} , σ_{235} , σ_{238} the microscopic fission cross-sections and , $\%_{234}$, $\%_{235}$, $\%_{238}$ the fractional abundance of an individual isotope .

The fission cross-section data used in equations (8.14) and (8.15) is that obtained from ENDF/B-IV . The data for σ_{235} and σ_{238} is listed in Tables 8.2 and 8.3 , whilst the interpolated data corresponding to measurements at specific energies is presented in Table 8.4 . The corresponding detection efficiencies are listed in Table 8.5 . The data for σ_{234} are obtained from ref./127/ since the detection efficiencies are not sensitive to these values .

Further corrections are required to the experimentally determined gamma-ray activity in the sample and to the fission counts prior to the use of equation (8.9) . These corrections are considered in the following section .

Table 8.2 : <u>ENDF/B-IV U-235 fission cross-sections in</u> <u>barns</u>

E_n (Mev)	$\sigma_{n,f}$	E_n	$\sigma_{n,f}$
3.1	1.2218	5.3	1.07770
3.2	1.2213	5.32858	1.07547
3.3	1.2014	5.35	1.07380
3.4	1.19200	5.4	1.06960
3.5	1.1830	5.45	1.06500
3.6	1.1770	5.5	1.05900
3.7	1.1710	5.55	1.05280
3.8	1.1620	5.6	1.05000
3.9	1.1580	5.65	1.05330
4.0	1.1500	5.7	1.06250
4.1	1.14300	5.75	1.07460
4.2	1.13800	5.8	1.08750
4.3	1.1300	5.9	1.12700
4.4	1.1250	6.0	1.1600
4.5	1.1200	6.1	1.19300
4.6	1.11300	6.2	1.23200
4.7	1.10800	6.3	1.27400
4.8	1.10200		
4.9	1.09700		
5.0	1.09400		
5.1	1.0900		
5.15	1.08750		
5.2	1.08440		
5.25	1.08120		

Table 8.3 : ENDF/B-IV U-238 fission cross-sections

E_n (Mev)	$\sigma_{n,f}$ (barns)
3.1	0.541
3.5	0.554
4.0	0.565
4.5	0.563
5.0	0.554
5.2	0.559
5.4	0.562
5.5	0.565
5.8	0.603
6.0	0.661
6.2	0.723
6.5	0.835

Table 8.4 : Interpolated fission cross-sections

Neutron Energy (ENDF/B-IV) (Mev)	σ_{234} (barns)	σ_{235} (barns)	σ_{238} (barns)
3.51	1.375	1.184	0.554
4.07	1.325	1.155	0.565
4.32	1.31	1.131	0.565
4.57	1.292	1.125	0.563
4.82	1.270	1.103	0.560
4.93	1.260	1.098	0.556
5.04	1.250	1.110	0.556
5.16	1.300	1.088	0.559
5.27	1.330	1.089	0.561
5.38	1.350	1.084	0.562
5.54	1.375	1.063	0.570
5.65	1.410	1.053	0.585
5.91	1.475	1.13	0.635

Table 8.5 : Neutron Detection Efficiencies

Neutron Energy (Mev)	Neutron detection efficiency in fissions per unit flux	
	ε_{f235}	ε_{f238}
3.51	9.821 E-7	9.964 E-7
4.07	9.594 "	9.832 "
4.32	9.401 "	9.83 "
4.57	9.3497 "	9.797 "
4.81	9.1717 "	9.74 "
4.93	9.128 "	9.67 "
5.04	9.224 "	9.675 "
5.16	9.055 "	9.727 "
5.27	9.067 "	9.762 "
5.38	9.0309 "	9.779 "
5.54	8.868 "	9.918 "
5.65	8.799 "	1.0179 E-6
5.91	9.442 "	1.1049 E-6

8.2 Corrections applied to the measured gamma-ray activity and fission counts

8.2.1 Scattering Corrections

In determining the contribution to the gamma-ray activity in the sample and the fission counts in the uranium deposit from scattered neutrons, the approach adopted is that of Smith et al /124/ . A schematic representation of the scattering processes is depicted in Fig . 8.2 .

Scattering process
type :

(α) ALPHA

(β) BETA

(γ) GAMMA

PLATINUM
BACKING

SAMPLE

U-235
DEPOSIT
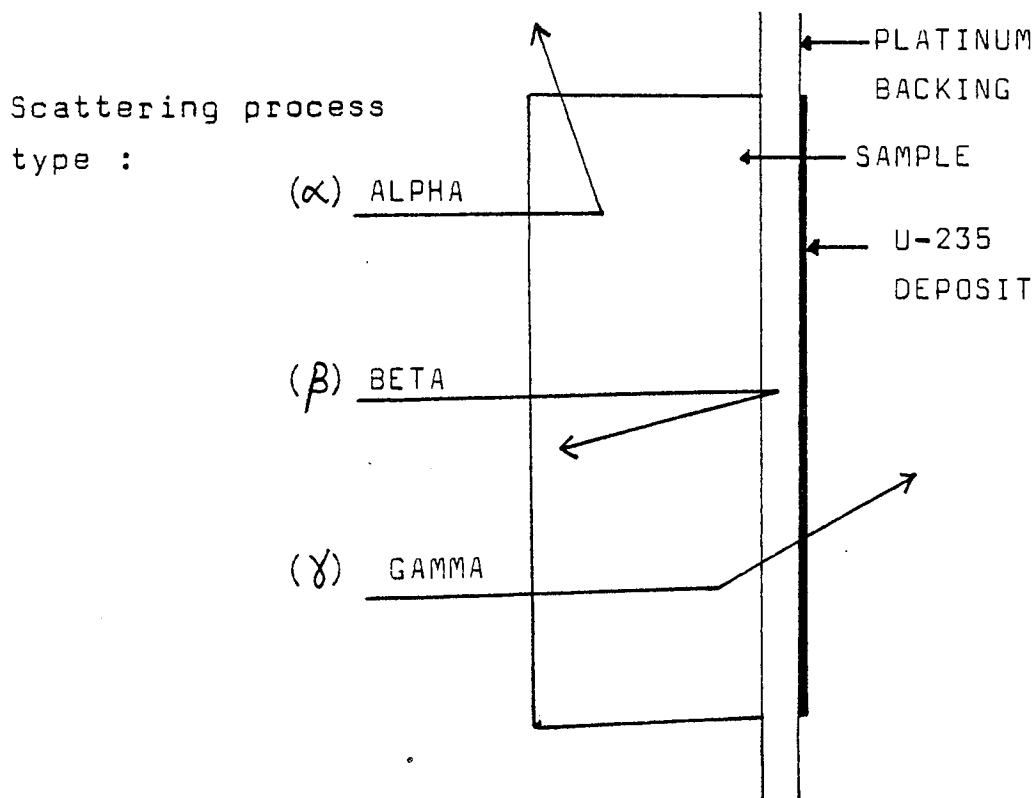
Fig . 8.2 : A schematic representation of the neutron scattering processes in the sample and fission chamber .

The scattering correction parameters α and β represent the number of activations initiated through neutron scattering in the sample and the 0.125 mm platinum backing of the uranium-235 deposit, respectively . The scattering parameters γ and ρ represent the contribution to the fissions in the uranium-235 deposit due to neutrons which are scattered in the sample and the platinum backing , respectively.

Only single scattering is considered in this treatment since the probability for multiple scattering is small . This is evident from the fact that neutron transmission through the sample is of the order of 96% and the single scattering corrections are of the order of 3% of the induced activities . Meadows /125/ has shown that the multiple scattering contributions from other portions of the fission counter cancel out in geometries similar to the present one . Nevertheless , the fission chamber has been designed to have low mass . Hence , the scattering parameters mentioned above are sufficient .

A Monte Carlo program , NSCATT , described in Appendix 5 , has been used to determine the scattering correction parameters . The derivation of the formulae used to provide the parameters α, β , γ and ρ are now described . In the present treatment, a parallel incident neutron flux and isotropic neutron scattering are assumed .

Scattering parameter α

Following the approach used in Section 8.1 but assuming a uniform , parallel beam incident upon the sample , the scattered neutron flux , ϕ_α , is given by :

$$\phi_\alpha = \frac{\Sigma_{ss}}{\Sigma_T} \; \phi_0 (1 - <\exp(- \Sigma_T x_s) >) \tag{8.16}$$

where Σ_{ss} is the macroscopic elastic scattering cross-section in the sample . Hence , the (n, p) reaction rate due to the scattered neutron flux is :

$$R_\alpha = A \frac{\Sigma_R}{\Sigma_T} \frac{\Sigma_{ss}}{\Sigma_T} \; \phi_0 (1 - <\exp(- \Sigma_T x_s) >) \; (1 - <\exp(-\Sigma_T \xi) >)$$

$$\tag{8.17}$$

The neutron path length in the sample of the scattered neutrons is represented by ξ , rather than x_s .

The scattering parameter , α , is defined as the ratio of the (n, p) reaction rate arising from scattered neutrons to that from the incident neutron flux :

$$\alpha = \frac{R_\alpha}{R} = \frac{\Sigma_{ss}}{\Sigma_T} (1 - <\exp(- \Sigma_T \xi) >) \tag{8.18}$$

Scattering Correction β

The scattered neutron flux in the platinum

backing is :

$$\phi_B = \frac{\Sigma_{SB}}{\Sigma_{TB}} \phi_0 \exp(-\Sigma_T x_s)(1-\exp \Sigma_{BS} x_B) \quad (8.19)$$

where Σ_{SB} is the macroscopic elastic scattering cross-section in the backing material , Σ_{TB} the total macroscopic cross-section in the backing material and, x_B the thickness of the backing material .

The (n, p) reaction rate produced in the sample as a result of this scattered flux is given by:

$$R_\beta = A \frac{\Sigma_R}{\Sigma_T} \frac{\Sigma_{SB} \phi_0}{\Sigma_{TB}} \exp(-\Sigma_T x_s) \left[1-\exp(-\Sigma_{TB} x_B) \right]$$

$$\cdot \left\langle \exp(-\Sigma_{TB} \xi_B) \left[1-\exp(-\Sigma_T \xi) \right] \right\rangle \quad (8.20)$$

where ξ_B is the neutron path length of the scattered neutrons in the backing material . The scattering correction β is defined as :

$$\beta = R_\beta / R = \frac{\Sigma_{SB}}{\Sigma_{TB}} \frac{\exp(-\Sigma_T x_s) \left[1-\exp(-\Sigma_{TB} x_B) \right]}{\left[1-\exp(1-\Sigma_T x_s) \right]}$$

$$\cdot \left\langle \exp(-\Sigma_{TB} \xi_B) \left[1-\exp(-\Sigma_T \xi) \right] \right\rangle \quad (8.21)$$

Scattering Correction γ

The corrections for fission events induced by elastically scattered neutrons in the sample and

backing require knowledge of the thickness of the uranium deposit . An effective thickness was calculated from the equation :

$$x_f = \text{deposit mass}/(A^2 \times \text{density of uranium}) \quad (8.22)$$

and an effective macroscopic cross-section is normalised such that :

$$\frac{N_u \, \overline{\sigma_{n,f}}}{A} = \Sigma_f \, x_f \quad (8.23)$$

where N_u is the total number of uranium atoms .

The fission reaction rate in the uranium deposit due to the incident neutron flux , ϕ_o , is given by :

$$R_f = \frac{A \Sigma_f}{\Sigma_{Tf}} \, \phi_o \, \exp\left[-(\Sigma_T \, x_s + \Sigma_{TB} \, x_B)\right]\left[1-\exp(-\Sigma_{Tf} x_f)\right]$$

$$(8.24)$$

where Σ_{Tf} is the total macroscopic cross-section in the uranium foil . The fission reaction rate due to neutrons elastically scattered in the sample is given by :

$$R_\gamma = \frac{A \Sigma_f \Sigma_{ss}}{\Sigma_{Tf} \Sigma_T} \, \phi_o \left[1-\exp(-\Sigma_T x_s)\right]\left\langle\exp\left[-(\Sigma_T \xi + \Sigma_{TB} \xi_B)\right]\right.$$

$$\left. \cdot \left[1-\exp(-\Sigma_{Tf} \xi_f)\right]\right\rangle \quad (8.25)$$

where ξ_f is the neutron path length of the scattered neutrons in the uranium foil . The scattering correction δ is defined as :

$$R_\gamma / R_f = \frac{\Sigma_{ss}}{\Sigma_T} \exp(\Sigma_T x_s + \Sigma_{TB} x_B) \frac{\left[1-\exp(-\Sigma_T x_s)\right]}{\left[1-\exp(-\Sigma_{Tf} x_f)\right]}$$

$$\cdot \left\langle \exp\left[-(\Sigma_T \xi + \Sigma_{TB} \xi_B)\right]\left[1-\exp(-\Sigma_{Tf} \xi_f)\right]\right\rangle \qquad (8.26)$$

Scattering Correction ρ

The fission reaction rate in the uranium deposit due to neutrons elastically scattered in the platinum backing is given by :

$$R_\rho = A \frac{\Sigma_f \Sigma_{SB}}{\Sigma_{Tf} \Sigma_{TB}} \phi_0 \exp(-\Sigma_T x_s)\left[1-\exp(-\Sigma_{TB} x_B)\right]$$

$$\cdot \left\langle \exp(-\Sigma_{TB} \xi_B)\left[1-\exp(-\Sigma_{Tf} \xi_f)\right]\right\rangle \qquad (8.27)$$

Hence the scattering correction ρ is given by:

$$\rho = R_\rho / R_f = \frac{\Sigma_{SB}}{\Sigma_{TB}} \exp(\Sigma_{TB} x_B) \frac{\left[1-\exp(-\Sigma_{TB} x_B)\right]}{\left[1-\exp(-\Sigma_{Tf} x_f)\right]}$$

$$\cdot \left\langle \exp(-\Sigma_{TB} \xi_B)\left[1-\exp(-\Sigma_{TB} \xi_f)\right]\right\rangle \qquad (8.28)$$

The scattering correction ρ is independent of the type of sample used . Hence , the calculated values for ρ can be applied to any fission counter configuration used for the present work .

The scattering corrections corresponding to the parameters α , β , γ and ρ , as determined by the program NSCAT , are listed in Table 8.6 . Using this data , the experimentally determined (n,p) reaction rate , $R_{measured}$, in the sample and the measured fission count rate , $C_{f\ measured}$, were corrected , such that :

$$R = \frac{R_{measured}}{1 + \alpha + \beta} \qquad (8.29)$$

$$\text{and } C_f = \frac{C_{f\ measured}}{1 + \gamma + \rho} \qquad (8.30)$$

The corresponding correction factors , tabulated as $1/(1 + \alpha + \beta)$ and $1/(1 + \gamma + \rho)$, are presented in Table 8.7 .

Table 8.6 : Neutron scattering corrections $\alpha, \beta, \gamma, \rho$

Neutron Energy (Mev)	α	β	γ	ρ
5.91	2.64%	0.367%	0.825%	0.28%
5.65	2.74	0.367	0.857	"
5.54	2.78	0.367	0.87	"
5.38	2.85	0.368	0.89	"
5.27	2.89	0.368	0.90	"
5.16	2.92	0.368	0.91	"
5.04	2.96	0.369	0.92	"
4.93	3.03	0.369	0.94	"
4.82	3.09	0.369	0.96	"
4.57	3.17	0.37	0.99	"
4.32	3.29	0.37	1.05	"
4.07	3.40	0.37	1.10	"
3.51	3.58	0.37	1.21	"

Table 8.7 : Scattering Correction Factors for
experimental data

Neutron Energy (Mev)	$1/(1 + \alpha + \beta)$	$1/(1 + \gamma + \rho)$
5.91	0.9712	0.9891
5.65	0.9699	0.9887
5.54	0.9695	0.9886
5.38	0.9688	0.9884
5.27	0.9685	0.9883
5.16	0.9682	0.9882
5.04	0.9678	0.9881
4.93	0.9672	0.9879
4.82	0.9666	0.9878
4.57	0.9658	0.9875
4.32	0.9647	0.9869
4.07	0.9637	0.9864
3.51	0.9620	0.9853

8.2.2 Corrections for background neutrons

Above a given deuteron beam energy , (d, n) reactions in the gas target material and in carbon deposits accumulated during beam bombardment introduce a neutron background , contributing to the fission counts and sample γ-activity observed . A further contribution originates from the loading of deuterium in the gas target beam stop . This neutron background is deuteron-energy dependent and is generally observed to increase with deuteron energy .

Background contributions must be subtracted from the measured activity . To determine these contributions , the sample and fission counter were irradiated with the gas target evacuated and the observed fissions and sample γ-activity normalised to the integrated deuteron beam current . Since the time available on the Dynamitron accelerator was limited , only two such irradiations were performed, one corresponding to a neutron energy of 5.91 Mev and another at 4.81 Mev . The contributions at other energies were interpolated from the results of the two measurements . These are presented in Table 8.8 .

8.2.3 Corrections for background thermal neutrons

The use of uranium-235 for neutron flux measurements results in the detection of fission

Table 8.8 : Background neutron contribution to the observed activity in the fission counter and the sample

Neutron Energy(Mev)	Fission counts	Sample γ-activity		
		^{46}Sc	^{47}Sc	^{48}Sc
3.51	1.8%	Negligible	Negligible	Negligible
4.07	2.0%	"	"	"
4.32	2.1%	"	"	"
4.57	2.15%	"	"	"
4.81	2.2%	0.1%*	0.3%	"
4.93	2.4%	0.14%	0.38%	"
5.04	2.6%	0.18%	0.46%	"
5.16	2.8%	0.23%	0.55%	"
5.27	2.9%	0.27%	0.62%	"
5.38	3.1%	0.3%	0.7%	"
5.54	3.4%	0.36%	0.81%	"
5.65	3.5%	0.39%	0.89%	"
5.91	3.8%	0.45%*	1.0%*	0.3%*

*measured values

The background fission contribution was measured for all energies .

events due to thermal neutron reactions . Although
this contribution could be eliminated through the use
of uranium-238 , such a foil was not available when
the present work was started .

The close proximity of the fission counter
to the gas target did not allow the use of a shadow
bar to determine the thermal neutron contribution . Neutron
flux measurements were made with a back-to-back double
fission chamber , Fig. 8.3 , incorporating two uranium
deposits , one uranium-238 enriched (see Chapter 5)
and the other , the uranium-235 enriched foil used in
the present work .

The fission counts in the U-235 and U-238
deposits , C_{f235} and C_{f238} , respectively , are given
by :

$$C_{f235} = \phi \varepsilon_{f235} + C_{fthermal} \qquad (8.31)$$

and

$$C_{f238} = \phi \varepsilon_{f238} \qquad (8.32)$$

where   is the non-thermal neutron flux , ε_{235} and
ε_{238} the fast neutron detection efficiency for the
U-235 and U-238 foils , respectively , and $C_{fthermal}$
the fission count rate due to thermal neutrons . Using
equations (8.31) and (8.32) , the thermal neutron

Fig. 8.3 The back-to-back double fission chamber

contribution is given by :

$$C_{f thermal} = C_{f235} - \frac{C_{f238}\ \varepsilon_{f235}}{\varepsilon_{f238}} \qquad (8.33)$$

Hence , the correction factor by which the U-235 fission count rate is multiplied to yield the thermal neutron corrected fission rate is given by :

$$\alpha_{thermal} = \frac{C_{f238}\ \varepsilon_{f235}}{C_{f234}\ \varepsilon_{f238}} \qquad (8.34)$$

The measured thermal neutron contributions as a percentage of the total fission counts and the corresponding thermal neutron correction factors , α thermal , are listed in Table 8.9 as a function of neutron energy .

In order to avoid systematic errors from the irradiation geometries for the two foils , the positions of the two foils were interchanged and the mean fission-rates used to provide the data in Table 8.9 .

Table 8.9 : Thermal neutron corrections to fission counts

Neutron Energy(Mev)	% Thermal fission counts	$\alpha_{thermal}$
3.51	4.6	0.954
4.07	3.7	0.963
4.32	3.5	0.965
4.57	3.4	0.966
4.81	3.2	0.968
4.93	3.0	0.97
5.04	3.0	0.97
5.16	2.7	0.973
5.27	2.4	0.976
5.38	2.2	0.978
5.54	1.9	0.981
5.65	1.7	0.983
5.95	1.5	0.985

8.3 Results

Results obtained from the present measurements of the ^{46}Ti(n, p)^{46}Sc , ^{47}Ti(n, p)^{47}Sc and the ^{48}Ti(n, p)^{48}Sc reaction cross-sections are presented in Tables 8.10 to 8.12 . Available data of other workers covering the present neutron energy range (3.5 Mev to 5.9 Mev) are compared with these results in Figs . 8.4 to 8.6 . The one standard deviation accuracies for the ^{46}Ti(n, p) and ^{47}Ti(n, p)^{47}Sc reactions are 6% and 5%, respectively , whilst the ^{48}Ti(n, p)^{48}Sc reaction is subject to a systematic error due to the sum-coincidence corrections applied (Chapter 7) , probably of the order of 20% . With this exception , the only other measurement of comparable accuracy to the present is that of Smith et al /10 /.

Agreement between the present measurements and those of Smith et al are good , considering the statistical fluctuation in the data . Nevertheless , a small systematic difference is evident , with present values being generally higher . However , if the ^{235}U(n, f) data used by Smith et al are updated to the more recent ENDF/8-IV data used in the present work , this difference is largely eliminated .
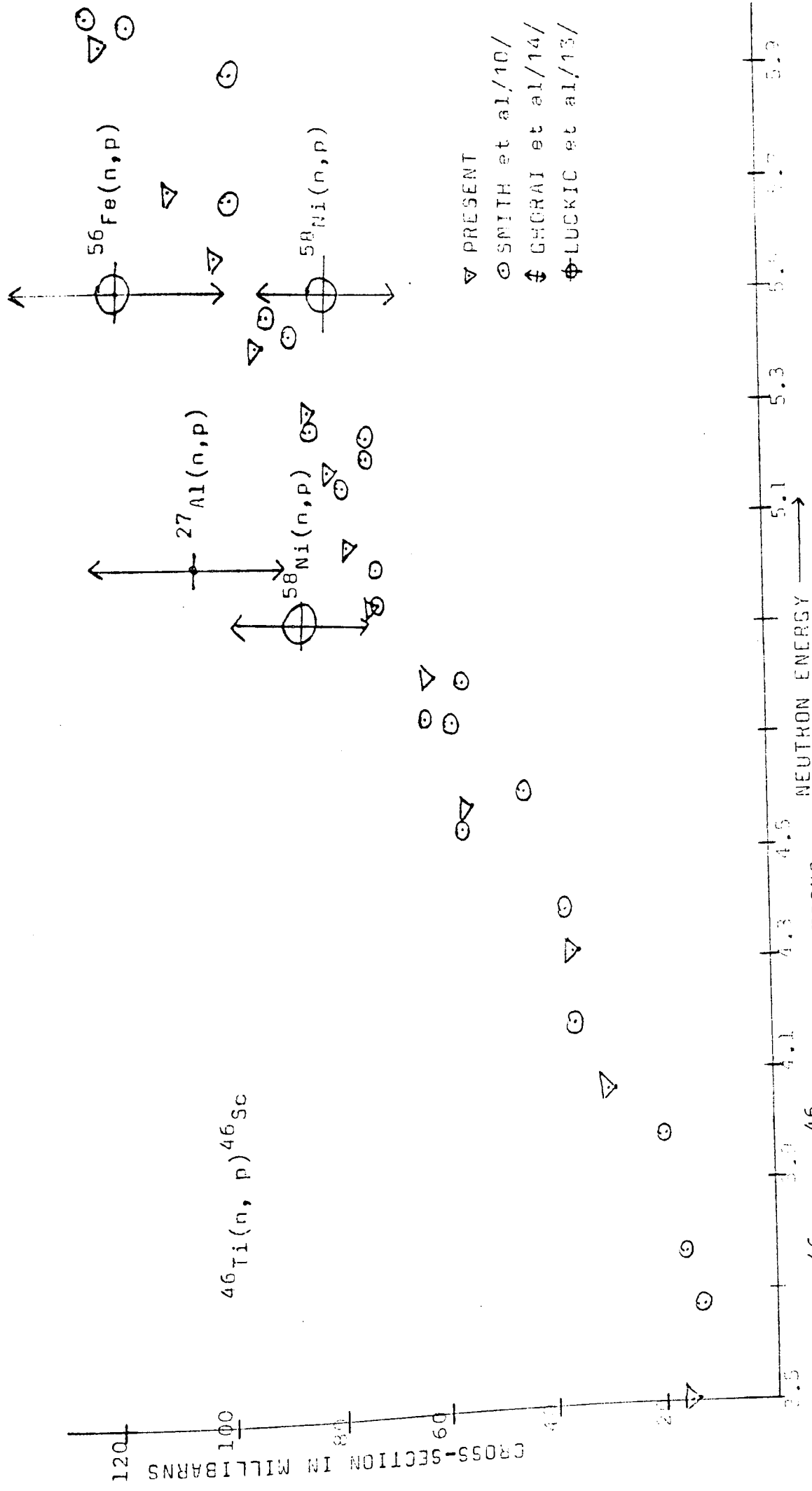
FIG. 8.4: $^{46}Ti(n,p)^{46}Sc$ CROSS-SECTIONS
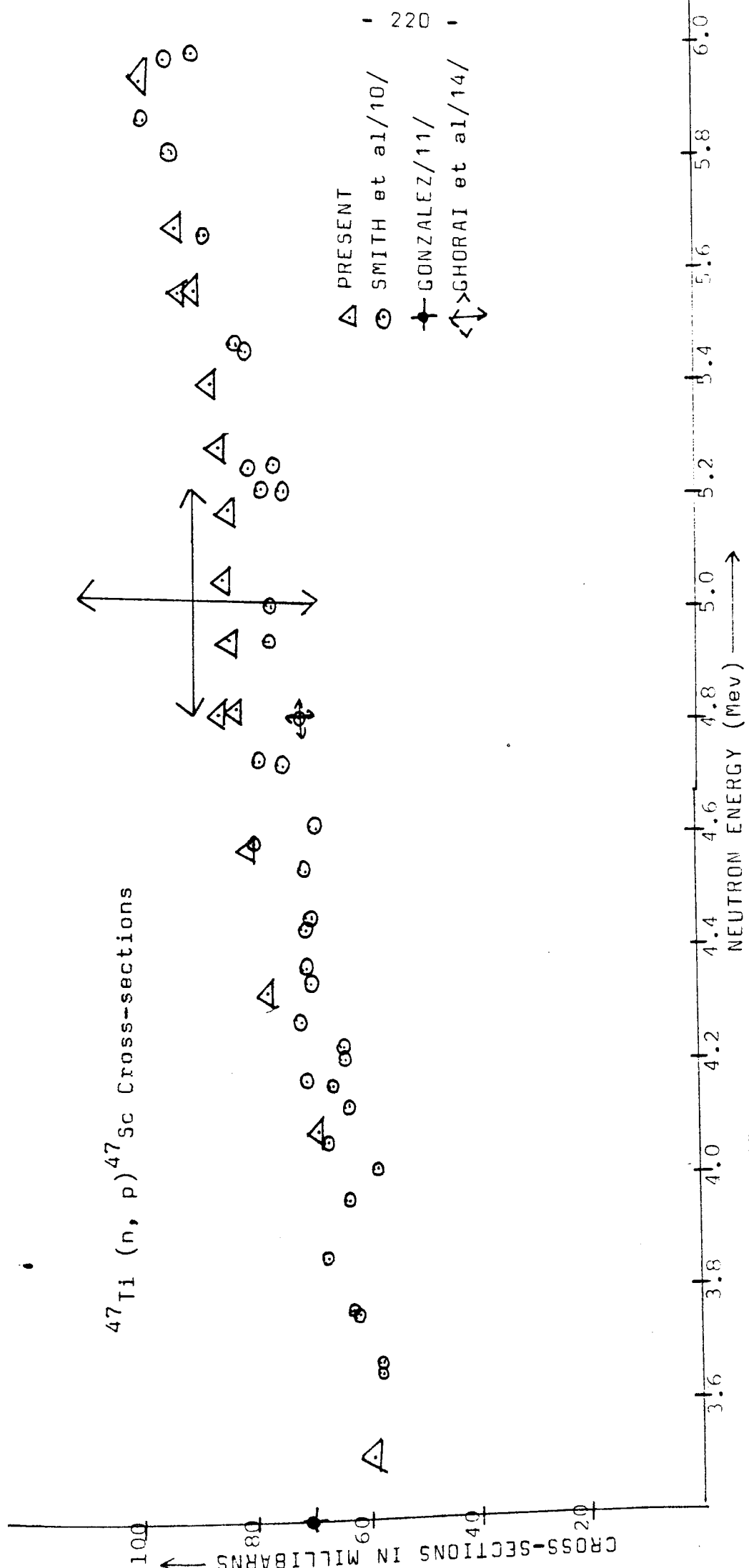
FIG.8.5: $^{47}Ti(n,p)^{47}Sc$ CROSS-SECTIONS
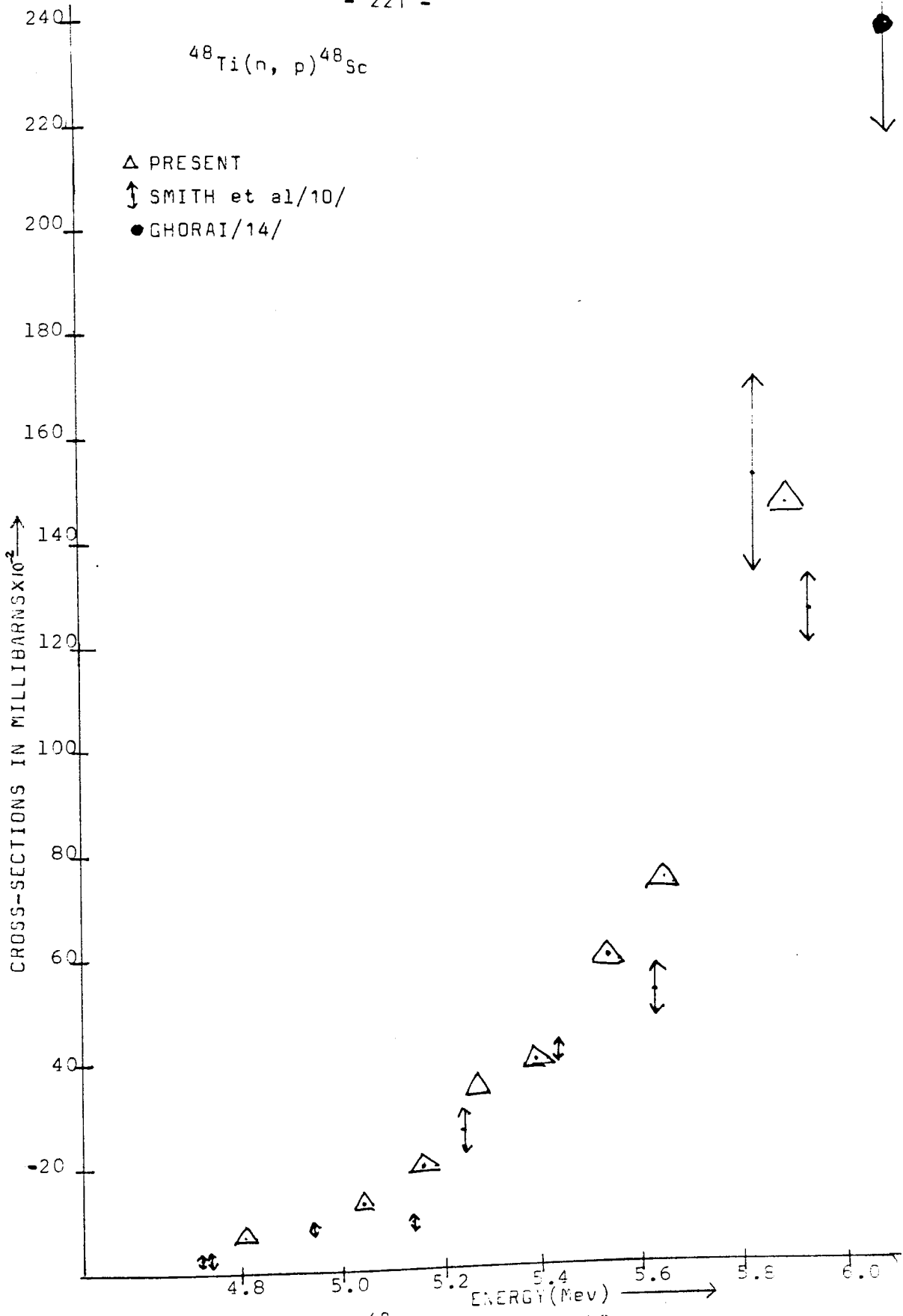
FIG. 8.6: $^{48}Ti(n, p)^{48}Sc$ CROSS-SECTIONS

Table 8.10 : Measured ^{46}Ti(n, p)^{46}Sc cross-sections

Neutron Energy (Mev)	Energy Resolution (Mev)	Cross-section (mb)	Uncertainty (mb)
3.514	0.16	15	$\pm$ 0.9
4.070	0.14	30	1.8
4.322	0.13	46	2.8
4.565	0.12	56	3.4
4.815	"	63/65	3.9
4.931	"	73	4.4
5.044	"	77	4.6
5.156	"	81	4.9
5.269	"	85	5.1
5.378	"	95	5.7
5.542	"	102/105	6.2
5.646	"	110	6.6
5.913	"	122	7.3

Table 8.11 : Measured ^{47}Ti(n, p)^{47}Sc cross-sections

Neutron Energy (Mev)	Energy Resolution (Mev)	Cross-section (mb)	Uncertainty (mb)
3.514	0.16	60	± 3.0
4.070	0.14	70	3.5
4.322	0.13	79	4.0
4.565	0.12	82	4.1
4.815	"	87/84	4.3
4.931	"	85	4.3
5.044	"	86	4.3
5.156	"	85	4.3
5.269	"	87	4.4
5.378	"	88	4.4
5.542	"	91/92	4.6
5.646	"	94	4.7
5.913	"	100	5.0

Table 8.12 : Measured ^{48}Ti(n, p)^{48}Sc cross-sections

Neutron Energy (Mev)	Energy Resolution (Mev)	Cross-section (mb)	Uncertainty (mb)
4.815	0.16	0.07	$\pm$ 0.014
4.931	0.14	0.08	0.016
5.044	0.13	0.13	0.026
5.156	0.12	0.20	0.04
5.269	"	0.35	0.07
5.378	"	0.40	0.08
5.542	"	0.60	0.12
5.646	"	0.75	0.15
5.913	"	1.48	0.30

Table 8.13 : Uncertainties

	$^{46}Ti(n,p)^{46}Sc$	$^{47}Ti(n,p)^{47}Sc$	$^{48}Ti(n,p)^{48}Sc$
Neutron flux			
Fission cross-section	3%	3%	3%
Uranium mass	1%	1%	1%
Counting statistics	0.5%	0.5%	0.5%
Background neutrons	1%	1%	1%
Gamma-ray activity			
Half-life	1%	1%	1%
Efficiency	3%	3%	3%
Peak integration	1 to 2%	1 to 2%	3 to 4%
Sum-coincidence	3%	-	20%
Self-absorption	1%	1%	1%
Counting statistics (γ-ray)	1%	0.5%	2 to 3%
Irradiation Geometry	1%	1%	1%
Total	6%	5%	21%

Data of Luckic et al /13/ for the ^{46}Ti(n,p)^{46}Sc reaction exhibit fluctuations due to the use of different neutron flux standards and are systematically higher . So too are the data of Ghorai et al /14/ made relative to the ^{27}Al(n, p)^{27}Mg reaction .

The ^{47}Ti(n, p)^{47}Sc measurements of Gonzalez /11/ agree with those of the present work and those of Smith et al at one energy only (3.5 Mev) , whilst being significantly higher at lower energies .

Uncertainties

A breakdown of the uncertainties associated with the present measurements are presented in Table 8.13 . Uncertainties arising from neutron scattering in the sample and the fission chamber are not quoted here since these corrections do not exceed 3% and an uncertainty of 10% in these corrections would only introduce an error of 0.3% in the correction factor. Hence , the effect on the overall uncertainty would be insignificant .

For the ^{47}Ti(n, p)^{47}Sc reaction , where there are no complicating effects arising from sum-coincidence events , the major sources of uncertainty are in the ^{235}U(n, f) cross-sections and the full energy peak efficiencies . It is unlikely, however , that these uncertainties will improve significantly

in the very near future .

For the $^{46}Ti(n, p)^{46}Sc$ reaction , the 3% uncertainty in the sum-coincidence correction contributes to an increase of only 1% in the overall uncertainty for this measurement .

The approximation made in the sum-coincidence correction for scandium-48 has probably led to an over-estimate of the sum-coincidence correction . However , an estimated uncertainty of approximately ± 20% could explain the differences between the present measurements and those of Smith et al .

Recommendations

The measurements of Luckic et al (op. cit.) demonstrate the difficulties associated with measurements made relative to different secondary standards . Such measurements contribute to differences between measurements which are beyond the quoted uncertainties. This is attributeable to the accentuation of systematic errors in the standards used .

Measurements made relative to the better known standards such as the H(n, p) scattering cross-section and the $^{235}U(n, f)$ cross-sections can provide more consistent results and results which can be more accurately evaluated . Although the H(n, p) cross-section is known to greater accuracy than that of

the $^{235}U(n, f)$ reaction , the greater simplicity of fission counting allows for improved consistency in measurements made relative to fission cross-section. Furthermore , measurements can be continually updated following improvements in the fission cross-section data .

It is evident also that the scatter in experimental measurements requires an increased number of measurements or , alternatively , an improvement in counting statistics . This would provide a more accurate estimate of the shape of the excitation function over a given energy range .

A major difference between the present measurements from those of Smith et al. lies in the use of a NaI(Tl) detector as opposed to a Ge(Li) detector . Furthermore , the gamma-ray counting was performed in geometries approaching 2π . This improved counting statistics , as is demonstrated in the reduced statistical scatter in the present measurements . Whilst the increased uncertainty with the sum-coincidence corrections for the $^{46}Ti(n, p)^{46}Sc$ reaction is small , a penalty is incurred with the $^{48}Ti(n,p)^{48}Sc$ reaction since some of the sum-coincidence peaks could not be resolved .

Lastly , although the use of direct on-line measurements of the emitted photons would eliminate

the uncertainties relating to the full-energy
efficiency and sum-coincidence effects (a major source
of uncertainties in the present measurements) , the
elimination of background effects would be a problem.

REFERENCES

1. B. Rose, AERE - M 2945 UKNDC (78) P.89 .

2. WRENDA 78: World request list for nuclear data measurements ; IAEA , INDC

3. J.L.Rowland , "Nuclear data for reactor design , operation and safety ." Proc.Int.Conf. Neutron Physics and nuclear data for reactors and other applied purposes . Harwell Sept. 1978 .

4. J.Konijn and A.Lauber, "Cross-section measurements of the ^{58}Ni(n, p)^{58}Co and ^{29}Si(n,α)^{26}Mg reactions in the energy range 2.2 Mev to 3.8 Mev". Nuc.Physics $\underline{48}$ (1963)191-208.

6. Dahl et al , "Neutron fluence measurements". IAEA Technical Rep. Series No.107(1970)141-163.

7. W.D.Allen, Flat response counters . Fast neutron physics, Chapter IIIA , Ed. Marion & Fowler .

8. C.H.Hogg and L.D.Weber , "Fast-neutron dosimetry at the MTR-ETR site". ASTC special technical publication No.341 (1963).

9. W.H.Taylor, K.Randle and M.F.Murphy , "Results of an investigation into the possibilities of the measurement of the Nb-93(n, n') Nb-93 m excitation function using the Birmingham Dynamitron machine". U.K. Nuclear data forum, Winfrith Dec.1979.

10. D.L.Smith and J.W.Meadows , "Cross-sections for (n, p) reactions in Al, Ti, Fe, Ni, Co and Zn for E_n from threshold to 10 Mev". Argonne National Laboratory Report ANL/NDM10 (1975).

11. L.Gonzalez, A.Trier and J.J.Van Loef, "Excitation function of the reaction $^{47}Ti(n, p)^{47}Sc$ at neutron energies between 2.0 Mev and 3.6 Mev." Physical Rev. Vol.126 No.1 April 1962 .

12. F.G.Armitage, Transmitted to the National Neutron cross-section Centre, Brookhaven Nat. Laboratory , by J.Symonds(1967) . Data available from the CSISRS file . See Reference 10 .

13. Y.Luckic and E.E.Carroll , "Titanium (n, p) cross-section measurements". Nuc. Sci. Eng. 43 (1971) 233-235 .

14. S.K.Ghorai, J.R.Cooper, J.D.Moore and W.L.Alford, "Some (n, p) cross-sections of ^{46}Ti, ^{47}Ti and ^{48}Ti". Jour.Nucl. Energy 25 P. 319 (1971).

15. J.A.Grundl , "A study of fission-neutron spectra with high energy activation detectors Part 1". Nucl. Sci. Eng. 30, P.39(1967).

16. J.F.Barry, "The cross-section of the $^{58}Ni(n, p)^{58}Co$ reaction for neutrons in the energy range 1.6 to 14.7 Mev". Jour. Nucl. Energy A/B 16, 467 (1962).

17. H.Liskien and Paulsen , "Determination of 1Mev neutron fluxes from the $T(p, n)^3He$ reaction by the associated particle method". Nuc. Instr. Meth. 69(1969) P70.

18. C.M.Bartle and H.O.Meyer, "Improved technique for the preparation of thin deuterated polyethylene targets". Nuc. Instr. Meth. 112 (1973) P615 .

19. W.P.Poenitz , "The black neutron detector , ANL-7915 ,1972 , also Nuc. Instr. & Methods , 109 , 413 (1973) .

20. V.V. Verbinski and R.G.Giovannini , "Proportional counter characteristics and applications to reactor neutron spectrometry". Nuc. Instr. Meth. 114, 205 (1974).

21. M.Ahmed , "A comparative study of n-γ discrimination properties of scintillators NE213, C_6H_6 , C_6O_6 and stilbene". Nuc. Instr. Meth. 143, 255 (1977).

22. I.B.Berlman and O.J.Steingraber, "Liquid scintillation solutions for pulse-shape discrimination". Nuc. Instr. Meth. 108, 587 (1973).

23. D.C.C.B.Syme and G.I.Crawford , "Pulse shape
      discrimination with NE211 liquid
      scintillator". Nuc. Instr. Meth. 104,
      245(1972) .

24. J.B.Czirr, "A comparison of scintillator solvents
      for pulse shape discrimination". Nuc.
      Instr. Meth. 88, 321(1970).

25. T.G.Miller, "Measurement of pulse shape discrimin-
      ation parameters for several scintilla-
      tors". Nuc. Instr. Meth. 63,121 (1968).

26. B.H.Patrick, "Fast fission cross-sections of the
      major Transactinium isotopes". Inter.
      Conf. on Neutron Physics and Nuclear
      Data, Harwell 1978.

27. F.Käppeler, "Counter techniques for highly radio-
      active samples". Neutron Phy. and Nuc.
      Data Proc. Int. Conf. Harwell Sept.1978
      pp 809-828 .

28. M.Mutterer, J.P.Theobald and K.-P.Schelhass ,"A
      low pressure Noble gas scintillation
      counter for heavy ion detection ". Nuc.
      Instr. Meth. 144, pp159-166(1977).

29. H.D.Lemke, B.Ziegler, J.Foh, M.Mutterer and J.P.
      Theobald, "Multiple ionisation chamber
      with intrinsic background discrimination
      and its response to photofission." Nuc.
      Instr. Meth. 169, (1980) 89-96 .

30. J.A.Grundl, "A study of fission spectra with high energy activation detectors part 1. Detector development and excitation measurement". Nuc. Sci. and Eng. 30, 39-53 (1967) .

31. H.Rösler, J.K.Millard and N.W.Hill, "Fast timing from a fission ionisation chamber". Nuc. Instr. Meth. 99, pp477-486 (1972).

32. J.W.Behrens and J.C.Browne, "Measurement of the neutron-induced fission cross-section of ^{241}Am relative to ^{235}U". Report UCID-17324 , Lawrence Livermore Lab.(1976).

33. C.Budtz-Jorgensen and H.H.Knitter, "A fission chamber with intrinsic suppression of alpha background". Nuc. Instr. Meth. 154, (1978) 121-125.

34. J.W.T.Dabbs, N.W.Hill, C.E.Bemis and S.Raman, "Fission cross-section measurements in short-lived alpha emitters". Proc. Conf. on Nuclear Cross-sections & Technology p81 , NBS spec. publ. 425 , (1975).

35. A.Kazerouni and F.Käppeler, "Development of a fast spherical Avalanche Fission Detector with intrinsic alpha discrimination for the measurement of the fission cross-section of ^{244}Cm". Annual Rep., Teilinstitut Kernphysik, KFK Rep.2504, p126 (1977).

36. B.G.Cartwright, E.K.Shirk and P.B.Price , "A
        nuclear track recording polymer of
        unique sensitivity and resolution".
        Nuc. Instr. Meth. 153, 457-466(1978).

37. D.C.Brunton and G.C.Hanna, "Energy distribution
        of fission fragments from ^{235}U and
        ^{233}U". Can. J. Research 28A, 190 (1950).

38. C.B.Fulmer and B.L.Cohen, "Equilibrium charges
        of fission fragments in gases". Phys.
        Rev. 109, 94(1958) .

39. G.I.Bell,"The capture and loss of electrons by
        fission fragments". Phys. Rev. 90, 548
        (1953).

40. D.H.Wilkinson, "Ionisation chambers and counters"
        (Cambridge monographs on physics) Cam.
        Uni. Press, Cam 1950.

41. R.C.Ling and J.K.Knipp, "Ionisation by recoil
        particles from alpha-decay". Phys. Rev.
        80,106(1950). Also, "On the ionisation
        yields of heavy particles". Phys. Rev.
        82, 30(1951).

42. H.W.Schmitt and R.B.Leachman, "Ionisation vs
        energy relation for fission fragments".
        Phys. Rev. 102, 183(1956).

43. W.P.Jesse and J.Sadauskis,"Alpha-particle ionisa-
        tion in pure gases and the average energy
        to make an ion pair". Phys. Rev. 90,1120
        (1953).

44. T.E.Bortner and G.S.Hurst, "Ionisation of pure gases and mixtures of gases by 5-Mev alpha-particles ". Phys. Rev. 93, 1236(1954).

45. C.E.Melton, G.S.Hurst and T.E.Bortner,"Ionisation produced by 5-Mev alpha-particles in Argon mixtures". Phys. Rev. 96,643(1954).

46. C.W.McCutchen, Senior thesis (Princeton 1950). See A.H.Snell "Nuclear Instruments and their uses" Vol.1 ,Wiley and sons (1962).

47. J.A.Bistline, "Some properties of BF_3 in ionisation chambers". Rev. Sci.Instr. 19,842(1948).

48. M.Just, D.Habs, V.Metag and H.J.Specht, "A position sensitive parallel plate avalanche detector (PPAAD) for fission fragments". Nuc. Instr. Meth.148, 283-289(1978).

49. D.H.Wilkinson, "Ionisation chambers and counters". Cambridge at the University Press 1950.

50. G.Jaffe, Ann. Physik, 42, 303 (1913).

51. T.E.Bortner, G.S.Hurst and W.G.Stone, "Drift velocities of electrons in some commonly used counting gases". Rev. Sci. Instr. 28, 103 (1957).

52. N.O.Lassen, "On the energy loss by fission fragments along their range". Kgl. Danske Videnskab. Selskab. Mat. Fys. Medd. Vol. 25 No.11 (1949).

53. W.Fano, "On the theory of ionisation yield of radiations in different substances". Phys. Rev. 70, 44(1940). Also, "Ionisation yield of radiations II . The fluctuations of the number of ions". Phys. Rev. 72, 26(1947).

54. G.D.Alkhazov, A.P.Komar and A.A.Voroblev, "Ionisation fluctuations and resolution of ionisation chambers and semiconductor detectors". Nuc.Instr.Meth. 48,1 (1967).

55. O.R.Frisch, "Isotopic analysis of uranium samples by means of their alpha-ray groups". BR-49 (unpublished report) 1944.

56. A.S.Mushtaq, "Designing, building and testing of ungridded and gridded fission ionisation chambers for neutron flux monitoring". M.Sc. THESIS University of Aston(1979).

57. A.B.Gillespie, "Signal, noise and resolution in nuclear counter amplifiers". McGraw Hill, New York (1953).

58. D.Engkkemier and G.M.Walton, AERE Report R4716(1964).

59. W.N.English and G.C.Hanna, "Grid ionisation chamber measurements of electron drift velocities in gas mixtures". Can. J.Phy.31,768(1953).

60. D.R.Weaver,"Information for new users of the Dynamitron". Birmingham Radiation Centre Paper No. BRC-74/01.

61. E.K.Hyde, " The nuclear properties of the heavy
elements 3 (Prentice-Hall, New York 1964).

62. P.W.Frank, Westing house Electric Corporation
Report WAPD-BT-30 (1964).

63. P.H.White, "Alpha and fission counting of thin
foils of fissile material". Nuc. Instr.
Meth. $\underline{79}$, 1-12 (1970).

64. M.Akhtar, "Studies to determine the uniformity
of fission foils(U_3O_8)." M.Sc. Thesis
Dept. of Physics, University of Aston 1978.

65. R.W.Lampher, "Fission detectors". Marion & Fowler
"Fast Neutron Physics" Part 1 pp449-506.

66. P.H.White,"Measurements of the ^{235}U neutron fission
cross-section in the energy range 0.04
to 14 Mev". Journal of Nuclear Energy
Parts A/B ,(1965) Vol. 19 pp325-342.

67. W.D.Shults and P.F.Thomason, "Controlled-Potential
Coulometric determination of Copper and
Uranium". Analyt. Chem. $\underline{31}$, 492 (1959).

68. E.B.Sandall, "Coulorimetric determination of
traces of metals". 3rd Edn. Interscience
New York, (1959).

69. G.F.Knoll, "Radiation Detection and Measurement".
John Wiley and Sons(1979).

70. M.Wiernik,"Normal and random pulse generations
for the correction of dead time losses
in Nuclear Spectrometry". Nuc. Instr.
Meth. $\underline{96}$, 325-329 (1971).

71. E.J.Cohen, "Live time and pile-up correction for
    Multichannel Analyser Spectra". Nuc.
    Instr. Meth. 121,25(1974).

72. A.H.Jaffrey,"The actinide elements" NNES PPR IV,
    14A, Ch.16.(McGraw-Hill, New York) 1949.

73. J.A.Crawford, "The transuranium elements". Research
    papers, NNES PPR IV 14B, paper 1655
    (McGraw-Hill, New York).

74. H.Tallquist,Soc. Sci. Fenn. Comm. Phys-Math (1931)
    99, See Reference 77.

75. J.Konijn and B.Tollander, "Efficiency calculation for
    a circular detector viewing a circular
    radiator". Nuc. Instr. Meth. 36,(1965)302-308.

76. A.H.Jaffey, "Solid angle subtended by a circular
    aperture at point and spread sources ". Rev.
    of Scientific Instruments Vol.25, No.4(1954).

77. I.R.Williams,"Monte Carlo calculation of source
    to detector geometry". Nuc. Instr. Meth. 44,
    (1966) 160-162.

78. P.H.White, "A measurement of the half-life of ^{235}U".
    J. of Nuc. Energy Parts A/B, (1965) Vol.19
    pp 33 to 35 .

79. Weast, "Handbook of Chemistry and Physics, 54th
    section", 1973-1974.

80. P.R.Bevington, W.W.Rolland and M.W.Lewis, "Reactive
    yields of neutron groups from the
    ^{7}Li(p,n)Be^{7},Be^{7}* reactions". Phys. Rev. 121,
    871 (1961).

81. J.H.Coon, "Neutron Targets". Marion & Fowler,
    Fast Neutron Physics Part1 ,pg.690.

82. C.M.Bartle and H.O.Meyer, "Improved techniques
    for the preparation of thin deuterated-
    polyethylene targets". Nuc. Instr. Meth.
    $\underline{112}$, (1973) p615.

83. M.I.L.Morgan, "Tritiated targets of scandium ,
    titanium, zirconium, erbium , yttrium
    and uranium". Euratom report EUR2641
    pp 239-263 .

84. D.L.Smith and J.W.Meadows, "Method of Neutron
    activation cross-section measurement
    for E_n=5.5 to 10 Mev using the $D(d,n)^3He$
    reaction as a neutron source". ANL/NDM-9,
    (1973).

85. R.W.Hill,"Angular distributions of elastic scatter-
    ing of 5-Mev neutrons". Phys. Rev. $\underline{109}$,
    2105 (1958).

86. R.Nobles, "High-current gas targets". Rev. Sci.
    Instr. $\underline{23}$, 604 (1952).

87. K.Fiebiger and Z.Naturforsch, 11a , 607(1956).
    See Reference 81.

88. E.Fermi, "nuclear Physics, University of Chicago,
    1950, revised edition p37 (see ref.81).

89. Edwards High Vacuum Catalogue No.7 .

90. Langmuir, Allison Butts Metallurgical problems(1971).

91. J.Grundle, "A study of fission-neutron spectra with high energy activation detectors Part 1. Detector development and excitation measurements". Nuc.Sci. and Eng. $\underline{30}$, 39-53(1967).

92. H.Liskien and A.Paulsen ,"Neutron angular distributions for the D(d, n)^{3}He and T(d, N) T(p, N) reactions". Nuclear Data tables 11(7) p 569-619 (1973).

93. J.L.Fowler & J.E.Brolley, "Monoenergetic neutron techniques in the 10 to 30 Mev range". Rev. of Modern Physics Vol 28 No.2 (1956).

94. P.Fowles, "High current tritium targets". Birmingham Radiation Centre Annual Report BRC-70/03 (1976).

95. Goodfellow Metals Catalogue No.6 1979/1980.

96. R.B.Ross, Metallic materials specification handbook 1972, Halsteel Press, New York .

97. R.L.Heath, "Computer techniques for the analysis of Gamma-ray spectra obtained with NaI and Lithium-ion drifted Germanium detectors". Nuc. Instr. Meth. $\underline{43}$, (1966) 209-229.

98. T.Sekine and H.Babs, "A method of computer analysis of a NaI(Tl) γ-ray spectrum". Nuc. Instr. Meth. $\underline{127}$, 261-263 (1975).

99.   R.L.Heath, R.G.Helmer, L.A.Schmittroth and G.A.Cazier,
       "A method for generating single gamma-
       ray shapes for the analysis of spectra".
       Nuc. Instr. Meth. 47, 281-304(1967).

100.   P.A.Baedecker, "Digital methods of photopeak
       integration in activation analysis".
       Analyt. Chem. Vol.43, No.3 (1971).

101.   S.Terlinski,"Analysis of digital data from a
       multichannel pulse height analyser on
       gamma-ray total absorption peaks in
       activation analysis". Analyt. Chem. Vol.
       40 , No.13, Nov. 1968.

102.   U.Abondanno, A.Boiti and F. Demanins, "The appli-
       cation of a non-iterative method for
       fitting a Gaussian to peaks from Ge(Li)
       and Si detectors". Nuc, Instr. Meth.
       142, 605-607 (1977).

103.   L.Kokta, "Determination of peak area". Nuc. Instr.
       Meth. 112, 245-251 (1973).

104.   T.Sekine and H.Baba, "A measure of the degree of
       fit between the calculated and observed
       spectra". Nuc. Instr. Meth. 133,171-173
       (1976).

105.   T.S.Mudhole and N.Umakonathe, "On the shape of
       the photopeak in a NaI(Tl) scintillation
       detector". Letters to the Editor, Nuc.
       Instr. Meth.(1973) p 401-403.

106.   R.G.Helmer, R.L.Heath, M.Putnam and D.H.Gipson,

         "Photopeak analysis program for photon

         energy and intensity determinations ,

         Ge(Li) and NaI(Tl) spectrometers". Nuc.

         Instr. Meth. 57, 46-57 (1967).

107.   T.Mukoyama, "Fitting of a Gaussian to peaks by

         non-iterative methods". Nuc. Instr. Meth.

         125, 289-291 (1975).

108.   C.C.Grosjean and W.Bossaert, "Table of absolute

         detection efficiencies of cylindrical

         scintillation gamma-ray detectors".

         Computing Lab. Univ. of Ghent. (1965).

109.   W.N.McElroy,"LMFBR reaction rate and dosimetry".

         Quarterly Progress Report Dec. 1971

         78b-4 UNLTD DIST.

110.   D.F.Covell, "Determination of gamma-ray abundance

         directly from the total absorption peak".

         Analyt. Chem. Vol.31, No. 11(1959).

111.   R.L.Heath, AEC Reports, IDO-16408 (1957), IDO-

         1688 (1964).

112.   B.Grosswendt and E.Waibel, "Monte Carlo calculation

         of the intrinsic gamma-ray efficiencies

         of cylindrical NaI(Tl) detectors". Nuc. Instr.

         Meth. 133, 25 (1976).

113.   T.Nakamura,"Monte Carlo calculation of efficiencies

         and response functions of NaI(Tl) crystals

         for thick disc gamma-ray sources and

its application to Ge(Li) detectors ".
Nuc. Instr. Meth. 105, 77-89(1972).

114. T.Nakamura, "Calculation of the detector efficiency
of a 3" diameter x 3" NaI(Tl) crystal
for a thick disc source". Nuc. Instr.
Meth. 86, 163-168(1970).

115. M.Belluscio, R.D.Lev, A.Pantaleo and A.Vox,
"Efficiencies and response function of
NaI(Tl) crystals for gamma-rays from thick
disc sources". Nuc. Instr. Meth. 118,
553-563 (1974).

116. U.C.Mishra and S.Sadasivan,"Experimental peak/total
ratios for a few NaI(Tl) sizes". Nuc. Instr.
Meth. 69, 330-334 (1969).

117. H.Lentz and G.Schultz, "Peak/total ratios for
NaI(Tl) crystals". Nuc. Instr. Meth.
40, 257-260(1960).

118. K.L.Coop and H.A.Grench,"Experimental photopeak
efficiencies for NaI(Tl) crystals". Nuc.
Instr. Meth. 36, 339-340 (1965).

119. B.Chinaglia and R.Malvano,"Efficiency calibration
of 3" x 3" NaI(Tl) crystals". Nuc. Instr.
Meth. 45, 125-132 (1966).

120. E.Storm and H.I.Israel,"Photon cross-sections from
1 Kev to 100 Mev for elements Z=1 to Z=100".
Nuc. Data Tables, A7, 565 (1970).

121. M.E.Rose, "The analysis of angular correlation and angular distribution data". Phys. Rev. $\underline{91}$, 610 (1953).

122. H.I.West, "Angular correlation correction factors via the method of Rose". Lawrence Radiation Lab. Report UCRL-5451 (1959).

123. F.Adams and R.Dams,"Applied Gamma-ray Spectrometry". 2nd Edition and revision of original publication by C.E.Crouthamel , Pergammon Press, Oxford (1970).

124. D.L.Smith and J.W.Meadows, "Measurement of $^{58}Ni(n,p)$ ^{58}Co reaction cross-sections for E_n=0.44 to 5.87 Mev using activation methods". Argonne Nat. Lab. Report ANL-7989.

125 J.W.Meadows,"The ratio of the uranium-238 to uranium-235 fission cross-sections from 1 to 5 Mev". Nuc. Sci. & Eng. $\underline{49}$, 310(1972).

126. B.J.Snyder, "Comparison of calculated and experimental scintillation crystal photofractions". Nuc. Instr. Meth. $\underline{46}$, 173-176(1967).

127. D.I.Garber and R.R.Kinsey, " Neutron Cross-sections" Vol. II , Curves BNL 325 , Jan(1976).

APPENDIX 1

Computer programs for the detection efficiency of a plane disc source viewing a solid-state detector .

APPENDIX 1

(a) Program LOGEOM

This program provides values of the detection efficiency using equations (5.9) and (5.10) where the numerical integration is performed by using Simpson's Rule . The relevant symbols used in the program are as follows :

    A=Source radius

    S=Detector radius

    D=Source-detector radius

The other symbols used correspond to those depicted in the text . The parameters A , T and S , in lines 10 to 30 are set to required values .

(b) Program LGEOM

This Monte Carlo program is described by Williams /77/ and was adapted to run on the Aston University 1904S computer . The NAG library routine "GO5CAF(Y)" is used to generate a random number between zero and one . The data required in the program are as follows :

    RS = Source radius

    RD = Detector radius

    D = Source-detector radius

    COEF = Accuracy required in percent

    NMAX = Maximum number of trials required .

Listing of LOGEOM

This program is written in BASIC .

```
10 A=1.0
20 T=0
30 S=0.691
40 U=0
50 F=0
60 PRINT "DISTANCE"
70 INPUT D
80 B=0


90 C=S
100 GOSUB 500
105 W=(D*U)/(3*A^2)
106 U=0
110 B=S
120 C=A
130 GOSUB 500
140 E=(D*U)/(3*A^2)
145 E=E+W
150 PRINT D,E
160 STOP
170 END
500 N=0
510 O=(C-B)/200
520 FOR R=B TO C STEP O
530 N=N+1
540 X=T*(R-S)/(D-T)
550 IF R)S THEN 604
560 P=2*S
590 M=SQR(D^2+(R+S)^2)
600 L=SQR(D^2+(S-R)^2)
602 GOTO 610
604 P=2*S-X
606 M=SQR(D^2+(R+X-S)^2)
608 L=SQR(D^2+(R+S)^2)
610 G=SQR((L^2+M^2-P^2+2*L*M)/(4*L*M))
620 F=((1-G)*R
630 PRINT F
640 IF N=1 THEN 720
650 IF N=101 THEN 720
660 L=INT(N/2)
670 IF L=N/2 THEN 700
680 U=U+2*F
690 GOTO 730
700 U=U+4*F
710 GOTO 730
720 U=U+F
730 NEXT R
740 RETURN
```

Listing of LGEOM

This program is written in FORTRAN .

```
      MASTER LGEOM
C     MONTE CARLO CALCULATION OF EFFECTIVE SOLID ANGLE
      READ(1,1)RS,RD
      READ(1,2)D,COEF,NMAX
    1 FORMAT(2F6.3)
    2 FORMAT(F6.3,F8.4,I6)
      C=D/SQRT((RS+RD)**2+D**2)
      ETA=0.5*(1.0-C)
      LOW=1
      NMIN=10000
      IHIT=0
    3 DO 10 I=LOW,NMIN
      RN=G05CAF(Y)
      W=C+RN*(1.0-C)
      RHO=SQRT(1.0-W**2)
      RN=G05CAF(Y)
      TT=(2.0*RN-1.0)*3.1415927
      U=RHO*COS(TT)
      V=RHO*SIN(TT)
      RN=G05CAF(Y)
      R=(1.0-RN**2)*RS
      RN=G05CAF(Y)
      PHI=6.283185*RN
      Y=R*SIN(PHI)
      X=R*COS(PHI)
      RL=D/W
      YF=Y+RL*V
      XF=X+RL*U
      Z=SQRT(XF**2+YF**2)
      IF(Z.GT.RD)GO TO 10
    4 IHIT=IHIT+1
   10 CONTINUE
      TOTAL=NMIN
      PI=FLOAT(IHIT)/TOTAL
      F=FLOAT(IHIT)
      SIGMA=(SQRT(F)/F)*100
      IF(SIGMA.LT.COEF)GO TO 5
    5 LOW=NMIN
      NMIN=NMIN+1000
      IF(NMIN.LT.NMAX)GO TO 3
    6 WRITE(2,7)
    7 FORMAT(1H ,28HCANNOT GET COEF SMALL ENOUGH)
    8 P=PI*ETA
      WRITE(2,9)RS,RD,D,P,SIGMA,NMAX
    9 FORMAT(1H ,3E7.3,2E13.5,I6)
      STOP
      END
```

APPENDIX 2

PROGRAM NPROFILE

APPENDIX 2

Description of NPROFILE

A flow chart of the Monte Carlo program NPROFILE is presented in Fig. A.1 .

1. Energy losses in the neutron source.

The energy loss in the gas target window and gas are determined from the equation (Coon /81/):

$$\Delta E_d = \left\{ 0.48(Z/E_d)\left[\ln(E_d/2Z) + a\right] \times 10^{-15} \right\} T \quad (A.1)$$

where ΔE_d represents the energy loss of a deuteron in eV , Z the atomic number of the medium traversed , E_d the deuteron energy in Mev , T the thickness traversed in the medium (nuclei cm^{-2}) and a , an empirical constant , where this constant was selected to fit the experimental data of Coon .

The energy loss in the gas target window (ELW) , at a given incident deuteron energy (ED) , is determined using equation A.1 . The energy loss in the gas (ELG) , is also determined from equation A.1, but with the deuteron energy E_d being replaced by :

$$E_d \equiv EDG = ED - ELW \qquad (A.2)$$

This accounts for the energy loss in the window by the deuteron beam .
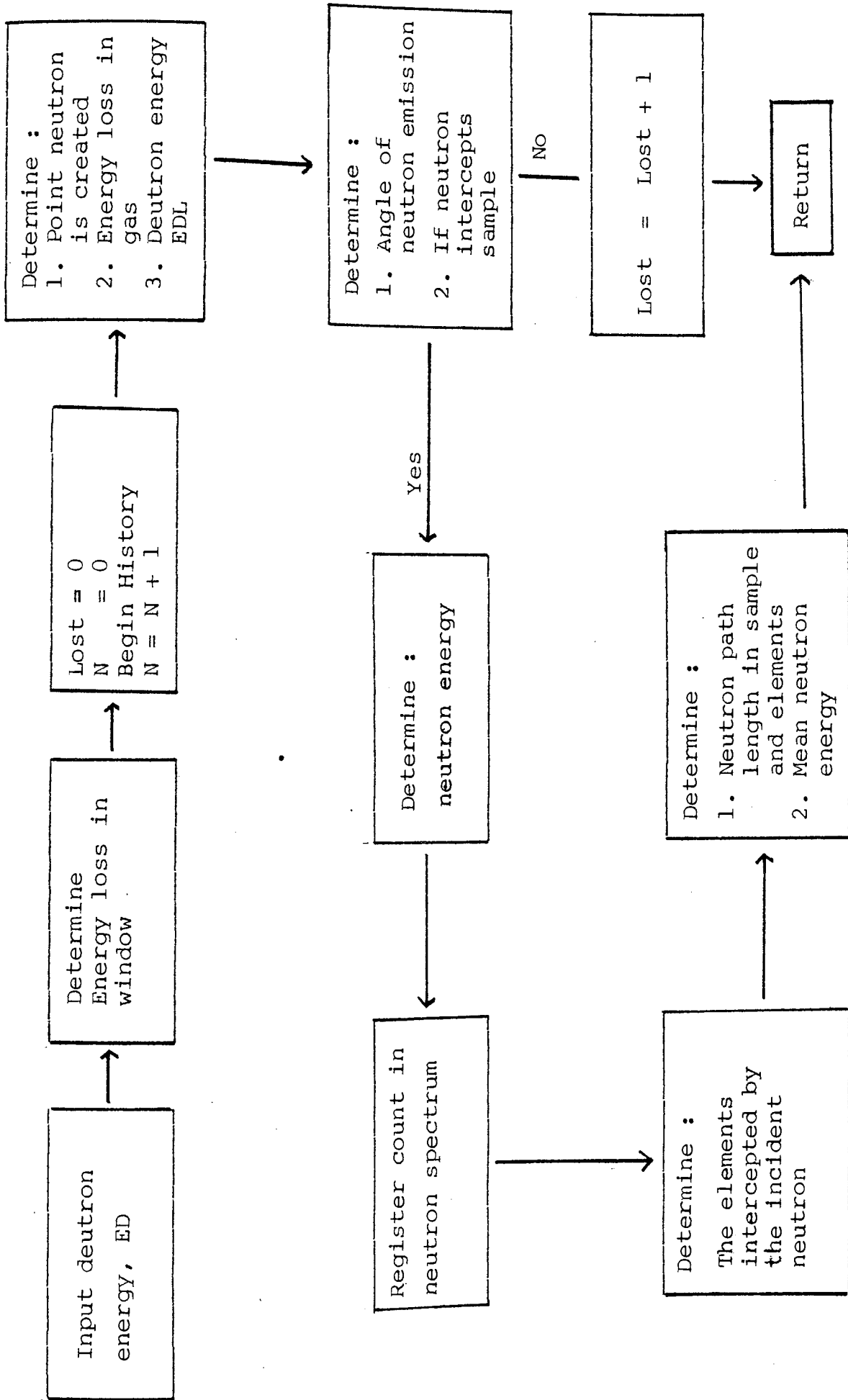
Fig. A.1 Flow diagram for NPROFILE

Whilst the deuteron energy loss in the window is constant with incident deuteron energy, the energy loss in the gas corresponding to the creation of a neutron is dependent upon the distance traversed in the gas prior to neutron creation . Hence , in the program , ELG was represented as the energy loss per centimetre in the gas. The deuteron energy corresponding to the creation of a neutron at a distance PL from the gas target window is given by :

$$EDL = EDG - ELG*PL \qquad\qquad (A.3)$$

PL is in centimetres .

2. Point of neutron creation

In the present calculation the neutron source is defined by a cylinder 3 cm long and 0.3 cm in diameter . Due to the symmetry of the cylinder , a two dimensional representation of the point of creation is sufficient , where the position co-ordinates are represented by (PL,R) . PL and R are determined by multiplying the target length (TL) and the beam radius (RB) , by random numbers .

3. Direction of Neutron Emission

The direction of neutron emission is determined by the co-ordinates θ and ϕ , where θ represents

the neutron angle of emission relative to the direction of the incident deuteron beam and ϕ its inclination relative to the vertical plane . The geometric configuration is depicted in Fig. A.2 .

Angle of emission θ

The angle θ lies in the range $0 \leq \theta \leq \pi$. This interval is divided into N_θ intervals corresponding to angles of emission θ_i where:

$$\theta_i = \pi/N_\theta \ (i - \tfrac{1}{2}) \tag{A.4}$$

and where i=1 to N_θ . Each value of θ_i is weighted by :

$$\sin \theta_i \ \frac{d\sigma}{d\Omega} (E_d , \theta_i) \tag{A.5}$$

where $\sin \theta_i$ accounts for the solid angle and $d\sigma/d\Omega (E_d, \theta_i)$ is the differential cross-section for neutron emission . Hence , the probability for neutron emission at an angle θ_i is given by:

$$P \theta_i = \sin \theta_i \frac{d\sigma}{d\Omega}(E_d, \theta_i)/ \sum_{i=1}^{N_\theta} \sin \frac{\theta_i}{d\Omega} \frac{d\sigma}{}(E_d, \theta_i)$$

$$\tag{A.6}$$

(b)

(a)
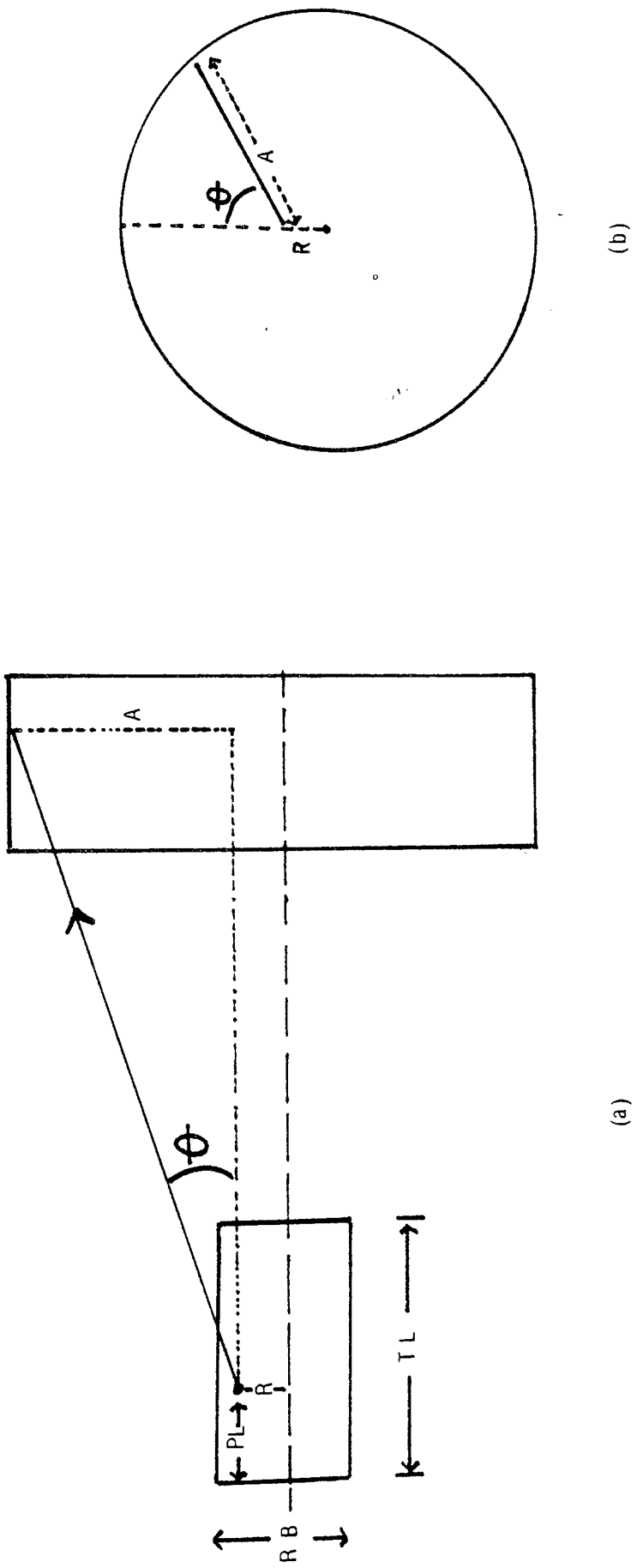
Fig. A.2 A representation of the irradiation geometry

The unit interval (0, 1) in probability space is
divided by a set of N θ_i intervals each of length
y θ_i , where :

$$y_{\theta_i} = \begin{cases} P_{\theta_i} & \text{for } i = 1 \quad (A.7) \\ \\ y_{\theta_{i-1}} + P_{\theta_i} & \text{for } 2 \leq i \leq N_\theta \quad (A.8) \end{cases}$$

If the selected random number , RN, (between zero and
1.0) lies between y $_{\theta_{i-1}}$ and y $_{\theta_i}$, then the value of
the angle of emission θ selected is given by :

$$\theta = (i - RN)(\pi / N_\theta) \qquad (A.9)$$

Angle ϕ

The angle ϕ lies in the range $-\pi < \phi < \pi$.
Due to the symmetry , this range can be reduced to
$(0, \pi)$. Since all values of ϕ are equally probable,
the angle ϕ is related to the random number generated
in the program by the equation :

$$\phi = (1.0 + RN)\pi \qquad (A.10)$$

4. Condition for production of a neutron

Given the position co-ordinates corresponding
to the creation of a neutron (PL,R) and an angle ϕ ,

the maximum possible value of the angle of emission, α , for a neutron to intercept the sample is given by :

$$\alpha = Tan^{-1} (A/(TL - PL + ST)) \qquad (A.11)$$

where ST is the distance between the beam stop , and the surface sample , and A is given by :

$$A = RCos\,\phi + (R^2Cos^2\phi + R_s^2 - R^2)^{\frac{1}{2}} \qquad (A.12)$$

where R_s is the sample radius . If the value selected for θ satisfies the condition $\theta \leq \alpha$, a score is registered and the program proceeds to determine the neutron energy . If this condition is not satisfied, the program registers the trial as a miss and proceeds to the next history .

5. The Neutron Energy profile

The neutron energy , E, is determined using the equation :

$$E = E_d m_G m_n \left\{ 2\,Cos^2\theta + \frac{m_r(m_r + m_n)}{m_G m_n} \left[Q/E_d + (1 - m_G/m_r) \right] \right.$$

$$\left. + 2Cos\,\theta \sqrt{Cos^2\theta + \frac{m_r(m_r + m_n)}{m_G m_n} \left[Q/E_d + (1 - m_G/m_r) \right]} \right\}$$

$$(A.13)$$

where m_G is the mass of the target nucleus (H-2),
m_n the mass of a neutron, m_r the mass of the
residual nucleus (He-3), Q the Q value of the reaction.
E_d is given by EDL . This neutron energy , E, is used
to determine the mean neutron energy using equation
(8.11) .

To determine the neutron energy profile ,
the range of possible neutron energies is divided
into energy intervals and the number of successful
trials for E in each energy interval provides the
energy profile for neutrons incident upon the sample.

6. Irradiation Geometry

Neutron Path lengths in the sample

A schematic representation of the neutron
path lengths in the sample is presented in Fig. A.3 .
If a neutron leaves the disc sample through the flat
surface of a disc , the neutron path length in the
sample is independent of ϕ. Hence , the neutron path
length in the sample , ξ, is given by :

$$\xi = TS/\cos \theta \qquad (A.14)$$

where TS is the thickness of the sample .
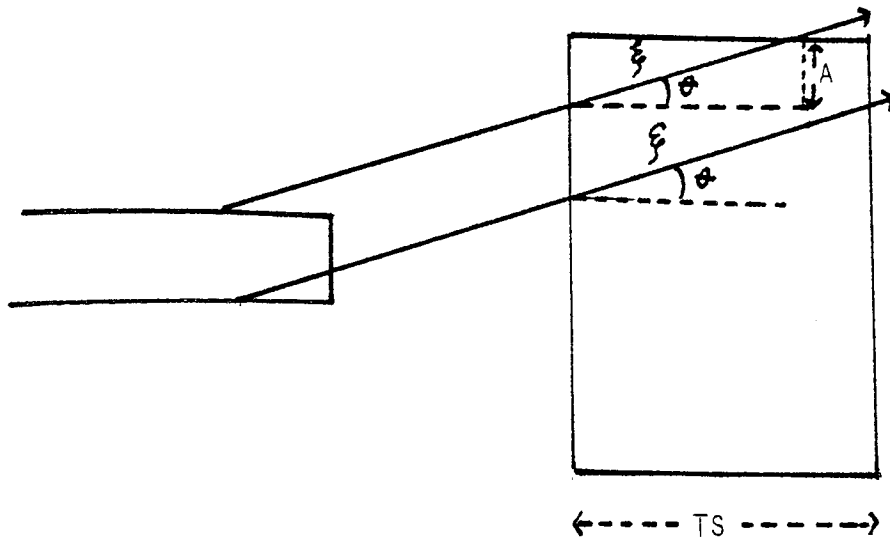
Fig. A.3 : Schematic representation for neutron path
          lengths in the sample .

If the neutron leaves the disc sample through its
curved surface , ξ is given by :

$$\xi = A/Sin \theta \qquad\qquad (A.15)$$

        Equations (A.14) and (A.15) are also appli-
cable to the fissile deposit backing and fissile
deposit , by inserting the value for TB (thickness
of backing) of TF(thickness of fissile deposit)
respectively .

        Finally , the elements intercepted by the
incident neutron are determined from a knowledge of
the point at which the neutron leaves the sample and
fission chamber . Four elements only are considered

in this program since the sample is relatively thin.

7. Listing of relevant symbols used

DIFX - Differential cross-section

BEAMD - Beam Diameter

TL - Neutron Source Length (window to beam stop)

SAMPT - Sample Thickness

SAMPR - Radius of sample .

ST - Neutron Source to sample distance

TB - Thickness of fissile deposit backing

SIGTS - Total macroscopic cross-section for the sample

SIGTB - Total macroscopic cross-section for the fissile
deposit backing material

SIGTF - Total macroscopic cross-section for the fissile
deposit

8. Input Data Requirements

Data Card No.	Data	Format Statement No.
1	TB	16
2	ED	20
3	SIGTS,SIGTB	30
4	SIGTF	35
5-14	DIFX	40

The differential neutron production cross-section data is averaged over 5° intervals .

9. <u>Listing of NPROFILE</u>

The programe is written in FORTRAN

```
    MASTER NPROFILE
    DIMENSION DIFX(36),L(30),ENP(30)
    READ(1,10)BEAMD,TL,SAMPT,SAMPR,ST
10  FORMAT(5F6.3)
    READ(1,16)TB
16  FORMAT(F6.4)
    READ(1,20)ED
20  FORMAT(F6.3)
    READ(1,30)SIGTS,SIGTB
30  FORMAT(2F6.3)
    READ(1.35)SIGTF
35  FORMAT(F11.9)
    READ(1,40)DIFX
40  FORMAT(4F6.2)
    TF=0.0000052
    ELW=(13.44/ED)*(ALOG(ED/56.0)+5.1)*0.02739
    EDF=ED-ELW
    ELG=(0.48/EDG)*(ALOG(EDG/2.0)+4.7)*0.01613
    PO=2.0+5.97286*(3.26893/EDG+0.33214
    RO=2.0*(1.0+5.97286*(3.26893/EDG+0.33214))**0.5
    ENMX=EDG*0.12545*(PO+RO)
    SSTTI=0.0
    DO 50 I=1,36
    F=I
    TTI=(3.1415927/36.0)*(F-0.5)
    STTI=(SIN(TTI))*DIFX(I)
    SSTTI=SSTTI+STTI
50  CONTINUE
    ENMX=IFIX(ENMX 100.0+0.5)
    ENMX=ENMX/100.0
    N1=0
    N2=0
```

```
        N3=0
        N4=0
        NB=0
        NF=0
        LOST=0
        SF1=0.0
        SF2=0.0
        SF3=0.0
        SF4=0.0
        SFF=0.0
        SFB=0.0
        SWEN=0.0
        SETA=0.0
        DO 55 I=1,30
        L(I)=0
   55 CONTINUE
        W1=SAMPT 0.25
        W2=SAMPT 0.5
        W3=SAMPT 0.75
        W4=SAMPT
        WB=SAMPT+TB
        DO 160 N=1,6000
C       DETERMINE POSITION AT WHICH NEUTRON IS PRODUCED
C       ALONG LENGTH OF TARGET
        RN=G05CAF(Y)
        PL=TL*RN
C       DETERMINE POSITION R,ALONG BEAM RADIUS
        RN=G05CAF(Y)
        RB=BEAMD/2.0
        R=RB*RN
C       DETERMINE DIRECTION OF EMMISSION,PHI
C       ALONG BEAM CONE
        RN=G05CAF(Y)
        PHI=(1.0+RN)*3.1415927
```

```
C       DETERMINE MAXIMUM ANGLE,ALFA,AT WHICH
C       NEUTRONS INTERCEPT THE SAMPLE
        A=R*COS(PHI)+(R**2*(COS(PHI))**2+SAMPR**2-R**2)**0.5
        ALFA=ATAN(A/(CTL-PL+ST)
C       DETERMINE ANGLE OF EMMISION TT,WEIGHTED
C       BY THE DIFFERENTIAL CROSS-SECTION AND SOLID ANGLE
        RN=G05CAF(Y)
        YTTI=0.0
        I=0
     60 I=I+1
        F=I
        TTI=(3.1415927/36.0)*(F-0.5)
        IF(TTI.GT.ALFA)GO TO 150
        PTTI=((SIN(TTI))*DIFX(I))/SSTTI
        YTTI=YTTI+PTTI
        IF(RN.GT.YTTI)GO TO 60
        RN=G05CAF(Y)
        TT=(F-RN)*(3.1415927/36.0)
C       COMPUTE NEUTRON ENERGY
        EDL=EDG-ELG*PL
        V1=2.0 (COS(TT))**2+5.97286*(3.26893/EDL+0.33214)
        V2=2.0 COS(TT)*((COS(TT))**2+5.97286 (3.26893/EDL+
       1 0.33124))**0.5
        EN=EDL*0.12545*(V1+V2)
        H=(ENMX-EN)/0.02
        I=IFIX(H+0.5)
        IF(I.LT.1)I=1
        L(I)=L(I)+1
C
C       THIS SECTION OF THE PROGRAM CORRECTS FOR THE IRRADIATION
C       GEOMETRY
C
C       DETERMINE THE NUMBER OF SUCCESFULL TRIALS IN EACH
C       ELEMENT AND THE CORRESPONDING MONTE CARLO AVERAGED
C       ATTENUATION FACTORS
        D=A/TAN(TT)-(ST+TL-PL)
        IF(D.LT.WB)GO TO 70
```

```
      ETA=SAMPT/COS(TT)
      ETAF=TF/COS(TT)
      ETAB=TB/COS(TT)
      WEN=ETA*EN
      SWEN=SWEN+WEN
      SETA=SETA+ETA
      N1=N1+1
      N2=N2+1
      N3=N3+1
      N4=N4+1
      NB=NB+1
      NF=NF+1
      Y=(SIGTS ETA)/4.0
      F1=EXP(-Y)
      F2=F1
      F3=F1
      F4=F1
      FF=EXP(-SIGTF*ETAF)
      FB=EXP(-ETAB*SIGBT)
      SF1=SF1+F1
      SF2=SF2+F2
      SF3=SF3+F3
      SF4=SF4+F4
      SFB=SFB+FB
      SFF=SFF+FF
      GO TO 160
   70 IF(D.LT.W4)GO TO 71
      ETA=SAMPT/COS(TT)
      GO TO 72
   71 ETA=D/COS(TT)
   72 WEN=ETA EN
      SWEN=SWEN+WEN
      SETA=SETA+ETA
      B=W1/COS(TT)
      IF(D.GT.W4)GO TO 75
      IF(D.GT.W3)GO TO 80
```

```fortran
      IF(D.GT.W2)GO TO 90
      IF(D.GT.W1)GO TO 100
      GO TO 110
   75 NB=NB+1
      ETAB=(D-W4)/COS(TT)
      FB=EXP(-SIGTB*ETAB)
      SFB=SFB+FB
      GO TO 115
   80 N4=N4+1
      ETA4=(D-W3)/COS(TT)
      F4=EXP(-SIGTS*ETA4)
      SF4=SF4+F4
      GO TO 120
   90 N3=N3+1
      ETA3=(D-W2)/COS(TT)
      F3=EXP(-SIGTS*ETA3)
      SF3=SF3+F3
      GO TO 130
  100 N2=N2+1
      ETA2=(D-W1)/COS(TT)
      F2=EXP(-SIGTS*ETA2)
      GO TO 140
  110 N1=N1+1
      F1=EXP(-SIGTS*ETA)
      SF1=SF1+1
      GO TO 160
  115 N4=N4+1
      F4=EXP(-SIGTS*B)
      SF4=SF4+F4
  120 N3=N3+1
      F3=EXP(-SIGTS*B)
      SF3=SF3+F3
  130 N2=N2+1
      F2=EXP(-SIGTS*B)
      SF2=SF2+F2
```

```
140 N1=N1+1
    F1=EXP(-SIGTS*B)
    SF1=SF1+F1
    GO TO 160
150 LOST=LOST+1
160 CONTINUE
    XN1=N1
    XN2=N2
    NX3=N3
    XN4=N4
    XNB=NB
    XNF=NF
    AF1=SF1/XN1
    AF2=SF2/XN2
    AF3=SF3/XN3
    AF4=SF4/XN4
    AFB=SFB/XNB
    AVEN=SWEN/SETA
    WRITER(2,170)
170 FORMAT(1H,2X,1HN,4X,4HLOST,5X,2HN1,5X,2HN2,5X,2HN3,
   15X,2HN4,5X,2HN,B,5X,2HNF)
    WRITE(2,180)N,LOST,N1,N2,N3,N4,NB,NF
180 FORMAT(1H,15,717//)
    WRITE(2,190)AVEN
190 FORMAT(1H,13HMEAN ENERGY= ,F5.3,1X,3HMEV/)
    WRITE(2,200)
200 FORMAT(1H,5H AF1,5X,3HAF2,5X,3HAF3,5X,3HAF4,5X,3HAFF,
   15X,3HAFB)
    WRITE(2,210)AF1,AF2,AF3,AF4,AFF,AFB
210 FORMAT(6f'.4///)
    WRITE(2,200)
220 FORMAT(1H,15HNEUTRON PROFILE//)
    DO 250 I=1,30
    F=I
    ENP(I)=(ENMX+0.010)-(F 0.02)
    WRITE (2,230)ENP(I),L(I)
```

```
230 FORMAT(iH,F7.3,16)
250 CONTINUE
    STOP
    END
```

PROGRAM 3

PROGRAM PEAKFIT

APPENDIX 3

Listing of PEAKFIT

The program PEAKFIT is written in BASIC .

```
2 INPUT L,M
10 REMARK PROGRAM PEAK FIT
40 PRINT "HOW MANY DATA POINTS "
50 INPUT N
60 DIM X(N),Y(N),H(N),W(N),O(N)
70 A=0
80 B=0
90 C=0
95 R=0
100 D=0
110 FOR I=1 TO N STEP 1
120 PRINT "CHANNEL NO. ?"
130 INPUT X(I)
140 PRINT "COUNTS ?"
150 INPUT Y(I)
160 NEXT I
162 OPEN 1,4
163 CMD1


170 FOR I=2 TO N-1 STEP 1
180 L=I-1
190 M=I+1
200 K=N-2
210 H(I)=LOG(Y(L)/Y(M))
220 O(I)=(1/Y(L)+1/Y(M))
230 O(I)=1/O(I)
240 A=A+X(I)*O(I)
250 B=B+H(I)*O(I)
260 C=C+X(I)*H(I)*O(I)
270 D=D+X(I)*X(I)*O(I)
280 R=R+O(I)
290 NEXT I
300 E=(R*C-A*B)/(R*D-A*A)
310 F=(B*D-A*C)/(R*D-A*A)
315 PRINT E
320 S=SQR(2.0/E)
330 P=-F/E
340 PRINT "PEAK POSITION = ";P
350 PRINT "SIGMA = ";S
360 REMARK RESIDUALS
```

```
370 T=0
371 A=0
372 D=0
380 FOR I=2 TO N-1 STEP 1
390 Z=2*(X(I)-P)/S^2
392 A=A+X(I)
393 D=D+X(I)*X(I)
400 R=(H(I)-Z)^2
410 T=T+R
420 NEXT I
430 R=T/(K-2)
440 GOSUB 600
450 PRINT "PEAK HIGHT = ";U
460 A=2.507*S*U
470 PRINT "PEAK AREA = ";A
471 PRINT " CHANNEL LIMITS (XL,XL) ?"
472 INPUT L,M
480 FOR X=L TO M STEP 1
490 Z=((X-P)^2)/(2*S^2)
500 Z=-Z
510 A=U*EXP(Z)
520 PRINT X,A
525 NEXT X
530 STOP
540 END
600 REMARK SUBROUTINE PEAK HIGHT
610 V=K*D-A^2
620 REMARK T IS ERROR IN SIGMA
630 G=SQR(K*R/V)
640 T=(0.7071*G)/(E^1.5)
650 REMARK Q IS ERROR IN P
660 U=SQR(R/(V*D))
670 Q=SQR((U/E)^2+(P*G/E^2)^2)
680 REMARK DETERMINE WEIGHTING
685 Z=0
686 B=0
690 FOR I=1 TO N STEP 1
700 V=Q^2+((X(I)-P)^2)*(T^2)/(S^2)
710 W(I)=1/Y(I)+(((X(I)-P)^2)*V)/S^4
720 W(I) =1/W(I)
730 A=W(I)*(LOG(Y(I))+((X(I)-P)^2)/(2*S^2))
740 B=B+A




750 Z=Z+W(I)
760 NEXT I
770 C=B/Z
780 REMARK PEAK HIGHT U
790 U=EXP(C)
800 RETURN
READY.
```

APPENDIX 4

Program GAMMA

APPENDIX 4

Description of GAMMA

The position of nuclei in the sample are
defined by the position co-ordinates (R,T) in the
disc sample (see Fig. A.4).
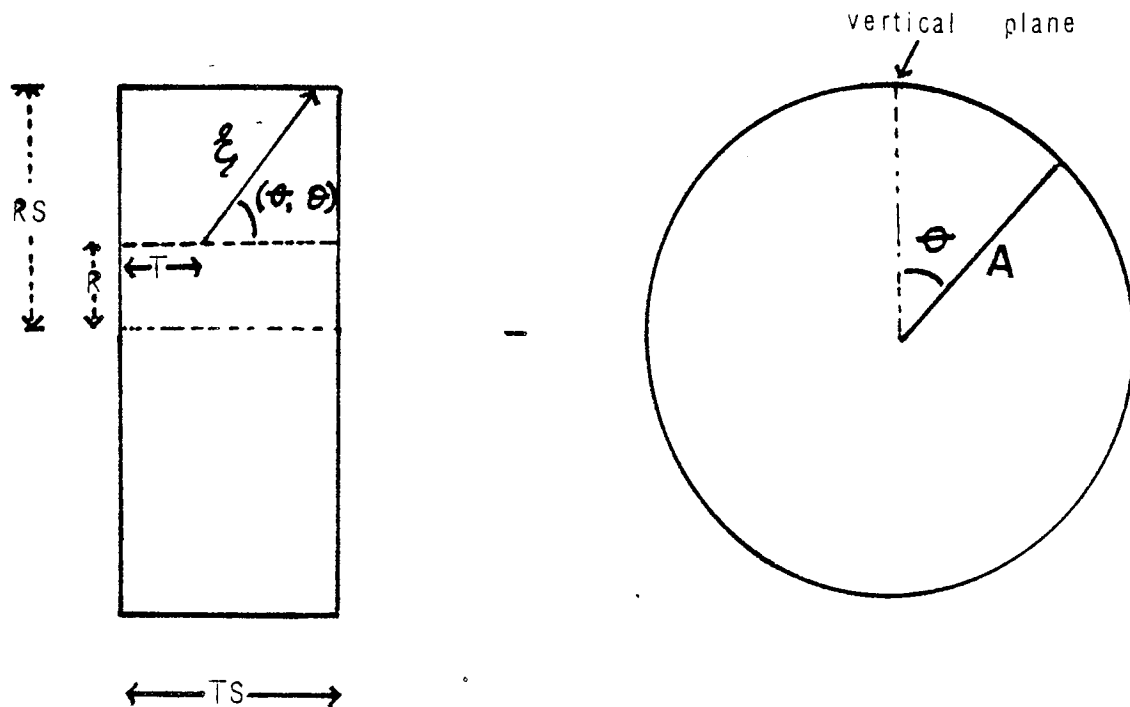
Fig . A.4 : Disc geometry applicable to the determination
of gamma-ray path lengths in the sample .

1. Co-ordinate T

The co-ordinate T in the sample is selected
at random such that :

$$T = TS \times RN \qquad (A.16)$$

where TS is the sample thickness in centimetres .

Co-ordinate R

The sample radius is divided into N_R equally spaced intervals, such that :

$$R_i = RS/N_R \; (i - \tfrac{1}{2}) \tag{A.17}$$

Each value of R_i corresponds to an area $2\pi R_i (R/N_R)$. Hence, the probability P_{R_i} increases with R_i, where:

$$P_{R_i} = \frac{r_i}{\sum\limits_{i=1}^{N_R} R_i} \tag{A.18}$$

Thus the unit interval $(0,1)$ in probability space can be divided by N_R intervals corresponding to y_{R_i}, such that :

$$y_{R_i} = \begin{cases} P_{R_1}, & \text{for } i=1 \\ \\ Y_{R_{i-1}} + P_{R_i}, & \text{for } 2 \leq i \leq N_R \end{cases} \tag{A.19}$$

If the selected random number RN satisfies the inequality $Y_{R_{i-1}} < RN \leq Y_{R_i}$, then :

$$R = (i - RN) \, RS/N_R \tag{A.20}$$

3. Directions for Gamma-ray emission

All nuclei are assumed to emit gamma-rays isotropically . The direction of emission is defined by the angular co-ordinates θ and ϕ, where θ is the angle between the direction of the emitted gamma-ray and the direction perpendicular to the flat surface of the disc . The angle ϕ is the inclination of this plane relative to the vertical plane . The angles θ and ϕ are determined using the methods described in Section 3 of Appendix 2 , but with the differential cross-section term in equation A.6 set to 1 since the emission is isotropic .

4. Gamma-ray path lengths in the sample

The gamma-ray path lengths in the sample can be defined from the geometry shown in Fig. A.5.
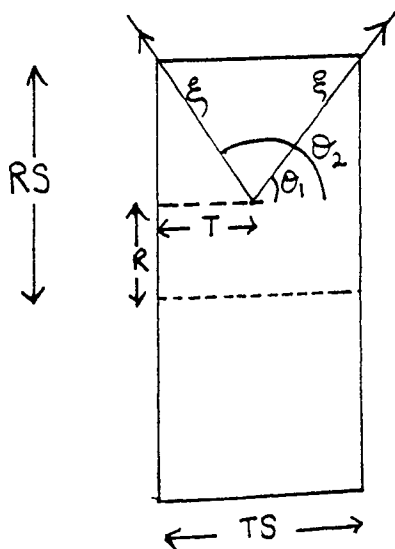
Fig. A.5 : Possible gamma-ray path lengths in the sample .

As shown by Fig. A.5, the γ-ray path length in the sample can be represented as :

$$
\xi = \begin{cases}
(TS-T)/\cos\theta, & \text{for } \theta \leq \theta_1 \\
A/\sin\theta, & \text{for } \theta_1 < \theta \leq \theta_2 \\
-T/\cos(\theta), & \text{for } \theta > \theta_2
\end{cases}
$$

where A is defined by equation (A.12) .

5. Listing of relevant symbols used in the program

G1, G2, G3, etc. are the linear absorption cross-sections for gamma-rays 1 , 2,3 etc.

6. Input Data

The program requires as input the linear absorption cross-sections G1 , G2 , G3 , etc. The radius of the disc sample , R_s , and its thickness , TS, are set to the required values in the program .

8. Listing of GAMMA

The program is written in FORTRAN

```
      MASTER GAMMA
C     CALCULATION OF GAMMA-RAY MULTIPLE SCATTERING CORRECTION
C     BY THE MONTE CARLO METHOD
   10 FORMAT (F10-6,F10-6,F10-6,F10-6,F10-6,F10-6)
   15 FORMAT (1X,F10-6,F10-6,F10-6,F10-6,F10-6,F10-6)
      READ(1,10)G1,G2,G3,G4,G5,G6
      RS=1.0
      TS=0.2
      SUMB1=0.0
      SUMB2=0.0
      SUMB3=0.0
      SUMB4=0.0
      SUMB5=0.0
      SUMB6=0.0
      SUMRI=0.0
      DO 20 I=1,20
      F=1
      RI=(RS/20.0) * (F-0.5)
      SUMRI=SUMRI+RI
   20 CONTINUE
      SUMTTI=0.0
      DO 60 I=1,20
      F=I
      TT1=(3.1415927/20.0) * (F-0,5)
      SUMTTI=SUMTTI+SIN(TTI)
   60 CONTINUE
      DO =130 N+1,3000
      RN=G05CAF(Y)
      I=0
      YRI=0.0
   40 I=I+1
      F=I
      RI=(RS/20.0) *(F-0.5)
```

```
          PRI=RI/SUMRI
          YRI=YRI+PRI
          IF(RN.GT.YRI)GO TO 40
          R=(F.I) * (RS/20.0)
C         DETERMINE POSITION COORDINATE T
          RN=G05 CAF(Y)
          T=TS * RN
C         DETERMINE SCATTERING ANGLE TT
          RN=G05 CAF(Y)
          YTTI=0.0
          I=0
   70     I=I+1
          F=I
          TTI=(3.1415927/20.0) * (F-0.5)
          PTTI=SIN(TTI)/SUMTTI
          YTTI=YTTI+PTTI
          IF(RN.GT.YTTI)GO TO 70
          TT=(F-RN) * (3.1415927/36.0)
C         DETERMINE SCATTERING ANGLE PHI
          RN=G05 CAF(Y)
          PHI=(1.0+RN) * 3.1415927
          IF (PHI.GT.3.1415927)PHI=3.1415927
          A=R * COS (PHI) + ((R**2.0) * (COS (PHI))**2.0+RS**2.0-
         1R   2.0)**0.5
          IF (TT.LT.ATAN(A/(TS-T)))GO TO 100
          IF (TT.LT.(3.1415927-ATAN(A/T)))GO TO 110
          GO TO 120
  100     PLENTH+(TS-T)/COS(TT)
          GO TO 125
  110     PLENTH=A/SIN(TT)
          GO TO 125
  120     PLENTH=-T/COS(TT)
  125     B1=EXP(-G1 PLENTH)
          B2=EXP(-G2 PLENTH)
          B3=EXP(-G3 PLENTH)
```

```fortran
      B4=EXP(-G4*PLENTH)
      B5=EXP(-G5*PLENTH)
      B6=EXP(-G6*PLENTH)
      SUMB1=SUMB1+B1
      SUMB2=SUMB2+B2
      SUMB3=SUMB3+B3
      SUMB4=SUMB4+B4
      SUMB5=SUMB5+B5
      SUMB6=SUMB6+B6
  130 CONTINUE
      N=F
      SC461=SUMB1/F
      SC462=SUMB2/F
      SC47=SUMB3/F
      SC481=SUMB4/F
      SC482=SUMB5/F
      SC483=SUMB6/F
      WRITE(2,15) SC461,SC462,SC47,SC481,SC482,SC483
      STOP
      END
```

APPENDIX 5

Program NSCAT

APPENDIX 5

The Monte Carlo methods applied in NSCAT are similar to those described in Appendix 4 and are also described by Smith et al /124/.

1. Symbols used in NSCAT

STS - Total macroscopic cross-section for sample

STB - " " " " fissile deposit backing

SES - Macroscopic elastic scattering cross-section for sample

SEB - Macroscopic elastic scattering cross-section for fissile deposit backing

STF - Total macroscopic cross-section for fissile deposit

SF - Macroscopic fission cross-section for ^{235}U deposit.

Other symbols are as depicted in Appendices 2 and 4 .

2. Input Data Required

Data Card Number	Data	Format Statement No.
1	STS,STB,SFS,SEB	20 21
2	STF	22
3	SF	

Listing of NSCAT

The program is written in FORTRAN .

```fortran
      PROGRAM NSCAT
C        NEUTRON SCATTERING CORRECTIONS
      READ(1,20)SFS,STF,SES,SEF
   20 FORMAT(4F5.5)
      READ(1,21)STF
   21 FORMAT(F5.6)
      READ(1,22)SF
   22 FORMAT(F5.6)
      RS=1.0
      TS=0.2
      TF=0.0125
      TF=0.000052
      TSF=TS+TF
      TSSF=TSS+TF
      SUMRI=0.0
      DO 30 I=1,20
      F=I
      RI=(RS/20.0)*(F-0.5)
      SUMRI=SUMRI+RI
   30 CONTINUE
      SUMTI=0.0
      DO 40 I=1,10
      F=I
      TI=(TS/20.0)*(F-0.5)
      ETI=EXP(-STS*TI)
      SUMTI=SUMTI+ETI
   40 CONTINUE
      DO 50 I=1,20
      F=I
      TTI=SIN((3.1415927/20.0)*(F-0.5))
      SUMTTI=SUMTTI+TTI
   50 CONTINUE
      Y=0
      N=0
      U=0.0
      SALFA=0.0
      SBETA=0.0
      SRHO=0.0
      SGSTR=0.
      DO 170 N=1,1000
C        CORRECTION SFS
      RN=0.5*CDF(Y)
      YRI=0.0
      I=0
   60 I=I+1
      F=I
      RI=(RS/20.0)*(F-0.5)
      YRI=YRI+RI/SUMRI
      IF(RN.GT.YRI)GO TO 60
      Y=RI
      RN=0.5*CDF(Y)
      YTI=0.0
```

```
70  I=I+1
    F=I
    TI=(TS/20.0)*(F-0.5)
    ETI=EXP(-STS*TI)
    YTI=YTI+ETI/SUMTI
    IF(RN.GT.YTI)GO TO 70
    T=TI
    RN=GOSCAF(Y)
    YTTI=0.0
    I=0
80  I=I+1
    F=I
    TTI=(3.1415927/20.0)*(F-0.5)
    YTTI=YTTI+SIN(TTI)/SUMTTI
    IF(RN.GT.YTTI)GO TO 80
    TT=TTI
    RN=GOSCAF(Y)
    PHI=(1.0+RN)*3.1415927
    R=R*COS(PHI)+((R**2)*(COS(PHI))**2+RS**2-R**2)**0.5
    IF(TT.LT.ATAN(A/(TS-T)))GO TO 90
    IF(TT.LT.(3.1415927-ATAN(A/T)))GO TO 100
    PLS=-T/COS(TT)
    GO TO 110
90  PLS=(TS-T)/COS(TT)
    GO TO 110
100 PLS=A/SIN(TT)
110 ALFA=EXP(-STS*PLS)
115 FORMAT(2F8.5)
160 SALFA=SALFA+ALFA
C        CORRECTION GAMA
    IF(TT.GT.ATAN((RS-R)/(TSBF-T)))GO TO 120
    J=J+1
    PLSBF=(TSBF-T)/COS(TT)
    PLF=(PLS-F*TS)/(TSBF-T)
    PLF=(PLS-F*TF)/(TSBF-T)
    GAMA=(EXP(-(STS*PLS+STB*PLB)))*(1.0-EXP(-STF*PLF))
    SGAMA=SGAMA+GAMA
C        CORRECTION BETA
120 IF(TT.LT.(3.1415927-ATAN(2.0*(RS-R)/TB)))GO TO 150
    K=K+1
    IF(TT.LT.(3.1415927-ATAN(A/(TS+TB/2.0))))GO TO 130
    PLBS=-(TS+TB/2.0)/COS(TT)
    GO TO 140
130 PLBS=A/SIN(TT)
140 PLB=(PLBS*COS(TT)-TB/2.0)/COS(TT)
    PLS=(TB/2.0)/COS(TT)
    BETA=(EXP(-STB*PLB))*(1.0-EXP(-STS*PLS))
    SBETA=SBETA+BETA
```

```
150   IF(TT.GT.ATAN(2.*(RHS-R)/TB))GO TO 170
C     CORRECTION RHO
      L=L+1
      PLBF=(TF+TB/2.0)/COS(TT)
      PLB=(PLBF*TB/2.0)/(TB/2.0+TF)
      RHO=(EXP(-STB*PLB))*(1.0-EXP(-STF*PLF))
      RHO=RHO+RHO
170   CONTINUE
      XN=N-1
      ASALFA=SALFA/XN
      ASBETA=SBETA/XN
      ASGAMA=SGAMA/XN
      ASRHO=SRHO/XN
      ALFA=(SES/STS)*(1.0-ASALFA)
      BETA=(SFL/STB)*(EXP(-STS*TS))*(1.0-EXP(-STB*TB))/(1.0-EXP(-STS*TS))
     1)
      ETA=ETA+ETA*ASBETA
      GAMA=(SES/STS)*(EXP(STS*TS+STB*TB))*(1.0-EXP(-STS*TS))
      GAMA=GAMA+ASGAMA/(1.0-EXP(-STF*TF))
      RHO=(SEB/STB)*(EXP(STB*TB))*(1.0-EXP(-STB*TB))/(1.0-EXP(-STF*TF))
      RHO=RHO+ASRHO
      WRITE(2,180)N,K,J,L
180   FORMAT(1H ,2HN=,I5,2X,2HK=,I5,2X,2HJ=,I5,2X,2HL=,I5)
      WRITE(2,190)ALFA,BETA,GAMA,RHO
190   FORMAT(1H ,5HALFA=,F3.6,2X,5HBETA=,F3.6,2X,5HGAMA=,F3.6,2X,4HRHO=,
     1F8.6)
      WRITE(2,200)SPLS
200   FORMAT(1H ,F8.3)
      STOP
      END
```